Graphical Abstract

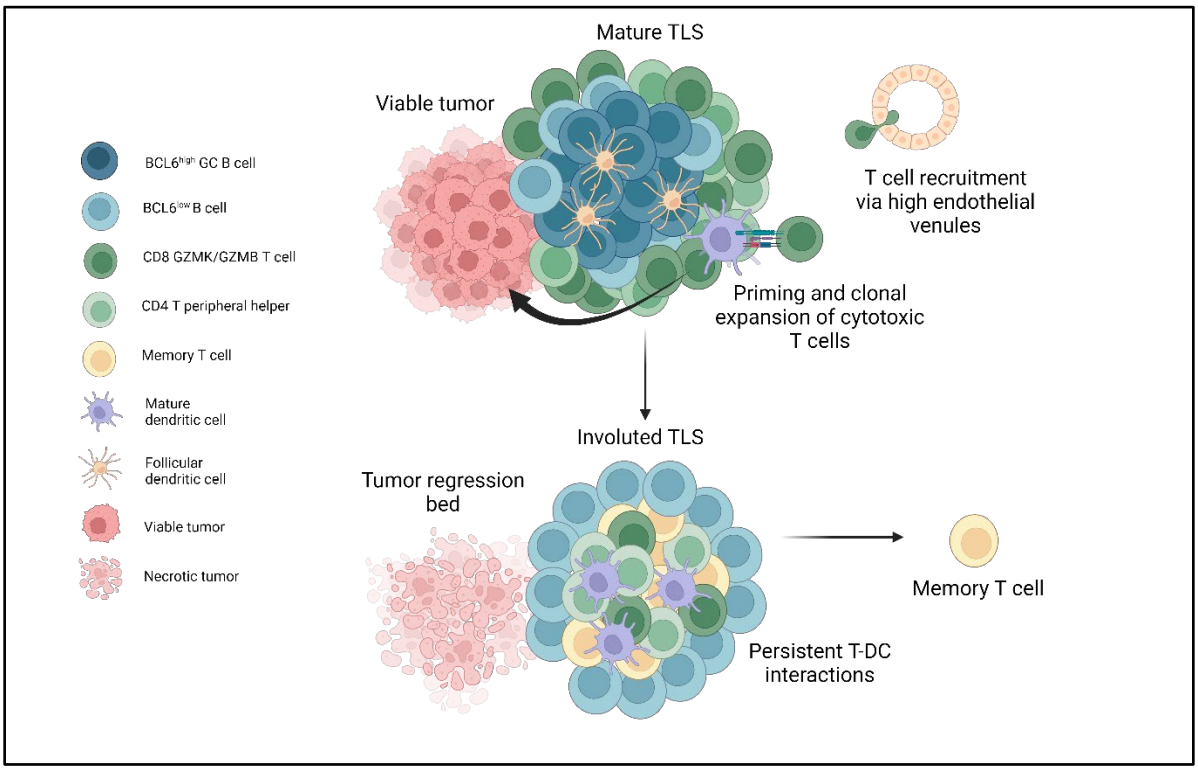

Highlights

1. In patients with hepatocellular carcinoma (HCC), tertiary lymphoid structures (TLS) are induced by neoadjuvant immunotherapy and are associated with favorable clinical outcomes.

2. TLS within the same tumor demonstrate extensive sharing of expanded granzyme K and granzyme B-expressing $CD8^+$ T effector memory clonotypes, but the B cell repertoires of individual TLS are almost wholly distinct, consistent with independent germinal center reactions.

3. Within areas of viable tumor, mature TLS are characterized by high expression of CD21 and CD23, $BCL6^+$ germinal center B cells, and close interactions between $DCLAMP^+$ mature dendritic cells and $CXCR5^-CXCR3^+$ CD4 T peripheral helper cells within a T cell zone adjacent to the B cell follicle.

4. Within areas of tumor regression, an involuted TLS morphology is identified that is notable for dissolution of the B cell germinal center, retention of the T cell zone, and increased T cell memory.

Immune landscape of tertiary lymphoid structures in hepatocellular carcinoma (HCC) treated with neoadjuvant immune checkpoint blockade

Daniel H. Shu[1,2], Won Jin Ho[1,2], Luciane T. Kagohara[1,2], Alexander Girgis[1,2,3], Sarah M. Shin[1], Ludmila Danilova[1], Jae W. Lee[4], Dimitrios N. Sidiropoulos[1,2], Sarah Mitchell,[1] Kabeer Munjal[1], Kathryn Howe[1], Kayla J. Bendinelli[1], Hanfei Qi[1], Guanglan Mo[1], Janelle Montagne[1,2], James M. Leatherman[1], Tamara Y. Lopez-Vidal[1,2], Qingfeng Zhu[2,4], Amanda L. Huff[1,2], Xuan Yuan[3], Alexei Hernandez[1], Erin M. Coyne[1], Neeha Zaidi[1,2], Daniel J. Zabransky[1,2], Logan L. Engle[5,6,7], Aleksandra Ogurtsova[5,6,7], Marina Baretti[1], Daniel Laheru[1,2], Jennifer N. Durham[1], Hao Wang[1], Robert Anders[2,4], Elizabeth M. Jaffee[1,2,7], Elana J. Fertig[1,2,3,8*], Mark Yarchoan[1,2,7*]

[1] Department of Oncology, Sidney Kimmel Comprehensive Cancer Center, Johns Hopkins University School of Medicine, Baltimore, Maryland.
[2] Convergence Institute, Johns Hopkins University, Baltimore, Maryland.
[3] Department of Biomedical Engineering, Johns Hopkins University School of Medicine, Baltimore, Maryland.
[4] Department of Pathology, Johns Hopkins University School of Medicine, Baltimore, Maryland, USA.
[5] Department of Dermatology, Johns Hopkins University School of Medicine, Baltimore, Maryland.
[6] The Mark Foundation Center for Advanced Genomics and Imaging, Johns Hopkins University, Baltimore, Maryland.
[7] Bloomberg~Kimmel Institute for Cancer Immunotherapy and Sidney Kimmel Comprehensive Cancer Center, Johns Hopkins University, Baltimore, Maryland.
[8] Department of Applied Mathematics and Statistics, Johns Hopkins University Whiting School of Engineering, Baltimore, Maryland.

* Corresponding authors:
Mark Yarchoan (mark.yarchoan@jhmi.edu)
Elana J. Fertig (ejfertig@jhmi.edu)

Keywords: neoadjuvant immunotherapy, tertiary lymphoid structures, hepatocellular carcinoma, immune checkpoint inhibitors, single cell multiomics, imaging mass cytometry, single cell RNA, single cell TCR,

ABSTRACT

Neoadjuvant immunotherapy is thought to produce long-term remissions through induction of antitumor immune responses before removal of the primary tumor. Tertiary lymphoid structures (TLS), germinal center-like structures that can arise within tumors, may contribute to the establishment of immunological memory in this setting, but understanding of their role remains limited. Here, we investigated the contribution of TLS to antitumor immunity in hepatocellular carcinoma (HCC) treated with neoadjuvant immunotherapy. We found that neoadjuvant immunotherapy induced the formation of TLS, which were associated with superior pathologic response, improved relapse free survival, and expansion of the intratumoral T and B cell repertoire. While TLS in viable tumor displayed a highly active mature morphology, in areas of tumor regression we identified an involuted TLS morphology, which was characterized by dispersion of the B cell follicle and persistence of a T cell zone enriched for ongoing antigen presentation and T cell-mature dendritic cell interactions. Involuted TLS showed increased expression of T cell memory markers and expansion of $CD8^+$ cytotoxic and tissue resident memory clonotypes. Collectively, these data reveal the circumstances of TLS dissolution and suggest a functional role for late-stage TLS as sites of T cell memory formation after elimination of viable tumor.

INTRODUCTION

Immune checkpoint blockade (ICB) therapy has revolutionized the treatment of metastatic solid tumors, offering to a subset of patients the potential for sustained remissions beyond what was previously possible with chemotherapy alone.[1,2] For patients with early stage, non-metastatic disease, the role for ICB and ideal timing of its administration remains an area of intense clinical investigation. Recent clinical data in patients with melanoma suggest that neoadjuvant immunotherapy, in which ICB is administered prior to curative-intent resection of the primary tumor, may produce superior long-term outcomes compared to immunotherapy given after surgery.[3,4] Preclinical data suggest that these improved outcomes may be attributable to an elevated and sustained tumor-specific immune response that occurs when immunotherapy is initiated with the primary tumor *in situ*.[5,6] However, in human subjects it is not known where or by what means the establishment of immunological memory occurs.

Tertiary lymphoid structures (TLS), organized collections of B and T cells that can arise within solid tumors, have been associated with favorable responses to neoadjuvant ICB,[7–13] and it is hypothesized that TLS play a mechanistic role in promoting effective antitumor immunity. However, understanding of the structure, constituent immune populations, and life cycle of TLS in this treatment setting remains limited by the rarity of neoadjuvant clinical trial specimens, particularly in solid tumor types where the successes of immunotherapy have been modest, and paucity of animal models for TLS in cancer.[14,15] Thus patient samples from neoadjuvant clinical trials provide a unique opportunity to investigate the contribution of TLS to the development of antitumor immunity.

We previously reported an association between TLS and pathologic response in a phase 1 trial of patients with locally advanced HCC who received neoadjuvant nivolumab and cabozantinib.[8] Here, we evaluated the clinical and immunological characteristics of TLS in an expanded cohort of patients with locally advanced hepatocellular carcinoma (HCC) treated with neoadjuvant ICB. We find evidence that neoadjuvant ICB induces the formation of intratumoral TLS, and that high TLS density following neoadjuvant therapy is associated with superior pathologic response to treatment and relapse-free survival. Using a multiomics approach employing imaging mass cytometry, bulk TCR and BCR sequencing of microdissected TLS, and paired single cell RNA

and TCR sequencing, we identify key differences in the spatial and immunological landscape of TLS in areas of viable and nonviable tumor that suggest that the contribution of TLS to antitumor immunity in tumors treated with neoadjuvant immunotherapy varies significantly according to morphological stage and circumstance.

RESULTS

Neoadjuvant ICB in HCC induces intratumoral TLS

To determine the clinical significance of TLS in patients with HCC treated with neoadjuvant ICB, we identified patients from the Johns Hopkins Liver Cancer Biorepository who had undergone surgical resection of their primary tumor after receiving neoadjuvant ICB-based therapy for locally advanced HCC. In total, 19 patients were identified who received treatment between October 2019 and January 2022 (**Extended Data Table 1**). 11/19 (57.9%) were male, 13/19 (68.4%) had tumors with moderately differentiated histology, and 11/19 (57.9%) had a history of viral hepatitis. No patients had active viral hepatitis at the time of surgery. 14/19 (73.6%) received anti-PD-1 plus an oral tyrosine kinase inhibitor, 3/19 (15.8%) received anti-PD-1 monotherapy, 1/19 (5.2%) received combination anti-PD-1 and anti-CTLA-4 monoclonal antibody, and 1/19 (5.2%) received combination anti-PD-1/anti-CTLA-4 and oral TKI prior to resection of the primary tumor.

Since TLS are known to occur in treatment naïve HCC,[16] we first attempted to determine if TLS were present in the tumors of patients prior to receiving neoadjuvant ICB. 7/19 (36.8%) of patients had undergone pre-treatment fine needle biopsies prior to initiation of neoadjuvant therapy and no intratumoral TLS were identified in these specimens. Given the limited assessment of the tumor microenvironment provided by fine needle biopsy, we next identified a second cohort of HCC patients treated at our institution who had undergone surgical resection without receiving prior systemic therapy, which would serve as a control cohort. 17 patients were identified who had received upfront surgical resection for HCC between 2017 and 2022, from which 3 patients were excluded due to small tumor volume, poor tissue quality, or HCC etiology not represented by the treatment cohort. The 14 remaining patients (**Extended Data Table 2**), were similar to the neoadjuvant treatment cohort by age, sex, histologic grade, and etiology (**Table 1**).

Evaluation of TLS density in the two cohorts was performed by CD20 staining of resected FFPE tumor (**Fig. 1a**). TLS, which we defined as $CD20^+$ lymphoid aggregates with diameter greater than 150 µm, were classified as either peritumoral or intratumoral according to their location relative to the interface between tumor and normal adjacent parenchyma (**Fig. 1b**). TLS were observed in 7/14 (50%) of untreated tumors and 12/19 (63.2%) treated tumors. No significant difference was identified in total TLS density (0.08±0.09 TLS/mm^2 versus 0.05±0.10 TLS/mm^2, P = 0.42) or peritumoral TLS density (0.03±0.05 TLS/mm^2 versus 0.04±0.1 TLS/mm^2, P = 0.73) (**Extended Fig. 1a**), but intratumoral TLS density was significantly increased in treated patients compared to untreated controls (0.05±0.08 TLS/mm^2 versus 0.01±0.02 TLS/mm^2, P = 0.05) (**Fig. 1c**). In untreated tumors, the majority of TLS were peritumoral, whereas in neoadjuvant treated tumors the majority were intratumoral (**Extended Data Fig 1b-c**). Taken together, these data suggest that neoadjuvant ICB induces the formation of intratumoral TLS.

High intratumoral TLS density after neoadjuvant ICB is associated with superior pathologic response and disease-free survival

We next set out to determine if there were an association between high TLS density after neoadjuvant ICB and three clinically meaningful endpoints: pathologic response to treatment, relapse free survival, and overall survival. Tumors treated with neoadjuvant ICB were reviewed

and assigned to a pathologic response category (non-response [NR], partial pathologic response [pPR], or major or complete pathologic response [MPR/CR]) according to percent residual viable tumor at the time of surgery.[17] 8/19 (42.1%) patients had a major or complete pathologic response, of which 2 had CR and 6 had MPR; 8/19 (42.1%) had a partial pathologic response (pPR); and 3/19 (15.8%) had non-response (NR). Intratumoral TLS density was significantly increased in tumors with MPR/CR compared to tumors with pPR (P = 0.000246), NR (P = 0.0129), or untreated patients (P = 0.000142) by Tukey's HSD test. In addition, total TLS density was also increased in tumors with MPR/CR compared to tumors with pPR (P = 0.00144), NR (P = 0.02), and untreated tumors (P = 0.00694) (**Fig. 1d** and **Extended Data Fig. 1d**). No significant difference was observed in peritumoral TLS density across pathologic response groups or untreated tumors (**Extended Data Fig. 1e**). Additional pathologic assessment was also performed according to the Immune Related Pathologic Response Criteria (irPRC), a set of categorical histopathologic criteria developed for standardized pathologic assessment of the regression bed of neoadjuvant immunotherapy treated solid tumors.[17] Using these criteria, we also observed a significant association between the presence of intratumoral TLS and MPR/CR (P = 0.02), while no significant association was detected between peritumoral TLS and MPR/CR (P = 0.38) (**Extended Data Table 3**). Thus, both a quantitative assessment of TLS density and a categorical evaluation of individual pathologic features suggested that intratumoral TLS density may be most correlated with response to treatment.

We next examined relapse free survival and overall survival in the treated cohort, excluding the untreated cohort from analysis lack of follow up data for the majority of the cohort. Significantly longer relapse free survival after surgery was observed in treated patients in the upper tertile of intratumoral TLS density compared to patients in the middle and lower tertiles *(*P = 0.021) *(***Fig. 1e**). At a median follow up of 38 months for patients in the upper tertile of intratumoral TLS density and 32 months for patients in the middle and lower tertiles, median RFS was not reached in the upper tertile and 9.1 months in the middle and lower group. RFS at 30 months was 100% and 38.5% (95% CI, 19.3% to 76.5%), respectively. No significant difference in overall survival (OS) was observed between the two groups (P = 0.24) (**Fig. 1f**), but at 30 months OS was 100% in the upper tertile and 76.9% (95% CI, 57.1% to 100%) in the middle and lower tertiles. In addition, we observed a trend toward improved RFS for patients in the upper tertile of total TLS density compared to the middle and lower tertiles (P = 0.13) (**Extended Data Fig. 2a**). OS was not significantly different (P = 0.28) (**Extended Data Fig. 2b**), but no deaths were observed in the upper tertile of total TLS density while three deaths were observed in the middle and lower tertiles. With respect to peritumoral TLS density, no difference was observed in relapse free survival (P = 0.56) or overall survival (p = 0.23) when comparing the upper tertile to the middle and lower tertiles (**Extended Data Fig. 2c-d**). Notably, in this cohort MPR/CR, which was closely associated with high TLS density, was also associated with superior RFS (P = 0.025) (**Extended Data Fig. 2e**). No significant difference was observed in OS (P = 0.16) (**Extended Data Fig. 2f**), but no deaths were observed in the MPR/CR group while three deaths were observed in the pPR/NR group. In addition, we also evaluated outcomes according to sex and previous viral HBV or HCV infection and identified no significant differences in RFS or OS (**Extended Data Fig. 2g-l**). Finally, to compare the different clinical covariates, we used the Bayesian information criterion[18] to quantify the strength of each parameter in predicting relapse free survival or death after neoadjuvant ICB and surgical resection. The strongest predictors of relapse free survival by BIC analysis were intratumoral TLS density and pathologic response (**Extended Data Table 4**).

High TLS density after neoadjuvant ICB is associated with increased T and B cell activation and an expanded intratumoral T and B cell repertoire

To identify differences in gene expression between tumors with high and low TLS density in this treatment context, we performed bulk RNA sequencing from FFPE surgical resection specimens. Tissue sections were collected from 14 tumors in the neoadjuvant treatment group, of which 2 samples were excluded after quality control. The resultant 12 samples were designated as TLS high (n = 5) or TLS low (n = 7) according to total TLS density relative to the mean total TLS density of the treatment group. Here, total TLS density was used rather than intratumoral or peritumoral TLS density since bulk sequencing of FFPE tissue blocks did not have spatial resolution to account for these differences. By principal component analysis, the 5 TLS high tumors and 1 TLS low tumor clustered separately from the remaining TLS low tumors (**Fig. 2a**). Differential expression analysis using the R package DESeq2 identified 814 differentially expressed genes (DEG), defined as having fold change in the TLS high group greater than 2 times that of the TLS low group and false discovery rate less than 0.05 (**Fig. 2b-c** and **Extended Data Table 5)**.

Compared to TLS low tumors, TLS high tumors demonstrated significant overexpression of multiple genes belonging to the Gene Ontology Biological Pathways gene sets for T and B cell activation, cytokine production, and antigen presentation, including *CTLA4*, *IL7R*, *IL6*, the B cell activating factor BAFF(*TNFSF13B*) and its receptors BAFF-R (*TNFRSF13C*) and TACI (*TNFRSF13B*), and the T cell-derived cytokine *IL17C*. TLS high tumors displayed significantly greater expression of *CCL19*, a chemokine involved in T-cell and B-cell migration to secondary lymphoid organs, and *CXCR5*, the receptor for the B-cell chemoattractant *CXCL13*. TLS high tumors also demonstrated increased expression of multiple B-cell related genes such as the B cell antigen CD79 (*CD79A* and *CD79B*), CD20 (*MS4A1*), and Fc Receptor Like A protein (*FCRLA*) which is highly expressed in germinal center B cells.[19] In addition, we found increased expression of immunoregulatory genes including *IL10*, *IL17REL*, and the integrin αvβ8-mediated *ITGB8*, which mediates TGF-beta-1 activation on the surface of regulatory T cells.[20,21] We also identified significantly increased expression of the gene encoding the germinal center regulatory protein EBI2 (*GPR183*), *DOCK10*, which regulates CD23 expression and sustains B-cell lymphopoiesis in secondary lymphoid tissue,[22] and *WDFY4*, a mediator of dendritic cell cross presentation.[23]

Gene set enrichment analysis for human gene sets in the MSigDB collections further identified significant enrichment in TLS high tumors of pathways associated with increased adaptive immune response, including Hallmark pathways for allograft rejection and inflammatory response, and multiple pathways related to T and B cell receptor activation (**Fig. 2d-e** and **Extended Data Table 6**). Consistent with these findings, TLS high tumors also displayed increased expression of the 12-chemokine gene signature which has previously been found in association with TLS formation in multiple solid tumor types (**Extended Data Fig. 3a**).[24] Taken together, these bulk gene expression data demonstrate that tumors with high TLS density display significantly higher levels of T and B cell activation compared to TLS low tumors.

To determine if TLS density was associated with differences in the adaptive immune repertoire, we used the Personalis ImmunoID NeXT platform to extract immunoglobulin heavy chain (IGH), TCRβ, and TCRα repertoire data from bulk RNA sequencing data. Statistical power was limited by the small sample size, but in tumors with high TLS density there were a significant increase in total number of immunoglobulin heavy chain (IGH) clones (P = 0.02), unique clonotypes (P = 0.029), and repertoire diversity (P = 0.043) by Wilcoxon rank sum test (**Extended Data Fig. 4a-c**). In addition, we identified a trend toward increased median number of total clones, unique clonotypes, repertoire diversity in the TCRα (P = 0.29, 0.18, and 0.18, respectively, by Wilcoxon rank sum test) (**Extended Data Fig. 4d-f**) and TCRβ repertoires (P = 0.22, 0.095, and 0.095, respectively, by Wilcoxon rank sum test) (**Extended Data Fig. 4g-i**). Overall, these findings suggest that high TLS density is associated with an expansion of the B and T cell repertoire in HCC treated with neoadjuvant immunotherapy.

In areas of tumor regression, an involuted TLS morphology is found that displays dissolution of the B cell germinal center, retention of the T cell zone, and increased expression of T cell memory markers

Based on these data, we hypothesized that a distinctive immunological process may occur in tumors with high intratumoral TLS density and major or complete pathologic response that contributes to long-term disease-free survival. To evaluate this hypothesis, we performed histologic examination of tumors with both viable tumor and extensive tumor regression beds. In viable tumor, the predominant phenotype observed was the canonical 'mature' stage of TLS characterized by a $CD20^+$ B cell germinal center surrounded by $CD4^+$ and $CD8^+$ T cells.[25] TLS of this morphology showed characteristically high expression of the follicular dendritic cell marker CD21 and the proliferation marker Ki67. In contrast, in areas of tumor regression bed we observed an 'involuted' TLS morphology characterized by $CD20^+$ B cells in a halo-like ring surrounding a central core of $CD4^+$ and $CD8^+$ T cells. CD21 and Ki67 expression were low to absent (**Fig. 3a**). To confirm that this involuted morphology was not an artifact of sectioning, we performed serial sectioning and anti-CD20 staining of FFPE tissue sections and confirmed the absence of a dense B cell core as is seen in mature TLS (**Extended Data Fig. 5a**). These involuted TLS were highly associated with tumors with complete pathologic response, and in several tumors were found in series (**Extended Data Fig 5b**), suggesting a shared lymphatic supply. No TLS of this morphology were detected in untreated tumors.

Given the location of the latter morphology within areas of nonviable tumor and the dispersed appearance of B cells in these lymphoid aggregates, we hypothesized that this morphology may represent TLS undergoing shutdown of the germinal center.[26,27] To characterize the features of this stage of TLS, we developed a 38-marker imaging mass cytometry antibody panel. Markers included in this panel were selected to identify different T cell subsets (CD3, CD4, CD8, FOXP3, CXCR3, CXCR5, ICOS), B cells subsets (CD20, BCL6, AID, CD138), follicular dendritic cells (CD21, CD23), dendritic cells (CD11c, DC-LAMP, CCR7), high endothelial venules (PNAd), macrophages (CD68), fibroblasts (Podoplanin [PDPN], αSMA), and tumor (CK). We included markers for T cell activation and exhaustion (CD25, CD69, CD137, PD-1, LAG3, TOX), co-stimulatory or antigen presenting molecules (CD86, HLA-DR), and markers of cell proliferation (Ki67) (**Extended Data Tables 7 and 8**). FFPE sections were obtained from the tumors of 9 patients treated with neoadjuvant ICB, in 8 of which the involuted morphology was identified, and, after whole-slide staining, 31 regions of interest (ROI) were captured by laser ablation (**Extended Data Fig. 6a**) from which 38 TLS areas (n = 20 mature and 18 involuted) were identified.

Consistent with previously published data, imaging mass cytometry of mature TLS (**Fig. 3b**) demonstrated dense B cell follicle-like structures surrounded by peripherally located $CD4^+$ and $CD8^+$ T cells with associated high endothelial venules (HEV) with a cuboidal morphology.[28,29] In multiple HEV, we observed $CD8^+$ T cells in transit through these structures (**Fig. 3b, far left inset**). Mature TLS were also notable for an extensive CD21 and CD23 follicular dendritic cell network (**3b, middle left inset**), a distinct T cell zone with densely concentrated $DCLAMP^+$ mature dendritic cells in close contact with T cells (**3b, middle right inset**), and a dense $PDPN^+$ stromal network, similar to the fibroblastic reticular cell networks seen in secondary lymphoid organs[15,30] (**3b, far right inset**). Involuted TLS (**Fig. 3c**) showed no detectable HEV with a cuboidal morphology, scattered CD21 and CD23 expression, and diminished PDPN expression, consistent with attenuation of the TLS structure. Notably, the center of involuted TLS demonstrated apparent persistence of the T cell zone with co-location of $DCLAMP^+$ mature dendritic cells and $CD4^+$ and $CD8^+$ T cells.

Further quantitative analysis of these structures supported these initial observations. After cell segmentation, we identified 61,371 single cells which were assigned to 16 distinct cell clusters (**Fig. 3d-f** and **Extended Data Fig. 6b-c**). In mature TLS we observed significantly higher density of a BCL6^{high} population of B cells (B_BCL6^{high}), which was consistent with a germinal center B cell population (P = 0.00023). In mature TLS, this cluster localized to the center of the B cell germinal center in close proximity to CD21^{+}CD23^{+} follicular dendritic cells and demonstrated high expression of HLADR, a marker of antigen presentation, and CD86, a B cell activation marker, consistent with an activate B cell population. A second B cell cluster was identified on the periphery of the B cell follicle which displayed lower expression of BCL6 (B_BCL6^{low}) and decreased expression of HLADR and CD86. This cluster was also found in significantly higher density in mature TLS (P = 0.038). In contrast, in involuted TLS we observed significantly increased density of a third B cell cluster (B_AID+) (P = 0.0026), which was characterized by high expression of activation-induced cytidine deaminase (AID), the B cell enzyme which drives somatic hypermutation and class switch recombination. AID is induced by BCR cross-linking and has a half-life of 2.5 hours in the nucleus and 18-20 hours in its cytoplasmic form,[31,32] thus this population may correspond to B cells undergoing somatic hypermutation or memory B cells which had recently undergone immunoglobulin class switching, the latter of which we felt to be more likely given the context. No difference was observed in plasma cell densities between the two morphologies.

In the T cell compartment, we identified a single cytotoxic CD8^{+} T cell population (Tc) and two major CD4 T helper populations, a CD4^{+}CXCR5^{-}CXCR3^{+} T peripheral helper (Tph) cluster, which was located around the peripheral of the B cell germinal center in mature TLS and at the center of involuted TLS, and a CD4^{+}CXCR3^{-} T helper (Th_CXCR3^{low}) clusters. In location and marker expression, Tph in these data were consistent with CD4^{+} Tph that have been identified in patients with autoimmune disease, where they are thought to play a T follicular helper (Tfh)-like role in promoting pathogenic B cell responses in non-lymphoid tissue.[33–35] In contrast to changes observed in the B cell compartment, no significant difference was observed in density of CD4^{+} T cell clusters or the cytotoxic Tc cluster.

Clustering analysis also identified a CD4^{+}CD57^{+} cluster (Th_CD57^{+}) within the germinal center of mature TLS, which may provide help to B cells and induce class switch recombination,[36–38] a cluster of CD4^{+}FOXP3^{+} regulatory T cells (Th_FOXP3^{+}), a cluster of cytotoxic T cells (Tc); CD4^{+} and CD8^{+} T cells defined by high expression of granzyme B (GZMB^{+} T cell); proliferating T and B cells defined by high expression of Ki67 (Proliferating T and B); a macrophage cluster with high expression of CD68; a mature dendritic cell cluster defined by the presence of high expression of DCLAMP and CCR7[39]; a high endothelial venule (HEV) cluster defined by expression of the protein peripheral node addressin (PNAd); and a tumor cluster with high expression of Cytokeratin (CK) and PDL1. In mature TLS compared to involuted TLS, there was significantly higher density of proliferating T and B cells (P = 0.022), HEV (P = 0.00028), and tumor (P = 0.0026). On the other hand, density of mature dendritic cells was increased in involuted TLS (P = 0.025).

To further evaluate the spatial relationships between different cell types in the mature and involuted morphologies, we performed nearest neighbor analysis of the top 2 most frequent cell neighbors for each cell cluster (**Fig. 3g**). As in previous the above analyses, neighborhood analysis showed that the primary differences in spatial relationships between the two morphologies occurred in B cell clusters. In particular, in the mature morphology BCL6^{high} germinal center B cell cluster were first and second nearest neighbors for themselves, consistent with a highly concentrated germinal center. In contrast, in the involuted TLS morphology the most common first neighbor of this cluster was the BCL6^{low} cluster, consistent with a more dispersed germinal center in the involuted TLS. On the other hand, Tph were the most common non-self

neighbors for GZMB T cells, mature dendritic cells, proliferating T cells, and FOXP3$^+$ Tregs in both mature and involuted TLS, suggesting that the spatial relationships of these clusters was preserved across the two morphologies despite changes occurring in the B cell germinal center. Network analysis, which we used to visualize the average distances between cell clusters and cell cluster abundance across the two TLS morphologies, demonstrated similar changes to the two B cell clusters (B_BCL6^{high} and B_BCL6^{low}) occupying the germinal center and preservation of spatial relationships between mature dendritic cells, Tph, FOXP3$^+$ T cells, proliferating T and B cells, and GZMB$^+$ T cells is mature and involuted TLS (**Fig. 3h**). Overall, these neighborhood and network analyses suggested that while the B cell germinal center appeared to undergo dissolution in involuted TLS, the T cell zone was preserved.

Finally, evaluation of individual marker expression by cluster supported these observations regarding persistence of the T cell zone (**Fig. 3i**). In the mature dendritic cell cluster, expression of CCR7, HLADR, and CD86 were significantly increased, implying ongoing antigen presentation in these structures, and both the Tph and Tc clusters demonstrated increased expression of markers of antigen experience, including CD45RO, CD25, PD1, and TOX expression While the precise role of TOX in T peripheral helper cells is not established, TOX2 has previously been shown to be involved in the establishment of durable GC Tfh memory.[40] Taken together, these data suggest that the involuted morphology may be a site of persistent antigen presentation by mature dendritic cells, which drive the formation of antigen-experienced memory T cell populations.

Expanded T cell clonotypes are shared across TLS within a tumor, while B cell repertoires of individual TLS are highly distinct

Based on these data, we next sought to determine whether there were differences in the T and B cell repertoires of TLS of these two morphologies. We microdissected 38 individual TLS (32 mature and 6 involuted) from 7 treated tumors and performed bulk sequencing using the Adaptive ImmunoSEQ TCRβ and IGH assays (**Fig. 4a, Extended Data Fig. 7a, Extended Data Table 9**). After filtering to remove repertoires with low counts, 35 TCRβ repertoires and 32 IGH repertoires were analyzed. Across all samples, the repertoire size was variable with a mean total TCRβ clonotypes of 7171±8472 **(Extended Data Fig. 7b**). Singleton clonotypes comprised 68.7±13.4% of the TCRβ repertoire in all TLS sampled. In mature TLS, singleton clonotypes comprised 72.02±9.83% of the T cell repertoire, while in involuted TLS the singleton compartment constituted 48.98±16.1%. Across TLS microdissected from the same tumors, a mean of 32.3±12.3% of unique TCRβ clonotypes could be identified in other TLS from the same tumor. TCRβ clonotypes identified in all TLS from the same tumor were highly expanded, while those found in only one TLS were predominantly singletons (**Fig. 4b-c and Extended Data Fig. 7c-h**), suggesting a high degree of T cell trafficking as well as significant local T cell repertoire diversity at each individual TLS.

Across all microdissected TLS, the mean total number of IGH clonotypes was 922±1188 (**Extended Data Fig. 8a**). Singleton clonotypes comprised 95.3±3.9% of IGH repertoire of all TLS sampled. In mature TLS, singleton clonotypes comprised 95.7%±4.0 of the IGH repertoire, while in involuted TLS the singleton compartment constituted 93.4±3.1%. IGH repertoire sharing was significant lower across TLS microdissected from the same tumor (P = 7.6e-15), with only 6.7±5.6% of unique IGH clonotypes of each TLS detected in other TLS from the same tumor (**Fig. 4d-f** and **Extended Figure 7b-g**). These B cell repertoire characteristics are consistent with highly distinct, independent germinal center reactions.

In three patients (P12, OT1, and OT6) in which mature and involuted TLS were present in the same tissue block, we compared the immune repertoires of these two morphologies. TCRβ clonality was significantly increased in mature TLS compared to involuted TLS (P = 0.023) (**Fig. 4g**), although this difference was primarily observed in a single patient OT6 (**Extended Data Fig. 7i**). No difference was observed in IGH clonality (**Extended Data Fig. 7g**), but the IGH repertoire of involuted TLS did demonstrate a significantly higher number of V gene substitutions, a surrogate for somatic hypermutation (P < 2.22e-16) (**Fig. 4h** and **Extended Fig. 8i**). Taken together, these comparisons suggest that B cell populations in involuted TLS have undergone greater antigen-driven positive selection, consistent with a late-stage germinal center, and that there is associated T cell repertoire contraction and clonal expansion at these structures.

Given the extensive sharing of expanded T cell clonotypes observed within TLS from the same tumor, we also evaluated the peripheral blood to determine the extent of T cell trafficking between TLS and peripheral blood. We performed TCRβ sequencing of pre- and post-treatment peripheral blood mononuclear cells from 5 of the 7 patients whose TLS were microdissected. In TLS from these 5 patients, a mean of 44.0±8.4% of unique TCRβ clonotypes and 52.7±8.5% of total clonotypes in TLS were also identified in post-treatment peripheral blood. Similar overlap was observed between TLS repertoires and pre-treatment peripheral TCRβ repertoires, where a mean of 40.4±11.5% of unique TCRβ clonotypes and 48.7±11.0% total clonotypes in TLS were identified in pre-treatment peripheral blood (**Extended Data Fig. 9a-b**). In 3 of the 5 patients, 13 unique TCRβ were significantly expanded after neoadjuvant treatment and 9/13 (69.2%) were detected in at least one TLS (**Extended Data Table 10**). Together, these data provide evidence for a high degree of overlap between T cells within TLS and T cells in the peripheral blood.

The top expanded T cell clonotypes in mature TLS are cytotoxic granzyme K and granzyme B-expressing CD8$^+$ T cells

To further characterize T and B cell populations identified in TLS, we performed single cell RNA/TCR/BCR sequencing of post-treatment peripheral blood from the 7 patients from whose tumors TLS were microdissected. Sequencing of tumor infiltrating lymphocytes (TIL) was also performed for all 7 patients, but in only one sample (patient OT6) was sequencing data of sufficient quality for further analysis. Peripheral blood and TIL samples were processed by fluorescence-activated cell sorting (FACS) after labeling with antibodies to CD3 and CD19. After pre-processing and filtering to remove low quality sequencing data, 28,694 single cells were identified in the peripheral blood and 620 in the TIL. After performing preliminary cluster annotation using a reference annotated dataset, we attempted to match the TCRβ and IGH CDR3 amino acid sequences identified in microdissected TLS with sequences identified in the single cell dataset. TCRβ in the microdissection and single cell datasets were successfully matched (described below), but no matching IGH were identified between the bulk sequencing performed on microdissected TLS and single cell sequencing data, therefore B cells were excluded from subsequent analysis.

The resultant 23,172 T cells in the post-treatment peripheral blood samples and 562 T cells in the TIL of patient OT6 were clustered into 16 distinct cell clusters based on expression of canonical genes associated with specific T cell subsets. The CD4 compartment of the single cell dataset was divided into a naïve CD4$^+$ T cell cluster (CD4 Naïve) expressing high levels of *CCR7* and *LEF1*; a CD4 Naïve-like cluster (CD4 Naïve-like) characterized by expression of *CCR7 and TCF7*; a CD4 T central memory cluster (CD4 TCM) with high expression of *LTB and S100A4*; a CD4 T peripheral helper cluster (Tph) characterized by low expression of *CXCR5,* high expression of *CXCR3,* and high expression of ICOS; and two CD4 T effector memory clusters notable for high expression of granzyme K (CD4 TEM_GZMK) and granzyme B (CD4 TEM_GZMB). CD8 T cells

were divided into the following clusters: a naïve cluster (CD8 Naïve) highly expressing *CD8B*, *CCR7*, *LEF1*; a CD8 T central memory cluster (CD8 TCM) with elevated expression of *CD8B and LINC02446*; two CD8 T effector memory clusters distinguished by high expression of granzyme K (CD8 TEM_GZMK) and high expression of granzyme B (CD8 TEM_GZMB); and a CD8 tissue resident memory-like cluster (CD8 TRM) with increased expression of *NR4A2*, *DUSP2*, and *ZNF683.* In addition, we identified a CD4 regulatory T cell cluster (Treg) with high expression of *FOXP3* and *RTKN2*; an NK-T cell cluster (NK-T) highly expressing *PRF1* and *GZMB*; a double negative T cell cluster (dnT) with high expression of *SYNE* and *MALAT1*; a gamma delta T cells (gdT) with high expression of *TRDV2* and *TRGV9*; and mucosal invariant T cells cluster (MAIT) highly expressing *KLRB1* and *SLC4A10* (**Fig. 5a-c** and **Extended Data Fig. 10a-b**). In the TIL of patient OT6, 11 of 16 clusters were identified: CD4 Naïve-like, CD4 TCM, CD4 Tph, CD4 TEM_GZMK, CD8 TCM, CD8 TEM_GZMK, CD8 TEM_GZMB, CD8 TRM, Treg, dnT, and MAIT **(Extended Data Fig. 11a-c**).

19,546/23,172 (84.3%) single cells in the peripheral blood dataset and 346/562 (61.6%) cells in the TIL had a partial or completely sequenced TCRαβ chain identified by single cell TCR sequencing, of which there were 15,016 and 256 unique TCRs, respectively (**Extended Data Table 11**). In the peripheral blood single cell dataset, clonal expansion was most strongly associated with the CD4 TEM_GZMB (Odds Ratio 31.48, $P < 0.001$) and CD8 TEM_GZMB clusters (Odds Ratio 17.99, $P < 0.001$) by Fisher's Exact test (**Fig. 5d** and **Extended Data Table 12**). In TIL, clonal expansion was most strongly associated with the CD8 TEM_GZMB (Odds Ratio 3.49, $P = 0.003$), CD8 TRM (Odds Ratio 2.57, $P = 0.041$), and CD8 TEM_GZMK (Odds Ratio 1.94, $P = 0.013$) clusters (**Extended Data Fig. 11d and Extended Data Table 12).**

T cells belonging to the CD8 TEM_GZMK cluster were notable for increased expression of the gene associated with cytotoxicity, including Granzyme K (*GZMK*) and the chemokine ligand CCL5 (*CCL5*) and decreased expression of Granulysin (*GNLY*). The CD8 TEM_GZMB clusters also demonstrated hallmarks of cytotoxicity, including elevated expression of granzyme B (*GZMB*) and granzyme H (*GZMH*), as well as elevated expression of perforin (*PRF1*), and *GNLY* (**Extended Data Fig. 10c-d**).[41] *GZMK* expression was low in the latter cluster. These two transcriptional phenotypes were consistent with T progenitor exhausted and cytotoxic/terminally differentiated CD8 T cell states, respectively, which have been previously identified in the peripheral blood and tumors of patients treated with ICB.[41] Consistent with this identity, in the TIL from patient OT6, both *GZMK* and *GZMB* expressing CD8 clusters showed increased expression of multiple T cell exhaustion markers, including *PDCD1*, *CTLA4*, *LAG3*, *TIGIT*, and *TOX*, which were more highly expressed in CD8 TEM_GZMB compared to CD8 TEM_GZMK. *NKG7* and *CCL5*, which are associated with cytotoxic CD8 T cells, were also increased in both clusters, with higher expression in the GZMB high cluster (**Extended Data Fig 11h-i**). Notably, both clusters in the single cell TIL from patient OT6 demonstrated elevated expression of the B cell chemoattractant *CXCL13*, which has been associated with tumor-specific T cells in single cell sequencing studies of TIL from patients treated with ICB and is involved in the formation of TLS.[42,43]

No $CD4^+$ T cell cluster was observed in the single cell data that displayed a transcriptional phenotype consistent with a $CD4^+$ T follicular helper (Tfh) population, which are defined by high expression of CXCR5, CXCR3, and ICOS. Instead, we identified a $CD4^+$ T cell cluster consistent with the T peripheral helper cluster identified by imaging mass cytometry. In the peripheral blood, cells belonging to this cluster demonstrated low CXCR5 expression, increased CXCR3 expression, and elevated expression of CTLA4, TIGIT, and TOX (**Extended Data Fig. 10e**). Cells belonging to this cluster in the single cell TIL demonstrated increased expression of *CXCL13*, *ICOS*, *PD1*, *MAF*, *TOX* and high expression of multiple exhaustion markers including *CTLA4*, *LAG3*, *TIGIT*, *HAVCR2*, and *TNFRSF18 (GITR)* (**Extended Data Fig 11j**). Based on these data

and the imaging mass cytometry above, we conclude that Tph constitute a major $CD4^+$ T cell subset found in TLS in the context of neoadjuvant immunotherapy.

Approximately one-third, or 6349/19546 (32.5%), of single cells with a TCRβ in the peripheral T cell dataset and 199/346 (77.7%) single cells with a TCRβ in the TIL were identified in at least one TLS (**Extended Data Table 11**). TCRβ identified in TLS were detected in all clusters of the peripheral and TIL single cell dataset. Among peripheral blood T cells, the clusters most strongly associated with TLS were CD4 TEM_GZMB (Odds Ratio 10.72, $P < 0.001$), CD8 TEM_GZMB (Odds Ratio 9.73, $P < 0.001$), and CD8 TEM_GZMK (Odds Ratio 9.46, $P < 0.001$) (**Fig. 5e-f** and **Extended Data Table 13**), suggesting that TLS specifically promote the trafficking of effector memory $CD4^+$ and $CD8^+$ T cell populations from the peripheral blood to tumor. In the TIL, no cluster was significantly correlated with TLS but the Treg cluster was inversely correlated with presence in TLS (Odds Ratio 0.22, $P = 0.003$) (**Extended Data Fig. 11e-f** and **Extended Data Table 13**). The proportion of all TCRβ identified in TLS that were matched to single cell data was low overall (2,908/135,909 unique clonotypes or 2.1%), but a higher proportion of clonotypes were successfully matched for the most expanded clones, with 369/1359 (27.2%) of the top 1% of TCRβ that had been identified in TLS being successfully matched to the single cell data, and 63/137 (46%) of the top 0.1% of TCRβ (**Extended Data Table 14**). Thus, this approach, while providing a limited view of singleton TCRβ identified in TLS, could be used to provide additional transcriptional information about expanded T cell populations trafficking to TLS.

We next used these data to infer the transcriptional phenotype of T cells trafficking through TLS. Since our single cell dataset contained peripheral blood and TIL data, we first evaluated the correlation between peripheral blood and TIL phenotypes, and the reliability of using data from single cell sequencing from one compartment to infer the properties of single cells with the same TCRβ in the other compartment. To carry this out, we examined the correlation between single cell cluster identity for TCRβ which were found in both peripheral blood and TIL in patient OT6. In total, 16 unique TCRβ sequences were present in both peripheral blood and TIL (**Extended Data Fig. 11a**). 7/16 TCRβ clonotypes had the same single cell identity for all cells with the same TCRβ in the peripheral blood and TIL, and an additional 5/16 TCRβ had the same cluster identity assigned to at least half of the cells in both peripheral blood and TIL. In only 4/16 TCRβ were the cluster identities of cells with the same TCRβ entirely discordant (**Extended Data Fig. 11b).** Based on these data, we concluded that the peripheral blood transcriptional phenotype closely recapitulates the cluster assignment of TIL, and thus both identities may be used to determine a putative phenotype for T cells identified in TLS by TCRβ sequencing. These findings were consistent with previous work demonstrating that in circulating TILs, gene signatures of effector functions, but not terminal exhaustion, reflect those observed in the tumor.[44]

Across all 7 patients, the majority of T cells identified by matching of the TCRβ were GZMK and GZMB expressing CD8 T effector memory cells, but we also observed CD4 TEM_GZMK, CD4 CTL, and CD4 T peripheral helper clusters among the putative phenotypes of T cells trafficking through TLS (**Fig. 5g**). Notably, in the involuted TLS from the tumor of patient OT6, where we had previously noted significant increase in clonality relative to mature TLS, clonal expansion was greatest in the of CD8 TEM_GZMK, CD8 TEM_GZMB, and CD8 TRM clusters (**Fig. 5h** and **Extended Data Fig. 11k**). Overall, these data provide single cell resolution to the top expanded clonotypes in TLS and show that highly expanded T cell populations in TLS are $CD8^+$ T cell effector memory, which may undergo clonal expansion and repertoire contraction in concert with expansion of resident memory populations in areas of tumor regression.

DISCUSSION

Neoadjuvant immunotherapy aims to use the primary tumor as a source of antigens to enhance antitumor immunity and prevent cancer recurrence after surgery.[4] Preclinical and clinical data suggest that this approach induces more durable immunologic memory than adjuvant immunotherapy alone,[3] but the mechanism by which this occurs and the contribution of TLS to this process are not well understood. The data presented here show that in HCC treated with neoadjuvant immunotherapy, intratumoral TLS are associated with superior pathologic responses and improved relapse free survival. These findings are consistent with data reported in other solid tumors treated with ICB,[9–12] as well as studies of the prognostic significance of intratumoral TLS in treatment-naïve early stage HCC treated with surgical resection.[16] In tumors with high TLS density and significant regression of the tumor, we further identified an involuted morphology of TLS in areas of nonviable tumor whose location, histologic, and immunologic features, and similarity to late stage germinal centers observed in murine secondary lymphoid organs,[26] are consistent with a terminal stage of the TLS life cycle. Using laser capture microdissection, bulk immune repertoire sequencing, and matched single cell sequencing, we identify and characterize expanded T cell populations trafficking through TLS and find evidence for significant immune repertoire changes associated with TLS dissolution.

While TLS are thought to mature from a loosely organized lymphoid aggregate to a $CD21^+$ primary follicle and reach full maturity as a $CD21^+CD23^+$ secondary follicle,[16,45,46] which have distinct T and B cell zones,[25] the circumstances of TLS resolution are not known.[47] These data suggest that TLS dissolution may be driven by elimination of tumor and may occur dyssynchronously, with dissolution of the B cell germinal center accompanied by persistence of a T cell zone enriched for interactions between $DCLAMP^+CCR7^+HLADR^+$ mature dendritic cells and $CD4^+$ and $CD8^+$ T cells. Furthermore, the changes observed in T cell repertoire at these structures, including increase in clonality and expansion of cytotoxic and tissue resident memory-like $CD8^+$ T cell clonotypes, suggest that late-stage TLS may play a functional role in supporting the contraction and memory phase of the intratumoral adaptive immune response through persistent antigen presentation in the T cell zone (**Fig. 6**). Such a role would also be consistent with recent data suggesting that tonic antigenic stimulation drives programs of T cell residency in tumors, and would identify a specific place where such interactions may occur.[48]

Notably, in neoadjuvant treated tumors we did not detect a $CXCR5^+CXCR3^+CD4^+$ T follicular helper population, which have been reported in tumor associated TLS.[49,50] Rather, in both the imaging mass cytometry analysis and single cell datasets we identified a $CXCR5^-CXCR3^+$ $CD4^+$ T cell population, which expressed CXCL13 in the single cell TIL of patient OT6 and was also detectable in post-treatment peripheral blood single cell sequencing. $CXCR5^-$CXCL13-producing $CD4^+$ T cells have been identified in untreated human breast cancer under the name TFHX13[51,52] and in autoimmune disease, where they are termed $CD4^+$ T peripheral helper cells and have been shown to provide help to B cells in an IL-21 dependent manner.[34,35,53] This population was present in both the mature and involuted morphologies observed in these patients. Additional studies are required to determine whether this population of $CD4^+$ T cells provides help to B cells in this treatment setting, and to determine their role in involuted TLS, where they were found in association with mature dendritic cells.

We recognize several limitations of the findings reported here. First, samples were obtained from a single institution and may not represent the full diversity of HCC etiologies and subtypes. Additionally, while the untreated cohort in this study was similar to the treatment cohort in age, sex, and HCC etiology and received treatment at the same primary institution, we cannot exclude the possibility that the different pathologic findings between the untreated and neoadjuvant cohorts arose as a consequence of differences in the patient populations rather than treatment status. We infer the transcriptional phenotype of T cells infiltrating TLS based on matching TCRs

identified by microdissection with peripheral T cells and/or TIL subjected to single cell sequencing. In our data, we demonstrate a correlation between the cluster identity for 16 TCRs shared between the peripheral blood and TIL of patient OT6, and others have reported correlation between gene signatures of effector functions in circulating TILs and tumor;[44] however, it is possible that the phenotype of these T cells are not fully conserved outside of TLS. Finally, our analyses throughout are limited by small sample size. However, clinical samples from neoadjuvant studies are rare, and as we have shown here even small samples can provide important insights into the constituent immune populations in tumors arising in human subjects.

Finally, these data raise several important questions which future studies should address. First, the role of FOXP3$^+$ T follicular regulatory cells, which have been shown to regulate germinal center reactions,[54,55] is not completely understood in this context and this population could not be resolved in our imaging mass cytometry analysis. Second, while dispersion of the B cell follicle was associated with attenuation of the PDPN$^+$ fibroblastic reticular cell and the CD21$^+$CD23$^+$ follicular dendritic cell network in our data, other changes occurring in the fibroblast populations involved in this process remain unclear and it is not known what permits retention of mature dendritic cells within the T cell zone. Third, since all tumors in which involuted TLS were observed were treated with neoadjuvant ICB and these structures were not seen in untreated tumors, the contribution of therapy to their formation cannot be established from our data. In murine studies, both the PD-1 and CTLA-4 pathways have been shown to be involved in regulation of T follicular regulatory populations,[56–58] suggesting that therapeutic blockade may affect the dynamics of germinal center formation and dissolution. Nonetheless, these data shed light on the circumstances of TLS resolution and suggest that this terminal stage, about which nothing was previously known, may play a functional role in the formation of intratumoral T cell memory after elimination of viable tumor.

METHODS

Study design

The aim of this study was to characterize tertiary lymphoid structures (TLS) in patients with hepatocellular carcinoma (HCC) treated with neoadjuvant ICB-based therapy prior to surgical resection of the primary tumors. To understand the clinical significance of TLS, we analyzed TLS density in treated patients and untreated controls and correlated TLS density in treated patients against pathologic response and post-surgical clinical outcomes. We performed bulk RNA sequencing of tumors with high and low TLS density after neoadjuvant treatment to understand the gene expression programs of tumors with high TLS density. We then characterized the morphological and functional properties using bulk immune repertoire sequencing of TCRβ and IGH, imaging mass cytometry, matched single cell TCR and RNA sequencing of peripheral blood and tumor infiltrating lymphocytes.

Patient identification and data collection

Patients were identified for inclusion in this study if they received surgical resection for locally advanced, non-metastatic hepatocellular carcinoma after neoadjuvant ICB-based therapy between October 1, 2019 and January 31, 2022 at the Johns Hopkins Sidney Kimmel Cancer Center. Retrospective chart review was performed to collect clinical data from the electronic medical record regarding age at surgery, sex, date of resection, HCC etiology, histologic grade of tumor, neoadjuvant treatment, relapse free survival, and overall survival. A cohort of untreated control patients who had undergone surgical resection for HCC without prior systemic treatment were also identified via a search of the electronic medical record. Review of the electronic medical record was performed to confirm absence of prior systemic treatment. For both cohorts, histologic grade was based on pathologic assessment at the time of resection if there was discordance with

grade reported for pre-treatment biopsy. Patients in both cohorts were excluded from analysis if there was evidence of active hepatitis B (defined by a positive HBsAg or detectable HBV DNA) prior to surgery. Patients were excluded from the control group if the etiology of their HCC was not represented in the treatment group (e.g. hepatic adenoma and hereditary hemochromatosis). This study was conducted in accordance with the Declaration of Helsinki and was approved by the Johns Hopkins University Institutional Review Board (IRB00149350, IRB00138853, NA_00085595). Informed consent or waiver of consent was obtained from all patients. Treated patients identified with the letter P were accrued as participants in the phase I clinical trial NCT03299946.[8]

Histopathologic assessment of TLS density and pathologic response

Evaluation of pathologic response was performed by a hepatopathologist (RA). Pathologic response designations were assigned according to percent residual viable tumor in surgically resected tumors. Complete response (CR) was defined as 0% residual viable tumor, major pathologic response (MPR) as less than 10% residual viable tumor, partial pathologic response (pPR) as 10-90% residual viable tumor, and non-response (NR) as >90% residual viable tumor.[17] 12 of the 19 patients had previously undergone assignment of pathologic response according binary categorization of major or complete pathologic response versus non-response,[8] and for this group non-responders were categorized as NR or pPR as described above. To determine TLS density, formalin fixed paraffin embedded (FFPE) tumors were sectioned, mounted on glass slides, and stained with anti-CD20 antibody as described below. Whole slide images were obtained at 0.49 µm per pixel using the Hamamatsu NanoZoomer. The presence of CD20 positivity was determined by digital image analysis software (HALO v3.0.311 Indica Labs), with TLS defined as CD20 positive cell aggregates greater than 150µm in diameter located among tumor cells or at the invasive margin in areas of viable and nonviable tumor. TLS density was determined by calculating the number of TLS per mm^2 of viable and nonviable tumor. TLS were classified as peritumoral if they were found within 200 µm of the interface between normal adjacent parenchyma and tumor and intratumoral if they were found within the tumor or tumor regression bed.

Survival analyses

The Kaplan–Meier method was used to estimate relapse-free survival (PFS) and overall survival (OS). Relapse free survival (RFS) was defined as the time from surgical resection to radiographic relapse. Overall survival (OS) was defined as the time from surgical resection to death from any cause. If a patient was not known to have had either event, RFS and OS were censored at the last date of known healthcare contact. RFS and OS analyses were limited to patients treated with neoadjuvant therapy and were not performed in the untreated controls due to limited follow up in this cohort. Survival analyses using the Kaplan-Meier method were performed using the R package survminer. Bayesian information criterion (BIC) analysis was performed using the R package stats. A linear regression model was used to evaluate the effect of each marker, dichotomized by the mean, as a predictor of each distance measure. For each binary outcome, logistic regression was employed, with each marker treated as continuous. A meaningful difference in BIC between the two models is 2 at a minimum, and a difference between 5-10 and above 10 is considered to be strong and very strong, respectively.[59]

Immunohistochemistry

Automated single and dual staining was performed on the Leica Bond RX (Leica Biosystems). Single staining for CD20 was employed for determination of TLS density. Dual staining for CD3 and CD21, CD8 and CD4, Ki67 and CD20 was performed prior to laser capture microdissection of TLS. Slides were baked and dewaxed online followed by antigen retrieval for 20 min at 100°C. Endogenous peroxidase was blocked using Peroxidase block (Refine Kit) followed by Protein

722 block (X090930-2, Agilent Technologies Inc., Santa Clara, CA). Primary antibodies were applied
723 at room temperature. Detection was performed using the Bond Polymer Refine Kit (DS9800, Leica
724 Biosystems). For dual staining, a second round of antigen retrieval was performed for 20 min at
725 95°C followed by application of a second primary antibody. Detection of the second primary
726 antibody was performed using the Bond Polymer Red Refine Kit (DS9390, Leica Biosystems).
727 Slides were counterstained, baked and coverslipped using Ecomount (5082832, Biocare Medical,
728 Walnut Creek, CA). Antigen retrieval buffers and concentrations of all antibodies are listed in
729 **Extended Data Table 15**. Antibodies were diluted to appropriate working concentration using
730 Antibody Diluent (S302283-2, Agilent Technologies Inc).
731
732 **Bulk RNA sequencing and TCRβ/BCR immune repertoire profiling of FFPE tumor**
733 RNA was extracted from FFPE tumor from the treatment cohort and sequenced using the
734 commercial platform ImmunoID NeXT with 200 million paired end reads (150 base pair). Reads
735 were aligned in accordance with the Personalis Cancer RNA pipeline and transcript per million
736 (TPM) values were extracted.[60] Bulk RNA sequencing was performed on 14 tumors in two
737 batches. No batch correction was applied due to lack of clear batch-to-batch differences by
738 principal component analysis. 2 samples were excluded due to poor sequencing depth, as defined
739 by a median of the log2 transformed count data being equal to 0 for those samples. The remaining
740 12 samples were filtered to include only genes for which the sum of raw counts across all samples
741 was greater than 1. Variance stabilizing transformation was performed on the resultant data and
742 differentially expressed genes were identified using DESeq2.[61] Genes with an adjusted P value
743 of < 0.05, and a minimum log2 fold change of 1 were considered differentially expressed. Pathway
744 analysis was performed using the R package fsgsea to identify biologically enriched pathways
745 from the MSigDB hallmark gene sets.[62,63] For pathway analyses, adjusted P values of < 0.05 were
746 considered statistically significant. TCRβ and BCR repertoire profiling was performed using the
747 ImmunoID NeXT transcriptome, which provides augmented (approximately a 100x increase over
748 a standard transcriptome) coverage of TCRβ and BCR.[60,64] Clones were identified using MiXCR[65]
749 and repertoire analysis was performed using the R package immunarch.[66] Clonality was
750 calculated as 1-Shannon's equitability[67] with clonality values ranging from 0-1, with 0 indicating
751 equal representation of all clones within a repertoire and 1 being a repertoire consisting of only
752 one clone.
753
754 **IMC staining and acquisition**
755 IMC Staining was done as previously described.[8,68] Briefly, formalin-fixed paraffin-embedded
756 (FFPE) resected liver tissue sections were baked, deparaffinized in xylene, then rehydrated in an
757 alcohol gradient. Slides were incubated in Antigen Retrieval Agent pH 9 (Agilent PN S2367) at
758 96 °C for 1 hour then blocked with 3% BSA in PBS for 45 min at room temperature followed by
759 overnight staining at 4°C with the antibody cocktail. Antibodies, metal isotopes, and their titrations
760 are listed in **Extended Data Table 8**. Images were acquired using a Hyperion Imaging System
761 (Standard BioTools) at the Johns Hopkins Mass Cytometry Facility. Upon image acquisition,
762 representative images were visualized and generated through MCD™ Viewer (Standard
763 BioTools).
764
765 **IMC data analysis**
766 Images were segmented into a single-cell dataset using the publicly available software pipeline
767 based on CellProfiler, ilastik, and HistoCAT.[69–72] Since multiple images contained more than one
768 TLS, images were subset for distinct TLS regions by manual gating using FlowJo™v10.9.0
769 Software (BD Life Sciences), which identified the xy coordinates of cells belonging to distinct
770 lymphoid aggregates (**Extended Data Fig. 6b-c**). This resulted in 38 unique TLS matching either
771 the mature (n = 20) or involuted morphology (n = 18). The resulting 61,371 single cells were
772 clustered using FlowSOM[73] into metaclusters, which were manually annotated into final cell types.

773 Density of each cell type was determined by calculating the number of cells per unit area as
774 determined by ImageJ v1.53.[74] For network visualization, the mean distance between each cell
775 type was computed and visualized using the R package qgraph.[75] Neighborhood analysis was
776 performed by using data generated by HistoCAT summarizing the top neighboring cell types for
777 every cell type.
778
779 **Laser capture microdissection and TCRβ/IGH sequencing of microdissected TLS**
780 10-14 μm serial tissue sections were obtained from formalin-fixed paraffin embedded (FFPE)
781 tumor tissue blocks and mounted on UV activated PEN membrane glass slides (Applied
782 Biosystems Cat. No. LCM0522) with additional 4-μm tissue sections cut every 150 μm for staining
783 with hematoxylin and eosin (H&E) and dual IHC for CD3/CD21, CD8/CD4, and Ki67/CD20 as
784 described above. Stained sections were scanned at 20x objective equivalent (0.49 μm $pixel^{-1}$) on
785 a digital slidescanner (Hamamatsu Nanozoomer) in advance of microdissection and annotated
786 using NDP.view2 viewing software in order to identify areas for microdissection. On the day of
787 microdissection, unstained tissue sections mounted on PEN membrane slides were
788 deparaffinized using xylene and graded alcohol washes and stained with H&E. Laser capture
789 microdissection of individual TLS was performed on the LMD 7000 system (Leica) and genomic
790 DNA was extracted using the Qiagen QIAamp DNA FFPE Tissue Kit following the manufacturer's
791 protocol (Qiagen). DNA concentrations were quantified with a Qubit 4 Fluorometer using the Qubit
792 dsDNA high sensitivity assay (Invitrogen). Sequencing of the TCRβ and IGH CDR3 regions was
793 performed using the immunoSEQ platform (Adaptive Biotechnologies).[76,77] TCRβ and IGH
794 repertoire data were downloaded from the Adaptive ImmunoSEQ analyzer web interface after
795 filtering to remove non-productive reads. After exclusion of repertoires with fewer than 500 TCRβ
796 clones and 50 IGH clones, subsequent analysis was performed using the R package immunarch[66]
797 and the Python package Change-O,[78] which was used to assign clonal families to IGH data. J
798 gene, and greater than 90% identical CDR3 sequence according to nucleotide hamming distance.
799 Clonality was calculated as described above using 1-Shannon's equitability. To compare clonality
800 across multiple TLS from the same tumor, we used the median clonality of 1000 iterations of
801 downsampling to the number of productive CDR3 sequences in the smallest TCRβ or IGH
802 repertoire for that patient.[79]
803
804 **Peripheral blood and fresh tumor collection and processing**
805 Processing of peripheral and cryopreservation was completed as previously described.[8] Fresh
806 tumor tissue was diced with a sterile scalpel and dissociated in 0.1% collagenase in RPMI 1640
807 for 60 minutes at 37ºC using the gentleMACS OctoDissociator (Miltenyi Biotec) according to the
808 manufacturer's instructions. Supernatant was collected and centrifuged at 1500 rpm for 10
809 minutes. Supernatant was removed and discarded, and the cell pellet was resuspended in ACK
810 Lysing buffer (Quality Biological, cat# 118-156-721) and incubated at room temperature for 5
811 minutes before centrifugation at 1500 rpm for 10 minutes. Cells were resuspended in PBS,
812 counted using a manual hematocytometer, and cryopreserved in 10% DMSO/AIM-V freezing
813 media.
814
815 **Single cell RNA/TCR/BCR-sequencing**
816 For all 7 patients from whose tumors TLS were microdissected, single cell sequencing was
817 obtained for peripheral blood T and B cells isolated by Fluorescent Activated Cell Sorting (FACS).
818 For 6 of 7 patients, the peripheral blood sample was obtained following completion of neoadjuvant
819 ICB and prior to surgical resection; for 1 of the patients, the peripheral blood sample was drawn
820 4 weeks after resection. In addition, in the latter patient, single cell sequencing was performed for
821 tumor infiltrating T and B cells isolated by FACS from tumor specimen. Cryopreserved PBMC and
822 tumor suspension were thawed and washed with pre-warmed RPMI with 10% FBS. Cells were
823 resuspended 0.04% BSA in PBS and stained with a viability marker (Zombie NIR, BioLegend)

824 and Fc block (Biolegend, Cat. no. 422302) for 10 minutes at room temperature in the dark. Cells
825 were then stained with antibodies against CD3 (FITC, clone HIT3a), for 20 minutes on ice and
826 CD19 (PE/dazzle, clone SJ25C1) (**Extended Data Table 16**). After staining, viable $CD3^+$ and
827 $CD19^+$ cells were sorted into 0.04% BSA in PBS using a BD FACS Aria II Cell Sorter at a 4:1
828 ratio. Sorted cells were counted and resuspended at a concentration of 1000 cells per µl. The
829 single-cell library preparations for gene expression and V(D)J were performed with the Chromium
830 Next GEM Single Cell 5' GEM Kit v2 (10x Genomics) and Chromium Single Cell V(D)J
831 Amplification Kit (human TCR) (10x Genomics), respectively. The cells were partitioned into
832 nanoliter-scale Gel Beads in-emulsion (GEMs) and cells were barcoded. The cDNA synthesis
833 and amplification was performed prior to sample split for the gene expression and for V(D)J
834 libraries. Single cell libraries were sequenced on an Illumina NovaSeq instrument using 2 × 150-
835 bp paired end sequencing. 5′ VDJ libraries were sequenced to a depth of 5,000 reads per cell. 5′
836 DGE libraries were sequenced to a depth of 50,000 reads per cell.
837
838 **Single cell data pre-processing, quality control, clustering and integration**
839 Cell Ranger v6.1.2 was used to demultiplex FASTQ reads, perform sequence alignment to the
840 GRCh38 transcriptome, and extract unique molecular identifier (UMI) barcodes. Single cell gene
841 expression matrices were analyzed using the R package Seurat v4.1.1 as a single Seurat object.
842 Cells were filtered to include only cells with less than 25% mitochondrial RNA content and
843 between 200 and 4000 genes detected. For single-cell VDJ sequencing, only cells with full-length
844 sequences were retained. Raw count data were normalized using the Seurat function
845 SCTransform to normalize raw count data to a Gamma-Poisson Generalized Linear Model,
846 perform variance stabilization, identify highly variable features, and scale features.[80,81] Cells were
847 projected into their first 50 principal components using the RunPCA function in Seurat, and further
848 reduced into a 2-dimensional visualization space using the RunUMAP function. Initial cell cluster
849 identification was performed using the Seurat function FindClusters at a resolution of 0.7. Initial
850 cell type assignment was performed by reference mapping to the human PBMC dataset
851 associated with the R package Azimuth.[82] Cluster identities were then manually assigned by
852 identification of differentially expressed genes using the MAST hurdle model as implemented in
853 the Seurat FindAllMarkers function with a log fold change threshold of 0.25 and minimum
854 fractional expression threshold of 0.25.[83] Integration of single cell TCR-seq and BCR-seq data
855 into the scRNA-seq data was performed using the R package scRepertoire.[84] For each patient,
856 TCRβ sequences identified in single cell data were compared against TCRβ identified in
857 microdissected TLS to identify T cells present in TLS. In cases where single cells with the same
858 TCR occupied multiple clusters, a putative transcriptional phenotype was assigned to a T cell in
859 the TLS repertoire according to the most common T cell subset to which the single cells with the
860 same TCR belonged. No matches were identified between IGH sequences identified by Adaptive
861 sequencing and IGH sequences in the single cell dataset, and thus we excluded B cells in the
862 single cell dataset from further analysis.
863
864 **Data availability**
865 Bulk RNA-seq, single cell RNA/TCR-seq data, and imaging mass cytometry data from this study
866 are deposited in dbGap under *** and the Gene Expression Omnibus (GEO) under accession
867 number GSE ***. Bulk TCRβ and IGH data from microdissected TLS are available on the Adaptive
868 ImmunoSEQ web analyzer portal at ***. All other relevant data are available from the
869 corresponding authors upon request.
870
871 **Code availability**
872 All custom code used to generate the results in this study has been deposited in a GitHub
873 repository at https://github.com/FertigLab/HCCTLS.
874

Acknowledgements

This work was supported by the Johns Hopkins SPORE in Gastrointestinal Cancer and the National Institutes of Health (NIH) U01CA253403 and U01CA212007 grants to M.Y. and E.J.F. Additional research support was provided by the Breeden-Adams Foundation and Conquer Cancer to M.Y.; the Johns Hopkins School of Medicine J. Mario Molina Physician Scientist Fund, Linda Rubin Fellowship, and Bernice Garchik Fellowship to D.S; and the Maryland Cancer Moonshot Research Grant to the Johns Hopkins Medical Institutions to D.J.Z. We thank Theinmozhi Arulraj for reviewing the final manuscript.

Author contributions

D.S., M.Y., and E.J.F. conceived and designed this study. D.S., L.K., M.Y., and L.D. performed data analysis and interpreted results. Q.Z. and R.A. performed the pathologic review. D.S., K.M., Q.Z., and R.A. performed the histologic analysis. All authors assisted with the data analysis, provided valuable discussion, and reviewed and edited the final manuscript draft. D.S. and M.Y. wrote the manuscript with input from all the authors.

Competing interests

M.Y. reports grant/research support from Bristol-Myers Squibb, Incyte, Genentech (to Johns Hopkins) and honoraria from Genentech, Exelixis, Eisai, AstraZeneca, Replimune, Hepion, and equity in Adventris Pharmaceuticals. E.J.F is on the Scientific Advisory Board of Viosera/Reistance Bio, is a paid consultant for Merck and Mestag Therapeutics, and receives research funds from Abbvie. W.J.H. has received patent royalties from Rodeo/Amgen and is the recipient of grants from Sanofi, NeoTX, and CirclePharma. He has received speaking/travel honoraria from Exelixis and Standard BioTools. E.M.J. reports grant/research support from the Lustgarten Foundation, Break Through Cancer, Genentech, Bristol-Meyers Squibb; honoraria from Achilles, DragonFly, Parker Institute, Cancer Prevention and Research Institute of Texas, Surge, HDT Bio, Mestag Therapeutics, Medical Home Group; and equity in AbMeta Therapeutics and Adventris Pharmaceuticals. D.J.Z. reports grant/research support from Roche/Genentech.

903 **REFERENCES**

904 1. Garon EB, Hellmann MD, Rizvi NA, et al. Five-Year Overall Survival for Patients With Advanced Non–
905 Small-Cell Lung Cancer Treated With Pembrolizumab: Results From the Phase I KEYNOTE-001 Study.
906 *J Clin Oncol Off J Am Soc Clin Oncol*. 2019;37(28):2518-2527. doi:10.1200/JCO.19.00934

907 2. Larkin J, Chiarion-Sileni V, Gonzalez R, et al. Five-Year Survival with Combined Nivolumab and
908 Ipilimumab in Advanced Melanoma. *N Engl J Med*. Published online September 27, 2019.
909 doi:10.1056/NEJMoa1910836

910 3. Patel SP, Othus M, Chen Y, et al. Neoadjuvant–Adjuvant or Adjuvant-Only Pembrolizumab in
911 Advanced Melanoma. *N Engl J Med*. 2023;388(9):813-823. doi:10.1056/NEJMoa2211437

912 4. Topalian SL, Forde PM, Emens LA, Yarchoan M, Smith KN, Pardoll DM. Neoadjuvant immune
913 checkpoint blockade: A window of opportunity to advance cancer immunotherapy. *Cancer Cell*.
914 Published online August 17, 2023. doi:10.1016/j.ccell.2023.07.011

915 5. Liu J, Blake SJ, Yong MCR, et al. Improved Efficacy of Neoadjuvant Compared to Adjuvant
916 Immunotherapy to Eradicate Metastatic Disease. *Cancer Discov*. 2016;6(12):1382-1399.
917 doi:10.1158/2159-8290.CD-16-0577

918 6. Liu J, O'Donnell JS, Yan J, et al. Timing of neoadjuvant immunotherapy in relation to surgery is
919 crucial for outcome. *Oncoimmunology*. 2019;8(5):e1581530. doi:10.1080/2162402X.2019.1581530

920 7. Chalabi M, Fanchi LF, Dijkstra KK, et al. Neoadjuvant immunotherapy leads to pathological
921 responses in MMR-proficient and MMR-deficient early-stage colon cancers. *Nat Med*.
922 2020;26(4):566-576. doi:10.1038/s41591-020-0805-8

923 8. Ho WJ, Zhu Q, Durham J, et al. Neoadjuvant cabozantinib and nivolumab convert locally advanced
924 hepatocellular carcinoma into resectable disease with enhanced antitumor immunity. *Nat Cancer*.
925 Published online July 29, 2021:1-13. doi:10.1038/s43018-021-00234-4

926 9. Cabrita R, Lauss M, Sanna A, et al. Tertiary lymphoid structures improve immunotherapy and
927 survival in melanoma. *Nature*. 2020;577(7791):561-565. doi:10.1038/s41586-019-1914-8

928 10. Petitprez F, de Reyniès A, Keung EZ, et al. B cells are associated with survival and immunotherapy
929 response in sarcoma. *Nature*. 2020;577(7791):556-560. doi:10.1038/s41586-019-1906-8

930 11. Helmink BA, Reddy SM, Gao J, et al. B cells and tertiary lymphoid structures promote
931 immunotherapy response. *Nature*. 2020;577(7791):549-555. doi:10.1038/s41586-019-1922-8

932 12. Vanhersecke L, Brunet M, Guégan JP, et al. Mature tertiary lymphoid structures predict immune
933 checkpoint inhibitor efficacy in solid tumors independently of PD-L1 expression. *Nat Cancer*.
934 2021;2(8):794-802. doi:10.1038/s43018-021-00232-6

935 13. Italiano A, Bessede A, Pulido M, et al. Pembrolizumab in soft-tissue sarcomas with tertiary lymphoid
936 structures: a phase 2 PEMBROSARC trial cohort. *Nat Med*. Published online May 26, 2022.
937 doi:10.1038/s41591-022-01821-3

938 14. Joshi NS, Akama-Garren EH, Lu Y, et al. Regulatory T Cells in Tumor-Associated Tertiary Lymphoid
939 Structures Suppress Anti-tumor T Cell Responses. *Immunity*. 2015;43(3):579-590.
940 doi:10.1016/j.immuni.2015.08.006

941 15. Rodriguez AB, Peske JD, Woods AN, et al. Immune mechanisms orchestrate tertiary lymphoid
942 structures in tumors via cancer-associated fibroblasts. *Cell Rep*. 2021;36(3):109422.
943 doi:10.1016/j.celrep.2021.109422

944 16. Calderaro J, Petitprez F, Becht E, et al. Intra-tumoral tertiary lymphoid structures are associated
945 with a low risk of early recurrence of hepatocellular carcinoma. *J Hepatol*. 2019;70(1):58-65.
946 doi:10.1016/j.jhep.2018.09.003

947 17. Cottrell TR, Thompson ED, Forde PM, et al. Pathologic features of response to neoadjuvant anti-PD-
948 1 in resected non-small-cell lung carcinoma: a proposal for quantitative immune-related pathologic
949 response criteria (irPRC). *Ann Oncol*. 2018;29(8):1853-1860. doi:10.1093/annonc/mdy218

950 18. Claeskens G, Hjort NL. *Model Selection and Model Averaging*. Cambridge University Press; 2008.
951 doi:10.1017/CBO9780511790485

952 19. Santiago T, Kulemzin SV, Reshetnikova ES, et al. FCRLA is a resident endoplasmic reticulum protein
953 that associates with intracellular Igs, IgM, IgG and IgA. *Int Immunol*. 2011;23(1):43-53.
954 doi:10.1093/intimm/dxq456

955 20. Lainé A, Labiad O, Hernandez-Vargas H, et al. Regulatory T cells promote cancer immune-escape
956 through integrin αvβ8-mediated TGF-β activation. *Nat Commun*. 2021;12(1):6228.
957 doi:10.1038/s41467-021-26352-2

958 21. Dodagatta-Marri E, Ma HY, Liang B, et al. Integrin αvβ8 on T cells suppresses anti-tumor immunity in
959 multiple models and is a promising target for tumor immunotherapy. *Cell Rep*. 2021;36(1):109309.
960 doi:10.1016/j.celrep.2021.109309

961 22. García-Serna AM, Alcaraz-García MJ, Ruiz-Lafuente N, et al. Dock10 regulates CD23 expression and
962 sustains B-cell lymphopoiesis in secondary lymphoid tissue. *Immunobiology*. 2016;221(12):1343-
963 1350. doi:10.1016/j.imbio.2016.07.015

964 23. Theisen DJ, Davidson JT, Briseño CG, et al. WDFY4 is required for cross-presentation in response to
965 viral and tumor antigens. *Science*. 2018;362(6415):694-699. doi:10.1126/science.aat5030

966 24. Coppola D, Nebozhyn M, Khalil F, et al. Unique Ectopic Lymph Node-Like Structures Present in
967 Human Primary Colorectal Carcinoma Are Identified by Immune Gene Array Profiling. *Am J Pathol*.
968 2011;179(1):37-45. doi:10.1016/j.ajpath.2011.03.007

969 25. Schumacher TN, Thommen DS. Tertiary lymphoid structures in cancer. *Science*. 375(6576):eabf9419.
970 doi:10.1126/science.abf9419

971 26. Jacobsen JT, Hu W, R. Castro TB, et al. Expression of Foxp3 by T follicular helper cells in end-stage
972 germinal centers. *Science*. 2021;373(6552):eabe5146. doi:10.1126/science.abe5146

973 27. Arulraj T, Binder SC, Meyer-Hermann M. Investigating the Mechanism of Germinal Center
974 Shutdown. *Front Immunol*. 2022;13. Accessed March 4, 2023.
975 https://www.frontiersin.org/articles/10.3389/fimmu.2022.922318

976 28. Milutinovic S, Abe J, Godkin A, Stein JV, Gallimore A. The Dual Role of High Endothelial Venules in
977 Cancer Progression versus Immunity. *Trends Cancer*. 2021;7(3):214-225.
978 doi:10.1016/j.trecan.2020.10.001

979 29. Asrir A, Tardiveau C, Coudert J, et al. Tumor-associated high endothelial venules mediate
980 lymphocyte entry into tumors and predict response to PD-1 plus CTLA-4 combination
981 immunotherapy. *Cancer Cell*. 2022;40(3):318-334.e9. doi:10.1016/j.ccell.2022.01.002

982 30. Astarita JL, Cremasco V, Fu J, et al. The CLEC-2–podoplanin axis controls fibroblastic reticular cell
983 contractility and lymph node microarchitecture. *Nat Immunol*. 2015;16(1):75-84.
984 doi:10.1038/ni.3035

985 31. Aoufouchi S, Faili A, Zober C, et al. Proteasomal degradation restricts the nuclear lifespan of AID. *J*
986 *Exp Med*. 2008;205(6):1357-1368. doi:10.1084/jem.20070950

987 32. ZAN H, CASALI P. Regulation of Aicda expression and AID activity. *Autoimmunity*. 2013;46(2):83-101.
988 doi:10.3109/08916934.2012.749244

989 33. Yoshitomi H, Ueno H. Shared and distinct roles of T peripheral helper and T follicular helper cells in
990 human diseases. *Cell Mol Immunol*. 2021;18(3):523-527. doi:10.1038/s41423-020-00529-z

991 34. Rao DA, Gurish MF, Marshall JL, et al. Pathologically expanded peripheral T helper cell subset drives
992 B cells in rheumatoid arthritis. *Nature*. 2017;542(7639):110-114. doi:10.1038/nature20810

993 35. Bocharnikov AV, Keegan J, Wacleche VS, et al. PD-1^{hi}CXCR5^{-} T peripheral helper cells promote B cell
994 responses in lupus via MAF and IL-21. *JCI Insight*. 2019;4(20). doi:10.1172/jci.insight.130062

995 36. Kim JR, Lim HW, Kang SG, Hillsamer P, Kim CH. Human CD57+ germinal center-T cells are the major
996 helpers for GC-B cells and induce class switch recombination. *BMC Immunol*. 2005;6:3.
997 doi:10.1186/1471-2172-6-3

998 37. Marinova E, Han S, Zheng B. Germinal Center Helper T Cells Are Dual Functional Regulatory Cells
999 with Suppressive Activity to Conventional CD4+ T Cells. *J Immunol*. 2007;178(8):5010-5017.
1000 doi:10.4049/jimmunol.178.8.5010

1001 38. Palmer BE, Blyveis N, Fontenot AP, Wilson CC. Functional and Phenotypic Characterization of
1002 CD57+CD4+ T Cells and Their Association with HIV-1-Induced T Cell Dysfunction1. *J Immunol*.
1003 2005;175(12):8415-8423. doi:10.4049/jimmunol.175.12.8415

1004 39. Hong W, Yang B, He Q, Wang J, Weng Q. New Insights of CCR7 Signaling in Dendritic Cell Migration
1005 and Inflammatory Diseases. *Front Pharmacol*. 2022;13. Accessed January 30, 2023.
1006 https://www.frontiersin.org/articles/10.3389/fphar.2022.841687

1007 40. Horiuchi S, Wu H, Liu WC, et al. Tox2 is required for the maintenance of GC TFH cells and the
1008 generation of memory TFH cells. *Sci Adv*. 2021;7(41):eabj1249. doi:10.1126/sciadv.abj1249

1009 41. van der Leun AM, Thommen DS, Schumacher TN. CD8+ T cell states in human cancer: insights from
1010 single-cell analysis. *Nat Rev Cancer*. 2020;20(4):218-232. doi:10.1038/s41568-019-0235-4

1011 42. Caushi JX, Zhang J, Ji Z, et al. Transcriptional programs of neoantigen-specific TIL in anti-PD-1-
1012 treated lung cancers. *Nature*. 2021;596(7870):126-132. doi:10.1038/s41586-021-03752-4

1013 43. Liu B, Zhang Y, Wang D, Hu X, Zhang Z. Single-cell meta-analyses reveal responses of tumor-reactive
1014 CXCL13+ T cells to immune-checkpoint blockade. *Nat Cancer*. 2022;3(9):1123-1136.
1015 doi:10.1038/s43018-022-00433-7

1016 44. Lucca LE, Axisa PP, Lu B, et al. Circulating clonally expanded T cells reflect functions of tumor-
1017 infiltrating T cells. *J Exp Med*. 2021;218(4):e20200921. doi:10.1084/jem.20200921

1018 45. Posch F, Silina K, Leibl S, et al. Maturation of tertiary lymphoid structures and recurrence of stage II
1019 and III colorectal cancer. *Oncoimmunology*. 2017;7(2):e1378844.
1020 doi:10.1080/2162402X.2017.1378844

1021 46. Siliņa K, Soltermann A, Attar FM, et al. Germinal Centers Determine the Prognostic Relevance of
1022 Tertiary Lymphoid Structures and Are Impaired by Corticosteroids in Lung Squamous Cell
1023 Carcinoma. *Cancer Res*. 2018;78(5):1308-1320. doi:10.1158/0008-5472.CAN-17-1987

1024 47. Arulraj T, Binder SC, Robert PA, Meyer-Hermann M. Germinal Centre Shutdown. *Front Immunol*.
1025 2021;12. Accessed March 4, 2023.
1026 https://www.frontiersin.org/articles/10.3389/fimmu.2021.705240

1027 48. Gavil NV, Scott MC, Weyu E, et al. Chronic antigen in solid tumors drives a distinct program of T cell
1028 residence. *Sci Immunol*. 2023;8(84):eadd5976. doi:10.1126/sciimmunol.add5976

1029 49. Garaud S, Dieu-Nosjean MC, Willard-Gallo K. T follicular helper and B cell crosstalk in tertiary
1030 lymphoid structures and cancer immunotherapy. *Nat Commun*. 2022;13(1):2259.
1031 doi:10.1038/s41467-022-29753-z

1032 50. Gutiérrez-Melo N, Baumjohann D. T follicular helper cells in cancer. *Trends Cancer*. 2023;9(4):309-
1033 325. doi:10.1016/j.trecan.2022.12.007

1034 51. Gu-Trantien C, Loi S, Garaud S, et al. $CD4^+$ follicular helper T cell infiltration predicts breast cancer
1035 survival. *J Clin Invest*. 2013;123(7):2873-2892. doi:10.1172/JCI67428

1036 52. Gu-Trantien C, Migliori E, Buisseret L, et al. CXCL13-producing TFH cells link immune suppression
1037 and adaptive memory in human breast cancer. *JCI Insight*. 2017;2(11):e91487, 91487.
1038 doi:10.1172/jci.insight.91487

1039 53. Argyriou A, Wadsworth MH, Lendvai A, et al. Single cell sequencing identifies clonally expanded
1040 synovial CD4+ TPH cells expressing GPR56 in rheumatoid arthritis. *Nat Commun*. 2022;13(1):4046.
1041 doi:10.1038/s41467-022-31519-6

1042 54. Chung Y, Tanaka S, Chu F, et al. Follicular regulatory T cells expressing Foxp3 and Bcl-6 suppress
1043 germinal center reactions. *Nat Med*. 2011;17(8):983-988. doi:10.1038/nm.2426

1044 55. Linterman MA, Pierson W, Lee SK, et al. Foxp3+ follicular regulatory T cells control the germinal
1045 center response. *Nat Med*. 2011;17(8):975-982. doi:10.1038/nm.2425

1046 56. Sage PT, Francisco LM, Carman CV, Sharpe AH. The receptor PD-1 controls follicular regulatory T
1047 cells in the lymph nodes and blood. *Nat Immunol*. 2013;14(2):152-161. doi:10.1038/ni.2496

1048 57. Sage PT, Paterson AM, Lovitch SB, Sharpe AH. The coinhibitory receptor CTLA-4 controls B cell
1049 responses by modulating T follicular helper, T follicular regulatory, and T regulatory cells. *Immunity*.
1050 2014;41(6):1026-1039. doi:10.1016/j.immuni.2014.12.005

1051 58. Wing JB, Ise W, Kurosaki T, Sakaguchi S. Regulatory T cells control antigen-specific expansion of Tfh
1052 cell number and humoral immune responses via the coreceptor CTLA-4. *Immunity*. 2014;41(6):1013-
1053 1025. doi:10.1016/j.immuni.2014.12.006

1054 59. Raftery AE. Bayesian Model Selection in Social Research. *Sociol Methodol*. 1995;25:111-163.
1055 doi:10.2307/271063

1056 60. Abbott CW, Boyle SM, Pyke RM, et al. Prediction of Immunotherapy Response in Melanoma through
1057 Combined Modeling of Neoantigen Burden and Immune-Related Resistance Mechanisms. *Clin*
1058 *Cancer Res Off J Am Assoc Cancer Res*. 2021;27(15):4265-4276. doi:10.1158/1078-0432.CCR-20-
1059 4314

1060 61. Love MI, Huber W, Anders S. Moderated estimation of fold change and dispersion for RNA-seq data
1061 with DESeq2. *Genome Biol*. 2014;15(12):550. doi:10.1186/s13059-014-0550-8

1062 62. Gene set enrichment analysis: A knowledge-based approach for interpreting genome-wide
1063 expression profiles | PNAS. Accessed June 12, 2023.
1064 https://www.pnas.org/doi/10.1073/pnas.0506580102

1065 63. Korotkevich G, Sukhov V, Budin N, Shpak B, Artyomov MN, Sergushichev A. Fast gene set
1066 enrichment analysis. Published online February 1, 2021:060012. doi:10.1101/060012

1067 64. Levy E, Milani P, Bartha G, et al. 67 B-cell receptor heavy chain repertoire profiling using an
1068 augmented transcriptome. *J Immunother Cancer*. 2020;8(Suppl 3). doi:10.1136/jitc-2020-
1069 SITC2020.0067

1070 65. Bolotin DA, Poslavsky S, Mitrophanov I, et al. MiXCR: software for comprehensive adaptive
1071 immunity profiling. *Nat Methods*. 2015;12(5):380-381. doi:10.1038/nmeth.3364

1072 66. ImmunoMind Team. immunarch: an R package for painless bioinformatics analysis of T-cell and B-
1073 cell immune repertoires. Zenodo https://doi.org/10.5281/zenodo.3367200 (2019).

1074 67. Montagne JM, Zheng XA, Pinal-Fernandez I, et al. Ultra-efficient sequencing of T Cell receptor
1075 repertoires reveals shared responses in muscle from patients with Myositis. *EBioMedicine*.
1076 2020;59:102972. doi:10.1016/j.ebiom.2020.102972

1077 68. Zabransky DJ, Danilova L, Leatherman JM, et al. Profiling of syngeneic mouse HCC tumor models as a
1078 framework to understand anti–PD-1 sensitive tumor microenvironments. *Hepatology*.
1079 2023;77(5):1566. doi:10.1002/hep.32707

1080 69. Zanotelli VRT, Bodenmiller B. ImcSegmentationPipeline: A pixelclassification based multiplexed
1081 image segmentation pipeline. Published online September 14, 2017. doi:10.5281/zenodo.3841961

1082 70. Carpenter AE, Jones TR, Lamprecht MR, et al. CellProfiler: image analysis software for identifying
1083 and quantifying cell phenotypes. *Genome Biol*. 2006;7(10):R100. doi:10.1186/gb-2006-7-10-r100

1084 71. Berg S, Kutra D, Kroeger T, et al. ilastik: interactive machine learning for (bio)image analysis. *Nat*
1085 *Methods*. 2019;16(12):1226-1232. doi:10.1038/s41592-019-0582-9

1086 72. Schapiro D, Jackson HW, Raghuraman S, et al. histoCAT: analysis of cell phenotypes and interactions
1087 in multiplex image cytometry data. *Nat Methods*. 2017;14(9):873-876. doi:10.1038/nmeth.4391

1088 73. FlowSOM: Using self-organizing maps for visualization and interpretation of cytometry data - Van
1089 Gassen - 2015 - Cytometry Part A - Wiley Online Library. Accessed June 14, 2023.
1090 https://onlinelibrary.wiley.com/doi/full/10.1002/cyto.a.22625

1091 74. Schneider CA, Rasband WS, Eliceiri KW. NIH Image to ImageJ: 25 years of image analysis. *Nat*
1092 *Methods*. 2012;9(7):671-675. doi:10.1038/nmeth.2089

1093 75. Epskamp S, Cramer AOJ, Waldorp LJ, Schmittmann VD, Borsboom D. qgraph: Network Visualizations
1094 of Relationships in Psychometric Data. *J Stat Softw*. 2012;48:1-18. doi:10.18637/jss.v048.i04

1095 76. Robins HS, Campregher PV, Srivastava SK, et al. Comprehensive assessment of T-cell receptor beta-
1096 chain diversity in alphabeta T cells. *Blood*. 2009;114(19):4099-4107. doi:10.1182/blood-2009-04-
1097 217604

1098 77. Carlson CS, Emerson RO, Sherwood AM, et al. Using synthetic templates to design an unbiased
1099 multiplex PCR assay. *Nat Commun*. 2013;4:2680. doi:10.1038/ncomms3680

1100 78. Gupta NT, Vander Heiden JA, Uduman M, Gadala-Maria D, Yaari G, Kleinstein SH. Change-O: a
1101 toolkit for analyzing large-scale B cell immunoglobulin repertoire sequencing data. *Bioinformatics*.
1102 2015;31(20):3356-3358. doi:10.1093/bioinformatics/btv359

1103 79. Venturi V, Kedzierska K, Tanaka MM, Turner SJ, Doherty PC, Davenport MP. Method for assessing
1104 the similarity between subsets of the T cell receptor repertoire. *J Immunol Methods*.
1105 2008;329(1):67-80. doi:10.1016/j.jim.2007.09.016

1106 80. Hafemeister C, Satija R. Normalization and variance stabilization of single-cell RNA-seq data using
1107 regularized negative binomial regression. *Genome Biol*. 2019;20(1):296. doi:10.1186/s13059-019-
1108 1874-1

1109 81. Ahlmann-Eltze C, Huber W. glmGamPoi: fitting Gamma-Poisson generalized linear models on single
1110 cell count data. *Bioinformatics*. 2020;36(24):5701-5702. doi:10.1093/bioinformatics/btaa1009

1111 82. Hao Y, Hao S, Andersen-Nissen E, et al. Integrated analysis of multimodal single-cell data. *Cell*.
1112 2021;184(13):3573-3587.e29. doi:10.1016/j.cell.2021.04.048

1113 83. Finak G, McDavid A, Yajima M, et al. MAST: a flexible statistical framework for assessing
1114 transcriptional changes and characterizing heterogeneity in single-cell RNA sequencing data.
1115 *Genome Biol*. 2015;16:278. doi:10.1186/s13059-015-0844-5

1116 84. Borcherding N, Bormann NL, Kraus G. scRepertoire: An R-based toolkit for single-cell immune
1117 receptor analysis. *F1000Research*. 2020;9:47. doi:10.12688/f1000research.22139.2

1118

1119 **Table 1 | Characteristics of the Patients, According to Treatment Status**

	Neoadjuvant (N=19)	Untreated (N=14)	Total (N=33)
Age at surgery — yr			
Mean (SD)	64±10	66±9.0	65±9.6
Median (range)	65 (41-79)	66 (49-84)	65 (41-84)
Sex — no. (%)			
Male	11 (58)	11 (79)	22 (67)
Female	8 (42)	3 (21)	11 (33)
Histologic grade — no. (%)			
Poorly differentiated	3 (16)	1 (7)	4 (12)
Moderately differentiated	13 (68)	8 (57)	21 (64)
Well differentiated	3 (16)	5 (36)	8 (24)
Etiology — no. (%)			
HBV	3 (16)	1 (7)	4 (12)
HCV	7 (37)	6 (43)	13 (39)
HBV/HCV	1 (5)	1 (7)	2 (6)
NASH	2 (11)	3 (21)	5 (15)
ETOH	1 (5)	1 (7)	2 (6)
Unknown	5 (26)	2 (14)	7 (21)
Neoadjuvant Treatment — no. (%)			
anti-PD1 + TKI	14 (74)	0 (0)	14 (42)
anti-PD1	3 (16)	0 (0)	3 (9)
anti-PD1 + anti-CTLA4	1 (5)	0 (0)	1 (3)
anti-PD1 + anti-CTLA4 + TKI	1 (5)	0 (0)	1 (3)
None	0 (0)	14 (100)	14 (42)

1120
1121
1122
1123
1124

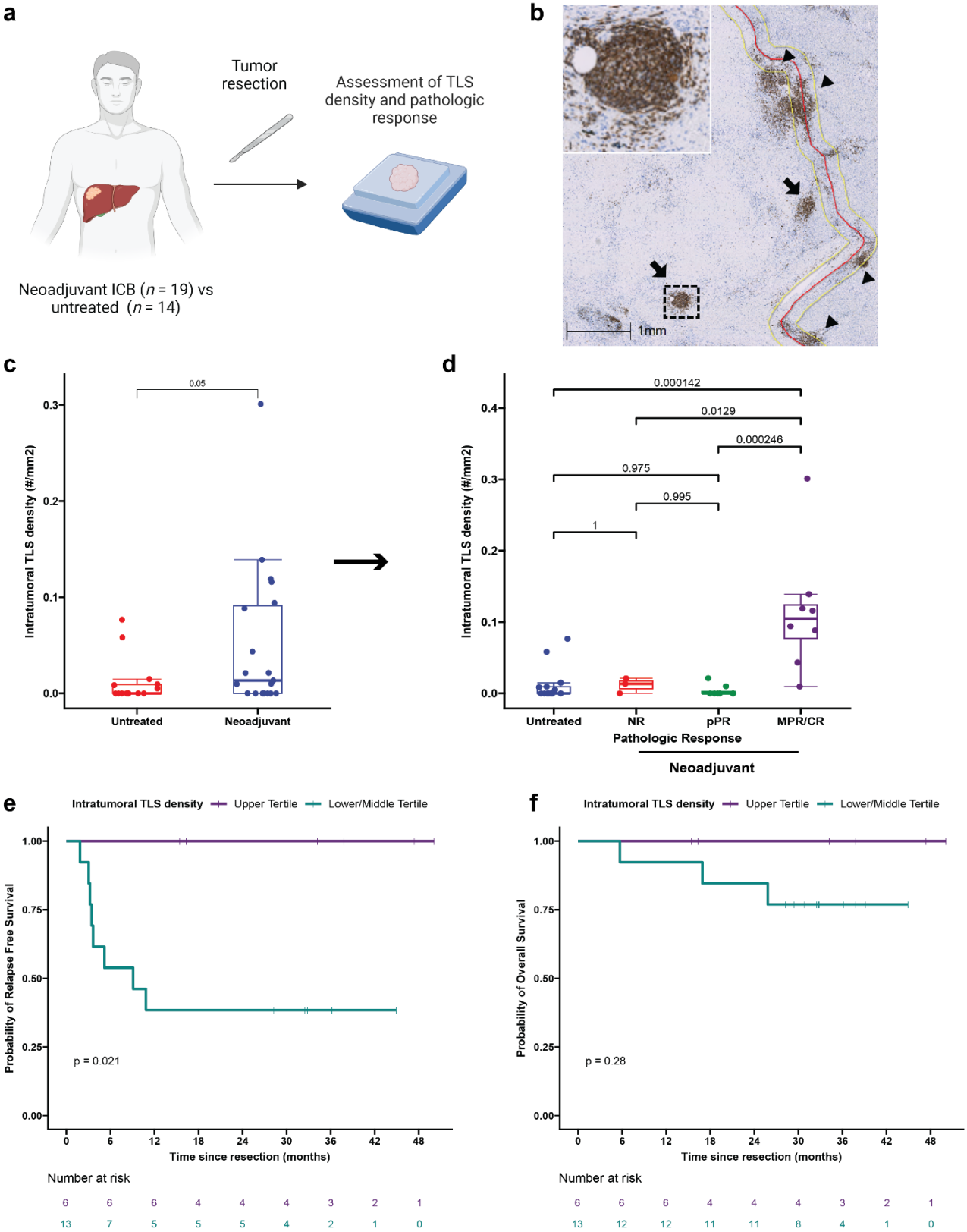
a
Tumor resection
Assessment of TLS density and pathologic response
Neoadjuvant ICB (n = 19) vs untreated (n = 14)
b
1mm
c
Intratumoral TLS density (#/mm2)
0.05
Untreated
Neoadjuvant
d
Intratumoral TLS density (#/mm2)
0.000142
0.0129
0.000246
0.975
0.995
1
Untreated
NR
pPR
MPR/CR
Pathologic Response
Neoadjuvant
e
Intratumoral TLS density
Upper Tertile
Lower/Middle Tertile
Probability of Relapse Free Survival
p = 0.021
Time since resection (months)
Number at risk
6 6 6 4 4 4 3 2 1
13 7 5 5 5 4 2 1 0
f
Intratumoral TLS density
Upper Tertile
Lower/Middle Tertile
Probability of Overall Survival
p = 0.28
Time since resection (months)
Number at risk
6 6 6 4 4 4 3 2 1
13 12 12 11 11 8 4 1 0

1125

Fig. 1 | Neoadjuvant ICB induces intratumoral TLS, which are associated with superior pathologic response and relapse free survival. a, Workflow for TLS density analysis. **b,** Representative images of formalin fixed paraffin embedded (FFPE) HCC tumors stained with anti-CD20 antibody. Annotations indicate boundary between tumor/tumor regression bed and adjacent normal parenchyma (red), extension of boundary by 200 µm (yellow), intratumoral TLS (arrow), and peritumoral TLS (arrow head). Inset shows representative TLS at high magnification. Scale bar, 1mm. **c,** Box-and-whisker plots showing intratumoral TLS density in patients with locally advanced HCC treated with neoadjuvant ICB (n = 19) and untreated controls (n = 14). **d,** Boxplot-and-whisker plots showing intratumoral TLS density in untreated (n = 14) and neoadjuvant treated tumors, divided according to pathologic response (n = 19). For each box-and-whisker plot, the horizontal bar indicates the median, the upper and lower limits of the boxes the interquartile range, and the ends of the whiskers 1.5 times the interquartile range. **e-f,** Kaplan-Meier curves showing relapse free survival (**e**) and overall survival (**f**) for patients with HCC in the highest tertile (purple) compared to the middle and lowest tertiles (green) of intratumoral TLS density after neoadjuvant ICB. Statistical significance was determined by two-tailed t-test (**c**), one-way ANOVA followed by Tukey's honest significant difference (HSD) test (**d**), and log-rank test (**e** and **f**).

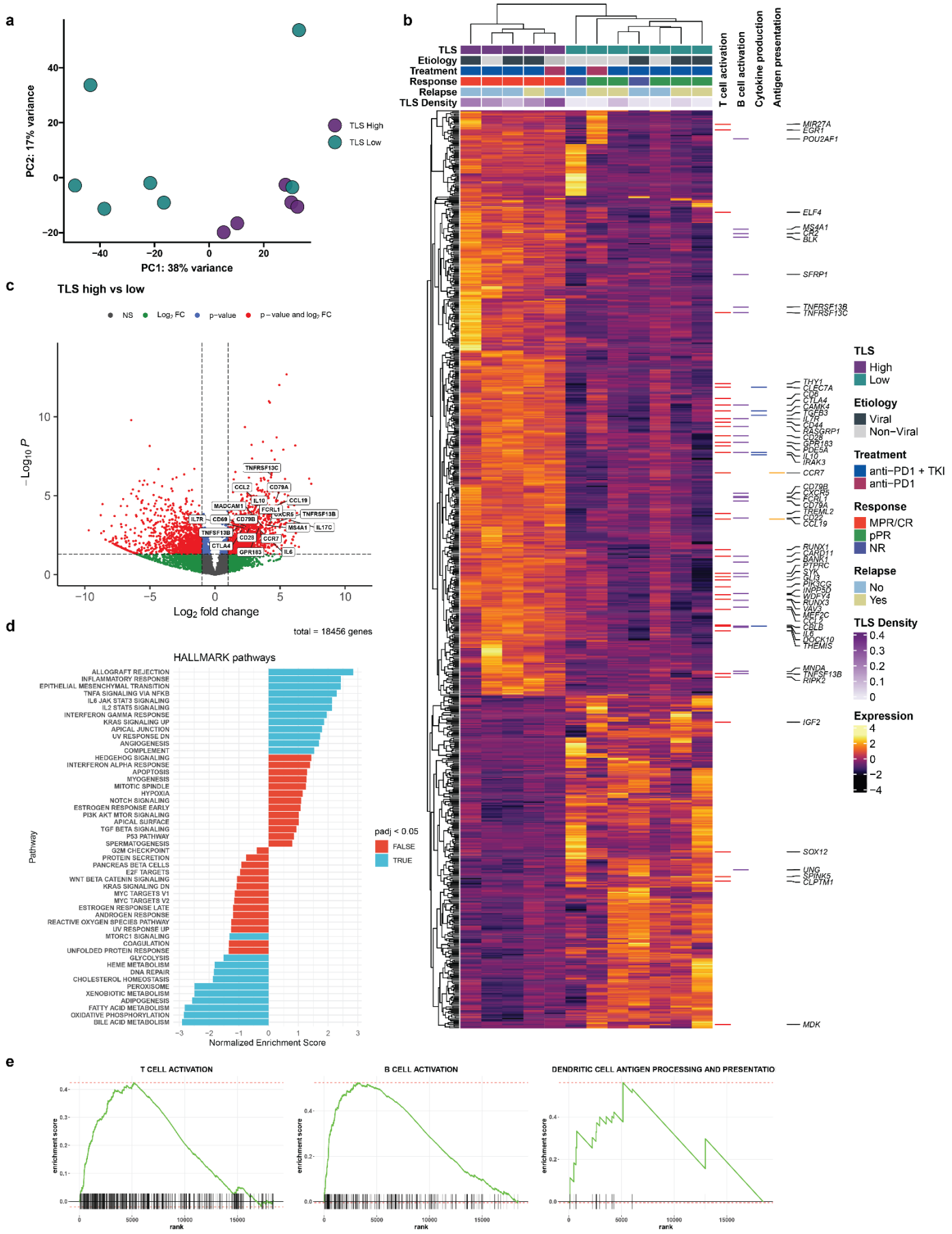
a
PC2: 17% variance
PC1: 38% variance
TLS High
TLS Low
b
TLS
Etiology
Treatment
Response
Relapse
TLS Density
T cell activation
B cell activation
Cytokine production
Antigen presentation
MIR27A
EGR1
POU2AF1
ELF4
MS4A1
CR2
BLK
SFRP1
TNFRSF13B
TNFRSF13C
THY1
CLEC7A
CD5
CTLA4
CAMK4
TGFB3
IL7R
CD44
RASGRP1
CD28
GPR183
PDE5A
IL10
IRAK3
CCR7
CD79B
CXCR5
FCRL1
CD79A
TREML2
CD22
CCL19
RUNX1
CARD11
BANK1
PTPRC
SYK
CLL3
PIK3CG
INPP5D
WDFY4
RUNX3
VAV3
MEF2C
CCL5
CBLB
IL6
DOCK10
THEMIS
MNDA
TNFSF13B
RIPK2
IGF2
SOX12
UNG
SPINK5
CLPTM1
MDK
TLS
High
Low
Etiology
Viral
Non−Viral
Treatment
anti−PD1 + TKI
anti−PD1
Response
MPR/CR
pPR
NR
Relapse
No
Yes
TLS Density
0.4
0.3
0.2
0.1
0
Expression
4
2
0
−2
−4
c
TLS high vs low
NS
Log2 FC
p−value
p−value and log2 FC
−Log10 P
Log2 fold change
TNFRSF13C
CCL2
CD79A
IL10
CCL19
MADCAM1
FCRL1
CXCR5
TNFRSF13B
IL7R
CD69
CD79B
MS4A1
IL17C
TNFSF13B
CD28
CCR7
CTLA4
GPR183
IL6
d
total = 18456 genes
HALLMARK pathways
ALLOGRAFT REJECTION
INFLAMMATORY RESPONSE
EPITHELIAL MESENCHYMAL TRANSITION
TNFA SIGNALING VIA NFKB
IL6 JAK STAT3 SIGNALING
IL2 STAT5 SIGNALING
INTERFERON GAMMA RESPONSE
KRAS SIGNALING UP
APICAL JUNCTION
UV RESPONSE DN
ANGIOGENESIS
COMPLEMENT
HEDGEHOG SIGNALING
INTERFERON ALPHA RESPONSE
APOPTOSIS
MYOGENESIS
MITOTIC SPINDLE
HYPOXIA
NOTCH SIGNALING
ESTROGEN RESPONSE EARLY
PI3K AKT MTOR SIGNALING
APICAL SURFACE
TGF BETA SIGNALING
P53 PATHWAY
SPERMATOGENESIS
G2M CHECKPOINT
PROTEIN SECRETION
PANCREAS BETA CELLS
E2F TARGETS
WNT BETA CATENIN SIGNALING
KRAS SIGNALING DN
MYC TARGETS V1
MYC TARGETS V2
ESTROGEN RESPONSE LATE
ANDROGEN RESPONSE
REACTIVE OXYGEN SPECIES PATHWAY
UV RESPONSE UP
MTORC1 SIGNALING
COAGULATION
UNFOLDED PROTEIN RESPONSE
GLYCOLYSIS
HEME METABOLISM
DNA REPAIR
CHOLESTEROL HOMEOSTASIS
PEROXISOME
XENOBIOTIC METABOLISM
ADIPOGENESIS
FATTY ACID METABOLISM
OXIDATIVE PHOSPHORYLATION
BILE ACID METABOLISM
Pathway
padj < 0.05
FALSE
TRUE
Normalized Enrichment Score
e
T CELL ACTIVATION
B CELL ACTIVATION
DENDRITIC CELL ANTIGEN PROCESSING AND PRESENTATIO
enrichment score
rank

1189 **Fig. 2 | High TLS density is associated with increased T and B cell activation in HCC treated**
1190 **with neoadjuvant ICB. a,** Principle component analysis of bulk RNA-sequencing of resected
1191 HCC tumors treated with neoadjuvant ICB (n = 12), divided according to TLS density relative to
1192 mean density of the neoadjuvant treatment group. **b,** Heatmap showing differentially expressed
1193 genes (DEG) with a log2 fold change > 1 and P < 0.05 between tumors with high (n = 5) and low
1194 (n = 7) TLS density. Annotation rows indicate TLS group, HCC etiology, treatment, response,
1195 relapse, and TLS density. Annotation columns at right identify DEG belonging to Gene Oncology
1196 Biological Pathways gene sets for T cell activation, B cell activation, Cytokine production, and
1197 Dendritic Cell Antigen Processing and Presentation. **c,** Volcano plot showing differentially
1198 expressed genes between tumors with high and low TLS density. Vertical dotted lines represents
1199 log2 fold change greater than or less than 1. Horizontal dotted line indicates adjusted P value of
1200 0.05. 4 outlier genes are excluded from the plot for the purposes of visualization. **d,** Gene set
1201 enrichment analysis showing differentially enriched gene sets from the HALLMARK database
1202 between tumors with high and low TLS density. **e,** Barcode plots showing enrichment scores for
1203 the Gene Ontology Biological Pathways gene sets for T cell activation, B cell activation, and
1204 Dendritic Cell Antigen Processing and Presentation.

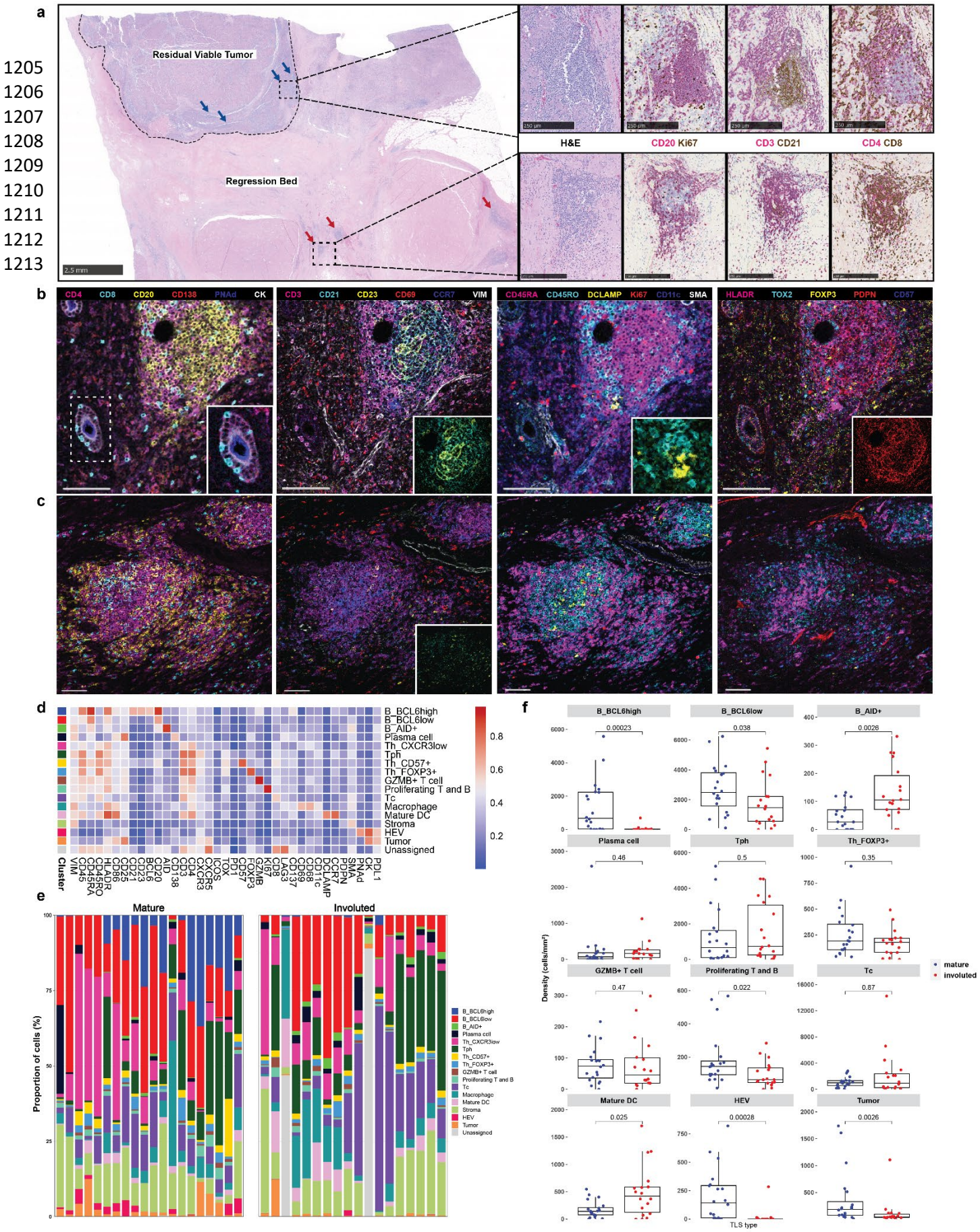
a
Residual Viable Tumor
Regression Bed
2.5 mm
H&E
CD20 Ki67
CD3 CD21
CD4 CD8
b
CD4 CD8 CD20 CD138 PNAd CK
CD3 CD21 CD23 CD69 CCR7 VIM
CD45RA CD45RO DCLAMP Ki67 CD11c SMA
HLADR TOX2 FOXP3 PDPN CD57
c
d
B_BCL6high
B_BCL6low
B_AID+
Plasma cell
Th_CXCR3low
Tph
Th_CD57+
Th_FOXP3+
GZMB+ T cell
Proliferating T and B
Tc
Macrophage
Mature DC
Stroma
HEV
Tumor
Unassigned
Cluster
VIM CD45 CD45RA CD45RO HLADR CD68 CD21 CD23 BCL6 CD20 AID CD138 CD3 CD4 CXCR3 CXCR5 ICOS TOX PD1 CD57 FOXP3 GZMB Ki67 LAG3 CD137 CD69 CD68 CD11c DCLAMP CCR7 SMA PNAd CK PDL1
e
Mature
Involuted
Proportion of cells (%)
f
B_BCL6high
B_BCL6low
B_AID+
Plasma cell
Tph
Th_FOXP3+
GZMB+ T cell
Proliferating T and B
Tc
Mature DC
HEV
Tumor
Density (cells/mm²)
mature
involuted
TLS type

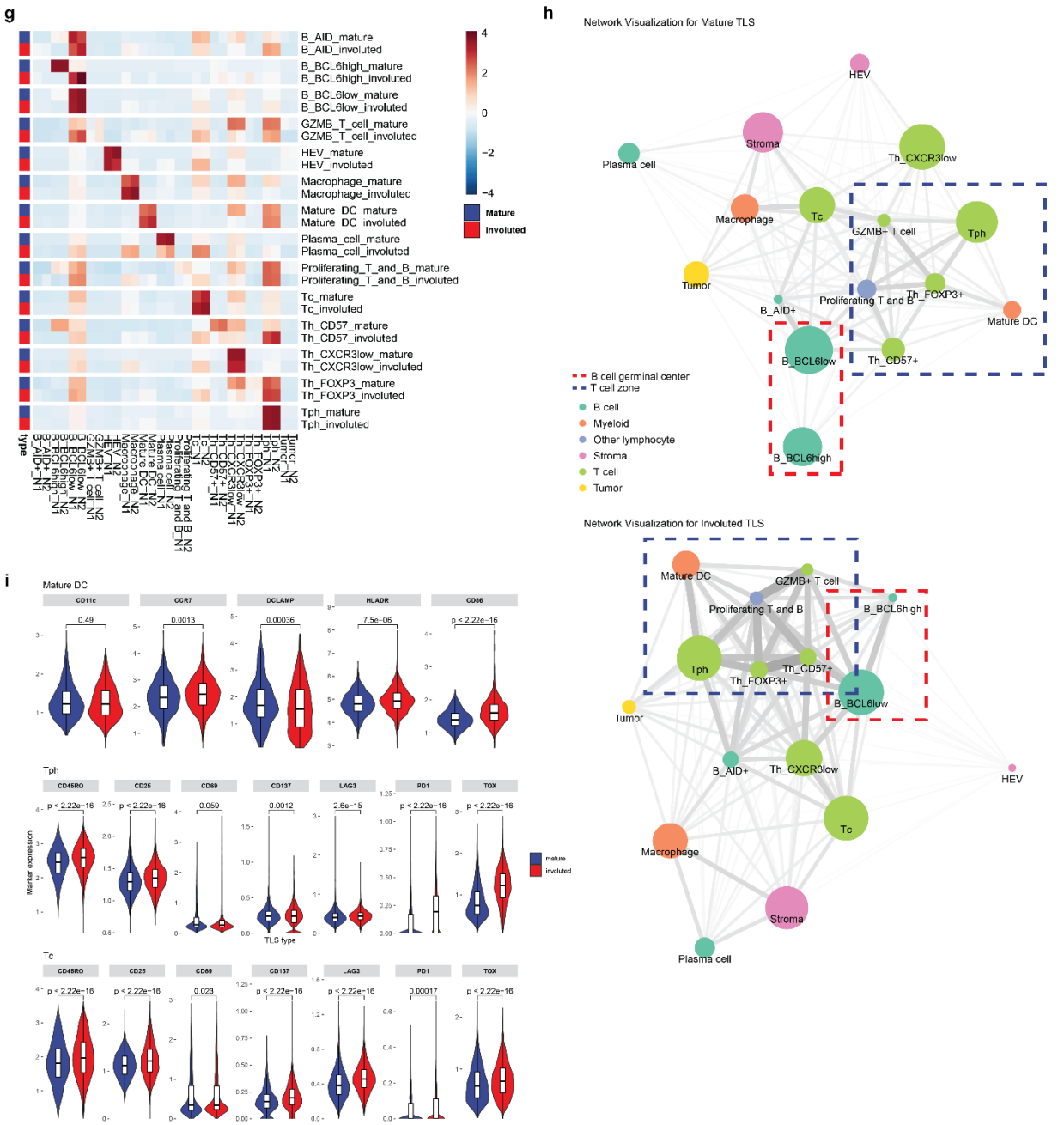

Fig. 3 | Identification of divergent TLS morphologies and cellular spatial relationships in viable tumor and tumor regression bed. a, Representative formalin-fixed, paraffin embedded (FFPE) neoadjuvant ICB-treated tumor stained with hematoxylin and eosin (H&E) showing divergent TLS morphologies ("mature" and "involuted") in viable residual viable tumor and regression bed. Dotted line shows boundary between residual viable tumor and regression bed. Blue arrows indicate mature TLS and red arrows indicate involuted TLS. Scale bar, 2.5mm. Higher magnification images of representative mature and involuted TLSare shown on right with serial sections stained with dual immunohistochemistry staining for CD20 (magenta) and Ki67 (brown), CD3 (magenta) and CD21 (brown), and CD4 (magenta) and CD8 (brown). Scale bars, 250 µm. **b-c,** Representative images of mature (**b**) and involuted (**c**) TLS obtained by imaging mass

cytometry. Insets show higher magnification images of $CD8^+$ T cells trafficking through high endothelial venules (**b, far left**), an extensive $CD21^+CD23^+$ follicular dendritic cell network in the mature morphology (**b**, **middle left**) compared to scant $CD21^+$ and $CD23^+$ in the involuted morphology (**c**, **middle left**), close interactions between T cells and $DCLAMP^+$ mature dendritic cells in the T cell zone adjacent to the germinal center (**b, middle right**), and high podoplanin expression in the germinal center of the mature TLS (**b**, **far right**). Scale bars, 100 μm. **d,** Heatmap showing average IMC marker expression in annotated cell clusters identified from 90,344 single cells from 38 TLS (*n* = 20 mature, *n* = 18 involuted). **e,** Composition of mature and involuted TLS regions by cell type as a percentage of total cells per TLS. **f**, Box-and-whisker plots showing cell cluster density in mature versus involuted TLS. For each box-and-whisker plot, the horizontal bar indicates the median, the upper and lower limits of the boxes the interquartile range, and the ends of the whiskers 1.5 times the interquartile range. **g,** Nearest neighbor analysis with rows indicating individual clusters in mature and involuted TLS and columns corresopnding to first and second most common neighbors. **h,** Network analysis for cell clusters in mature and involuted TLS. Node size corresponds to the proportion of total cells for each TLS type occupied by each cluster. Edge length represents the shortest distance between cell clusters and thickness corresponds to the number of measurements for each TLS type. **i**, Box and violin plots showing expression of mature dendritic cell markers (CD11c, CCR7, DCLAMP, HLADR, and CD86) in the mature DC cluster and markers of T cell activation and exhaustion (CD45RO, CD25, CD69, CD137, LAG3, PD1, and TOX) in the T peripheral helper (Tph) and cytotoxic T cell (Tc) clusters, by TLS morphology. Statistical significance was determined by pairwise two sample Wilcoxon test (**f** and **g**).

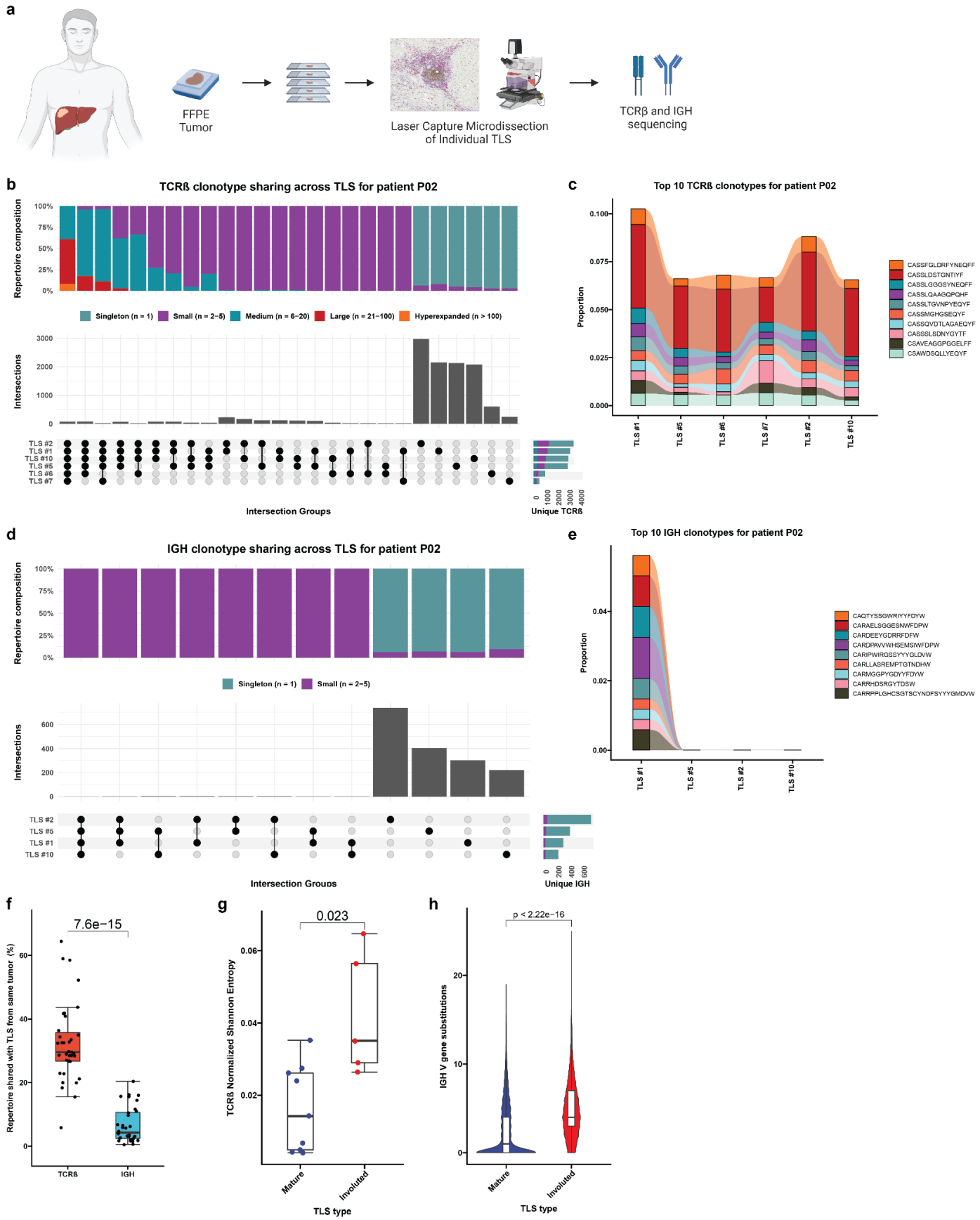
a
FFPE
Tumor
Laser Capture Microdissection
of Individual TLS
TCRβ and IGH
sequencing
b
TCRß clonotype sharing across TLS for patient P02
Repertoire composition
Singleton (n = 1)
Small (n = 2–5)
Medium (n = 6–20)
Large (n = 21–100)
Hyperexpanded (n > 100)
Intersections
Intersection Groups
Unique TCRß
c
Top 10 TCRß clonotypes for patient P02
Proportion
CASSFGLDRFYNEQFF
CASSLDSTGNTIYF
CASSLGGGSYNEQFF
CASSLQAAGQPQHF
CASSLTGVNPYEQYF
CASSMGHGSEQYF
CASSQVDTLAGAEQYF
CASSSLSDNYGYTF
CSAVEAGGPGGELFF
CSAWDSQLLYEQYF
d
IGH clonotype sharing across TLS for patient P02
Repertoire composition
Singleton (n = 1)
Small (n = 2–5)
Intersections
Intersection Groups
Unique IGH
e
Top 10 IGH clonotypes for patient P02
Proportion
CAQTYSSGWRIYYFDYW
CARAELSGGESNWFDPW
CARDEEYGDRRFDFW
CARDPAVVWHSEMSIWFDPW
CARIPWIRGSSYYYGLDVW
CARLLASREMPTGTNDHW
CARMGGPYGDYYFDYW
CARRHDSRGYTDSW
CARRPPLGHCSGTSCYNDFSYYYGMDVW
f
7.6e−15
Repertoire shared with TLS from same tumor (%)
TCRß
IGH
g
0.023
TCRß Normalized Shannon Entropy
Mature
Involuted
TLS type
h
p < 2.22e−16
IGH V gene substitutions
Mature
Involuted
TLS type

1323 **Fig. 4 | Expanded T cell clonotypes are shared across TLS within a tumor, while B cell**
1324 **repertoires of individual TLS are highly distinct. a,** Workflow for T and B cell repertoire profiling
1325 of microdissected TLS (*n* = 30 mature and 5 involuted) from 7 patients. **b** and **d,** Upset plots
1326 showing overlap in unique TCRβ (**b**) and IGH (**d)** clonotypes across microdissected TLS from the
1327 same patient (P02). Barplots in gray and annotation row indicate distinct groups of clonotypes
1328 shared between different TLS. Top stacked barplots indicate composition of groups according to
1329 clonal expansion. Bottom right stacked barplots indicate total number of unique TCRβ or IGH
1330 clonotypes identified at each TLS according to degree of clonal expansion. **c** and **e,** Alluvial plots
1331 tracking the top 10 TCRβ (**c**) or IGH (**e**) clonotypes from TLS # 1 of patient P02 across all TLS
1332 microdissected from the patient's tumor. **f,** Box-and-whisker plot comparing the percentage of the
1333 TCRβ or IGH repertoire of each TLS that is shared with other TLS from the same tumor. **g,** Box-
1334 and-whisker plots comparing TCRβ clonality (as determined by Normalized Shannon Entropy) in
1335 mature and involuted TLS microdissected from patients P12, OT1, and OT6. Each point
1336 represents the TCRβ of an individual TLS. **h,** Violin plots comparing number of somatic
1337 hypermutations in IGH of mature and involuted TLS microdissected from patients P12, OT1, and
1338 OT6. Individual data points (not shown) represent individual IGH sequences. Statistical
1339 significance was determined by two-tailed t test (**f-h**).
1340

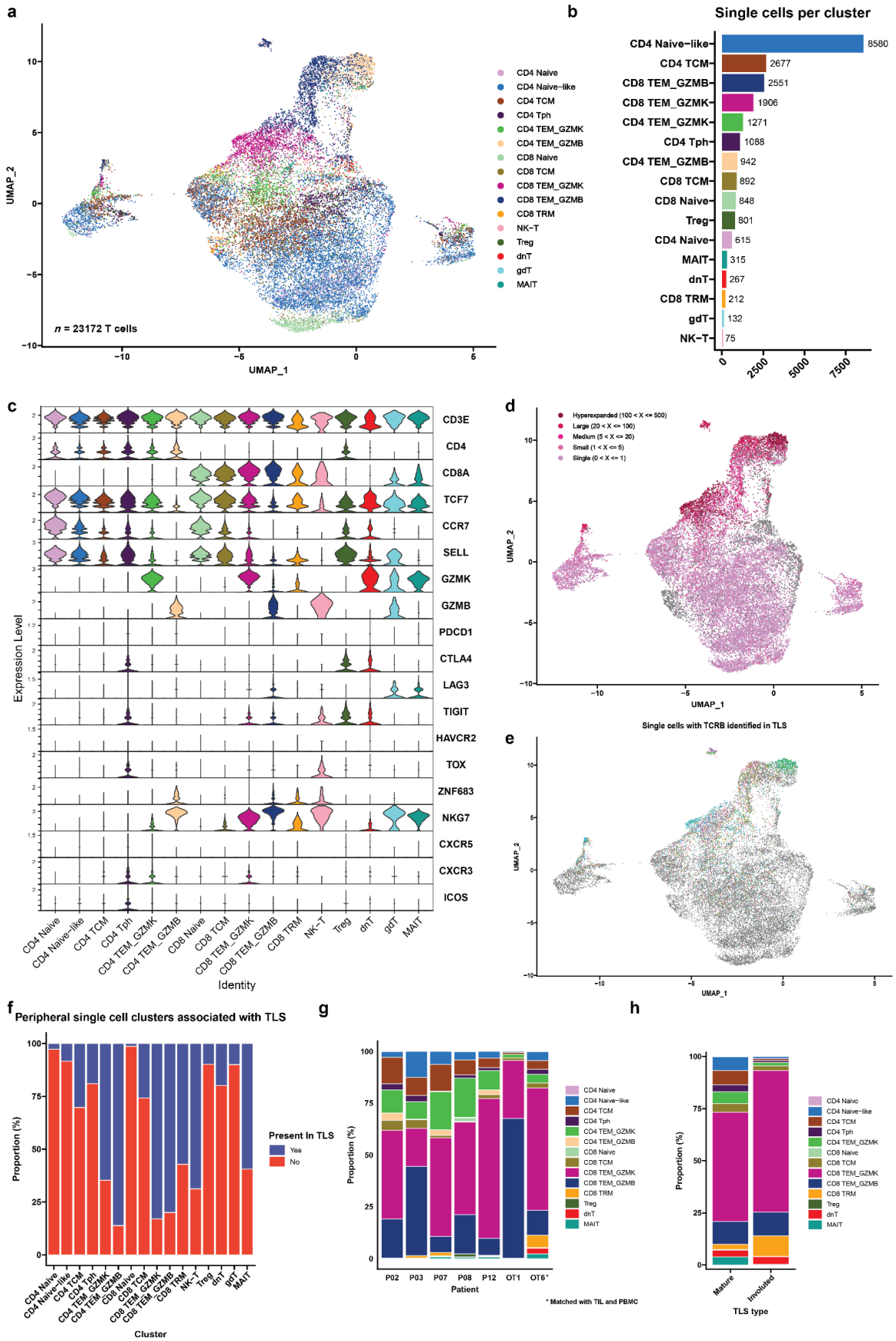
a
UMAP_2
UMAP_1
n = 23172 T cells
CD4 Naive
CD4 Naive−like
CD4 TCM
CD4 Tph
CD4 TEM_GZMK
CD4 TEM_GZMB
CD8 Naive
CD8 TCM
CD8 TEM_GZMK
CD8 TEM_GZMB
CD8 TRM
NK−T
Treg
dnT
gdT
MAIT
b
Single cells per cluster
CD4 Naive−like 8580
CD4 TCM 2677
CD8 TEM_GZMB 2551
CD8 TEM_GZMK 1906
CD4 TEM_GZMK 1271
CD4 Tph 1088
CD4 TEM_GZMB 942
CD8 TCM 892
CD8 Naive 848
Treg 801
CD4 Naive 615
MAIT 315
dnT 267
CD8 TRM 212
gdT 132
NK−T 75
c
Expression Level
CD3E
CD4
CD8A
TCF7
CCR7
SELL
GZMK
GZMB
PDCD1
CTLA4
LAG3
TIGIT
HAVCR2
TOX
ZNF683
NKG7
CXCR5
CXCR3
ICOS
Identity
d
Hyperexpanded (100 < X <= 500)
Large (20 < X <= 100)
Medium (5 < X <= 20)
Small (1 < X <= 5)
Single (0 < X <= 1)
e
Single cells with TCRB identified in TLS
f
Peripheral single cell clusters associated with TLS
Proportion (%)
Present In TLS
Yes
No
Cluster
g
Patient
P02
P03
P07
P08
P12
OT1
OT6*
* Matched with TIL and PBMC
h
Mature
Involuted
TLS type

1346 **Fig. 5 | Cytotoxic granzyme K and granzyme B-expressing CD8 T cells are highly**
1347 **represented in TLS. a**, Uniform Manifold Approximation and Projection (UMAP) of 23,172 T cells
1348 identified by single cell RNA/TCR/BCR sequencing of $CD3^{+}CD19^{+}$ FACS-sorted peripheral blood
1349 from HCC patients treated with neoadjuvant ICB (*n* = 7). **b,** Barplot showing number of single cells
1350 per cluster. **c,** Violin plots showing expression of subset specific marker genes across clusters.
1351 **d-e,** UMAPs showing clonality of single cells with an associated T cell receptor sequence (**d**) and
1352 single cells with a TCRβ identified in microdissected TLS (**e**). **f,** Stacked barplot showing
1353 proportion of each single cell cluster identified in TLS. **g,** Inferred transcriptional phenotype of
1354 TCRβ clonotypes in microdissected TLS with a matching TCRβ in single cell sequencing of post-
1355 treatment peripheral blood (*n* = 7) or tumor infiltrating lymphocytes (*n* = 1). **h,** Inferred
1356 transcriptional phenotype of TCRβ clonotypes in mature and resolving TLS of patient OT6.

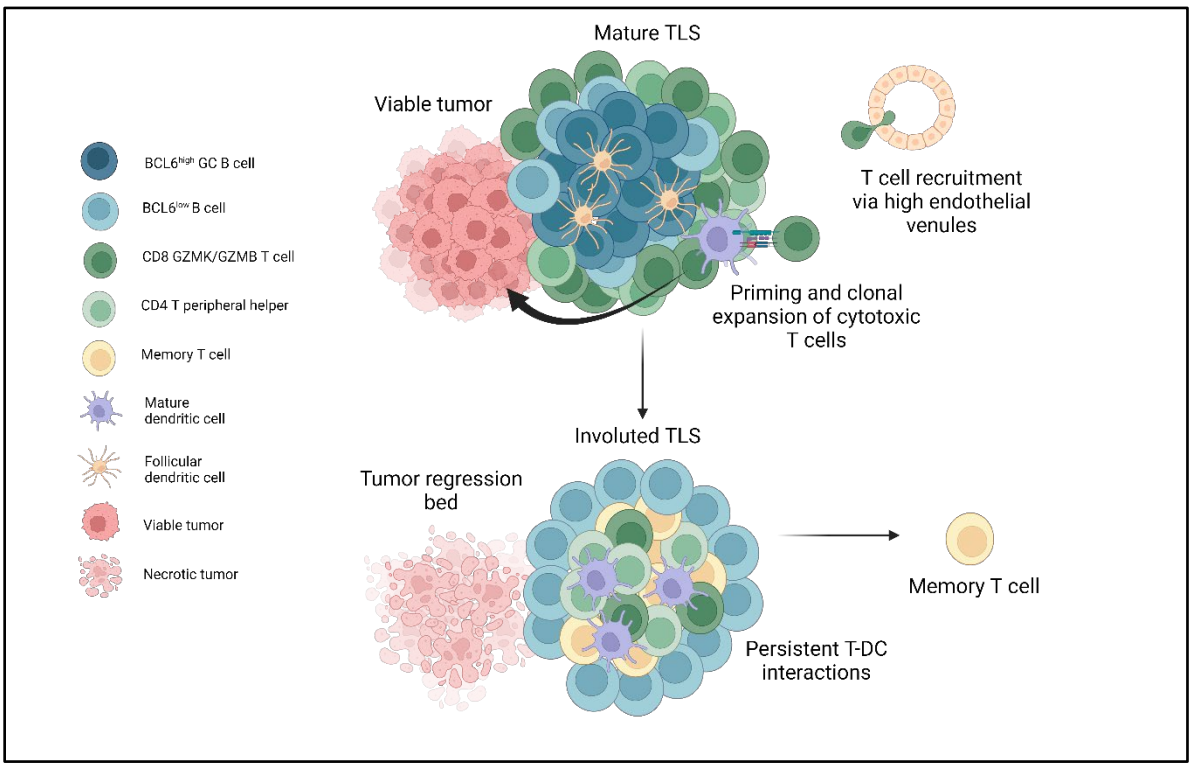

Fig. 6 | TLS structure and function in viable tumor and tumor regression bed in tumors treated with neoadjuvant checkpoint blockade. Mature TLS in viable tumor display a highly organized germinal center with close interactions between germinal center B cells and CD21$^+$ follicular dendritic cells, a T cell zone characterized by CD4$^+$ T peripheral helper cells in close proximity to mature dendritic cells, and cytotoxic CD8$^+$ T cells trafficking to the tumor via high endothelial venules. In areas of tumor regression, an involuted TLS morphology is found which displays dissolution of the B cell germinal center and persistence of Tph-DC interactions in the T cell zone, increased T cell memory marker expression, and clonal expansion of cytotoxic and tissue resident memory CD8$^+$ T cells.

1381 **Extended Data Table 1 | Clinical Characteristics of HCC cohort treated with neoadjuvant**
1382 **ICB.** Characteristics of treated patients. Each row represents a single patient and columns
1383 indicate age at surgery, sex, HCC etiology, histologic grade, treatment regimen, pathologic
1384 response, and whether the patient suffered relapsed or death.
1385

Patient	Age at surgery	Sex	Etiology	Histologic grade	Treatment	Response	Relapse	Death
P01	66	M	HCV	Moderately differentiated	α-PD1 + TKI	NR	No	No
P02	72	M	HCV	Moderately differentiated	α-PD1 + TKI	MPR	No	No
P03	76	F	Unknown	Moderately differentiated	α-PD1 + TKI	MPR	No	No
P07	64	F	HBV/HCV	Moderately differentiated	α-PD1 + TKI	pPR	Yes	Yes
P08	65	M	HCV	Moderately differentiated	α-PD1 + TKI	MPR	Yes	No
P09	47	M	HBV	Moderately differentiated	α-PD1 + TKI	CR	No	No
P10	41	F	HBV	Moderately differentiated	α-PD1 + TKI	pPR	Yes	Yes
P11	56	F	Unknown	Well differentiated	α-PD1 + TKI	pPR	No	No
P12	69	M	HCV	Moderately differentiated	α-PD1 + TKI	MPR	No	No
P13	74	F	Unknown	Poorly differentiated	α-PD1 + TKI	NR	No	No
P14	79	M	Unknown	Moderately differentiated	α-PD1 + TKI	pPR	Yes	No
P15	49	M	NASH	Moderately differentiated	α-PD1 + TKI	NR	Yes	Yes
OT1	68	M	ETOH	Poorly differentiated	α-PD1	MPR	No	No
OT2	71	F	Unknown	Well differentiated	α-PD1	pPR	No	No
OT3	63	M	HCV	Moderately differentiated	α-PD1 + TKI	pPR	Yes	No
OT4	69	F	HCV	Well differentiated	α-PD1 + TKI	pPR	Yes	No
OT5	62	M	NASH	Moderately differentiated	α-PD1	pPR	Yes	No
OT6	61	M	HCV	Moderately differentiated	α-PD1 + α-CTLA4 + TKI	MPR	No	No
OT7	56	F	HBV	Poorly differentiated	α-PD1 + α-CTLA4	CR	No	No

1386
1387

1388 **Extended Data Table 2 | Clinical characteristics of untreated HCC cohort.** Characteristics of
1389 untreated patients. Each row represents a single patient and columns indicate age at surgery,
1390 sex, HCC etiology, histologic grade, and treatment.
1391

Patient	Age at surgery	Sex	Etiology	Histologic grade	Treatment
C2	61	M	HCV	Moderately differentiated	none
C3	60	M	HBV/HCV	Well differentiated	none
C5	75	M	HCV/NASH	Well differentiated	none
C6	63	F	HCV	Moderately differentiated	none
C7	61	M	HCV/ETOH	Well differentiated	none
C8	57	M	NASH	Well differentiated	none
C9	65	M	HBV/ETOH	Moderately differentiated	none
C10	66	M	HCV	Well differentiated	none
C11	69	F	HCV	Moderately differentiated	none
C12	71	M	NASH	Moderately differentiated	none
C13	78	M	Unknown	Moderately differentiated	none
C14	66	M	Unknown	Moderately differentiated	none
C15	84	F	NASH	Poorly differentiated	none
C16	49	M	ETOH	Moderately differentiated	none

1392

1393

1394 **Extended Data Table 3 | Immune Related Pathologic Response Criteria Scoring for HCC**
1395 **tumors treated with neoadjuvant anti-PD-1.**

Feature, *n* (%)	MPR/CR (*n* = 8)	pPR/NR (*n* = 11)	P value†
Tumor			
Fibrosis			
Immature fibrosis	8 (100%)	7 (63.6%)	0.103
Mature fibrosis	8 (100%)	7 (63.6%)	0.103
Neovascularization	1 (12.5%)	0 (0%)	0.421
Cholesterol clefts	4 (50.0%)	2 (18.2%)	0.319
Granulomas	3 (37.5%)	2 (18.2%)	0.603
Foamy histiocytes	5 (62.5%)	4 (36.4%)	0.37
Giant cells	1 (12.5%)	2 (18.2%)	1
Hemosiderin macrophages	7 (87.5%)	5 (45.5%)	0.147
Calcification	1 (12.5%)	1 (9.1%)	1
Lymphoid aggregates	8 (100%)	8 (72.7%)	0.228
Tertiary lymphoid structures	6 (75.0%)	2 (18.2%)	0.0237
Dense plasma cells	2 (25.0%)	1 (9.1%)	0.546
Peritumor			
Lymphoid aggregates	7 (87.5%)	8 (72.7%)	0.603
Tertiary lymphoid structures	4 (50.0%)	3 (27.3%)	0.377
Dense plasma cells	1 (12.5%)	0 (0%)	0.421

1396 † Fisher's Exact test
1397

1398 **Extended Data Table 4 | Bayesian Information Criteria results for predicting relapse and**
1399 **death following surgical resection in HCC treated with neoadjuvant ICB.** Rows represent
1400 different BIC calculations and columns indicate outcomes and variables evaluated and calculated
1401 BIC.
1402

Outcome	Variable	BIC
Relapse	Total TLS density	43.04
Relapse	Peritumoral TLS density	45.4
Relapse	Intratumoral TLS	37.61
Relapse	Pathologic Response	40.18
Relapse	Sex	45.58
Relapse	Prior HCV	45.68
Relapse	Prior HBV	45.63
Death	Total TLS density	15.99
Death	Peritumoral TLS density	15.63
Death	Intratumoral TLS	15.99
Death	Pathologic Response	14.89
Death	Sex	17.2
Death	Prior HCV	17.85
Death	Prior HBV	16.22

1403

Extended Data Table 5 | Differentially expressed genes in TLS high and TLS low tumors. Each row represents a single gene, and columns provide mean of normalized counts for all samples, log2 fold change in mRNA expression, Wald statistic, Wald test p-value, and Benjamini Hochberg adjusted p-values.

significantGenes.csv

Extended Data Table 6 | Gene Set Enrichment Results showing enriched pathways in TLS high tumors compared to TLS low tumors. Each tab corresponds to a different gene set in the human MSigDB. Each row represents a single pathway, and columns provide the name of the pathway, enrichment p-values, a Benjamini Hochberg adjusted p-value, the expected error for the standard deviation of the P-value logarithm, enrichment score, enrichment score normalized to mean enrichment of random samples of the same size, size of the pathway after removing genes not present, and a vector with indexes of leading-edge genes that drive the enrichment.

pathwayAnalysisResultsCombined.xlsx

1422 **Extended Data Table 7 | Summary of antibodies selected for imaging mass cytometry.**
1423

Lymphocyte	
CD45	Pan-leukocyte
CD45RA	Naïve lymphocyte
CD45RO	Antigen-experienced lymphocyte
CD3	T cell
CD4	T helper
CD8 (CD8a)	Cytotoxic T cell
CD20	B cell
CD21	Follicular dendritic cell and B cell
CD23	Follicular dendritic cell and B cell
CD138	Plasma cell
ICOS	T follicular helper
CXCR3	T follicular vs peripheral helper
CXCR5	T follicular vs peripheral helper
CCR7	Central and effector memory T cell, mature dendritic cell
FOXP3	Treg
Tumor/Structural	
PNAd	Lymphatic vessel
aSMA	Myofibroblast
Podoplanin	Fibroblast
Vimentin	Mesenchymal
Cytokeratin	Epithelial/Tumor
Functional	
CD25 (IL2R)	Activated/memory T cell
CD69	Activated/memory T cell
CD137 (4-1BB)	T cell activation
HLADR	APC, Activated T cell
PD1	T cell activation/exhaustion
PDL1	Macrophage, activated T/B, dendritic cell, epithelial
TOX	T cell activation/exhaustion
LAG3	T cell activation/exhaustion
GZMB	CTL, NK
Ki67	Proliferation Marker
BCL6	B cell GC regulator
AID	B cell somatic hypermutation
Myeloid	
CD11c	cDC1, cDC2
DCLAMP	Mature dendritic cell
DCSIGN	Macrophage and dendritic cell
CD57	NK cell, T cell senescence
CD68	Macrophage
CD86	DC, Langerhans cell, macrophage, B cell, other APC

1424

1425 **Extended Data Table 8 | Summary of metal-conjugated antibodies used for imaging mass**
1426 **cytometry.** Rows indicates a different stain, and columns indicate the metal, antigen, clone,
1427 dilution factor, source, and whether the antibody was custom-conjugated for the current study.
1428

Mass	Metal	Antigen	Clone	Dilution Factor	Source	Custom
89	Y	CD45	D9M8I	125	Cell Signaling Technology®	X
96-104	Ru	Counterstain			Electron Microscopy Sciences	
113	In	PNAd	MECA-79	250	Biolegend®	X
115	In	AID	mAID-2	125	eBioscience™	X
141	Pr	αSMA	1A4	500	Standard BioTools™	
142	Nd	Podoplanin	D2-40	125	Biolegend®	X
143	Nd	Vimentin	D21H3	500	Standard BioTools™	
144	Nd	CD11c	EP1347Y	250	Abcam	X
145	Nd	CD45RO	UCHL1	250	Biolegend®	X
146	Nd	CXCR3	IC6	100	AbboMax	X
147	Sm	CD69	EPR21814	250	Abcam	X
148	Nd	Pan-Keratin	C11	125	Standard BioTools™	
149	Sm	CD25 (IL2R)	SP176	250	Abcam	X
150	Nd	PD-L1	E1L3N	125	Cell Signaling Technology®	X
151	Eu	CXCR5	51505	250	Novus Biologicals	X
152	Sm	DC-LAMP	1010E1.01	125	Novus Biologicals	X
153	Eu	Tox/Tox2	E6I3Q	250	Cell Signaling Technology®	X
154	Sm	CD57	HNK-1	250	Cell Signaling Technology®	X
155	Gd	Foxp3	PCH101	100	Standard BioTools™	
156	Gd	CD4	EPR6855	125	Standard BioTools™	
158	Gd	ICOS	D1K2T™	250	Cell Signaling Technology®	X
159	Tb	CD68	KP1	100	Standard BioTools™	
160	Gd	Syndecan 1 (CD138)	IHC138	125	Cell Signaling Technology®	X
161	Dy	CD20	H1	125	Standard BioTools™	
162	Dy	CD8α	C8/144B	250	Standard BioTools™	
163	Dy	CD21	Bu32	250	Biolegend®	X
164	Dy	BCL-6	K112-91	250	BD Pharmingen™	X
165	Ho	PD1	EPR4877(2)	250	Abcam	X
166	Er	CD45RA	HI100	250	Standard BioTools™	
167	Er	Granzyme B	D6E9W	125	Cell Signaling Technology®	X
168	Er	Ki-67	B56	250	Standard BioTools™	
169	Tm	CD23	MRQ-57	125	Cell Marque™	X
170	Er	CD3ε	Polyclonal, C-terminal	125	Standard BioTools™	
171	Yb	Lag3	17B4	125	GeneTex	X
172	Yb	CD137 (4-1BB)	D2Z4Y	250	Cell Signaling Technology®	X
173	Yb	DC-SIGN	DCN46	62.5	Ionpath	X
174	Yb	HLA-DR	LN3	250	Standard BioTools™	
175	Lu	CD86	E2G8P	125	Cell Signaling Technology®	X
176	Yb	CCR7	EPR23192-57	250	Cell Signaling Technology®	X
191	Ir	DNA 1			Standard BioTools™	
193	Ir	DNA 2			Standard BioTools™	
195	Pt	Plasma Membrane 2	1A36	250	Standard BioTools™	
196	Pt	Plasma Membrane 3	1A37	250	Standard BioTools™	
198	Pt	Plasma Membrane 4	1A38	250	Standard BioTools™	

1429

1430 **Extended Data Table 9 | Characteristics of microdissected TLS.** Each row indicates a different
1431 patient with HCC treated with neoadjuvant immunotherapy. Columns indicate number of TLS
1432 microdissected per patient according to location (tumor or normal adjacent) and morphology
1433 (mature or involuted). Sample number shown differs from the final number of TCRβ and IGH
1434 repertoires analyzed due to filtering to remove TCRβ repertoires with fewer than 500 clones and
1435 IGH repertoires with fewer than 50 clones.
1436

	Tumor		Normal adjacent	
Patient	**Mature**	**Involuted**	**Mature**	**Involuted**
P02	2		4	
P03	5	1		
P07			5	
P08	5			
P12	3	1		
OT1	4	1		
OT6	4	3		
Total	*23*	*6*	9	

1437

1438 **Extended Data Table 10 | Expanded TCRβ clones in peripheral blood after neoadjuvant**
1439 **ICB.**
1440

Patient	TCRβ sequence	pre-PBMC count	post-PBMC count	pre-PBMC freq	post-PBMC freq	pValue	fold change	present TLS
P02	CASSSLSDNYGYTF	1412	3064	0.011764608	0.025459289	2.1E-13	2.16	1
P02	CAISLDRGGEAFF	314	687	0.002616209	0.005708398	2.8E-08	2.18	1
P02	CASKPLVWNTGELFF	0	26	0	0.000216038	2.1E-06	Inf	0
P07	CASSEPQGQLTEAFF	0	44	0	0.000261729	2.3E-08	Inf	1
P12	CASSFGTSRRSEFF	9	127	6.6405E-05	0.000723144	7.8E-13	10.89	1
P12	CAISVDRGYSGANVLTF	9	114	6.6405E-05	0.000649121	1.9E-11	9.78	1
P12	CASSFLETQYF	16	124	0.000118053	0.000706062	1.8E-09	5.98	1
P12	CAWSRAAGGPNEQFF	63	250	0.000464835	0.001423512	5.4E-08	3.06	1
P12	CASSPGLAGDEQYF	1	33	7.37833E-06	0.000187904	7.4E-06	25.47	0
P12	CASSYTVGEYNEQFF	9873	17927	0.072846265	0.102077189	5.1E-05	1.40	1
P12	CASSLDAGASSYNSPLHF	35	125	0.000258242	0.000711756	7.1E-05	2.76	1
P12	CASSPEGQIRETQYF	1501	2954	0.011074875	0.016820216	8.5E-05	1.52	0
P12	CASSSDGAYLGTEAFF	0	21	0	0.000119575	1.0E-04	Inf	0

1441
1442

1443 **Extended Data Table 11 | TCR repertoire characteristics of peripheral blood and TIL single**
1444 **cell RNA/TCR-seq data**
1445 **Peripheral blood**

Cluster	Cells, *n*	Cells with TCR, *n*	Cells with expanded TCR, *n* (%)	Cells with TCRβ in TLS, *n* (%)
CD4 Naive	615	590	47 (8)	16 (2.7)
CD8 Naive	848	807	88 (10.9)	11 (1.4)
MAIT	315	217	108 (49.8)	129 (59.4)
CD4 Naive-like	8580	7224	806 (11.2)	604 (8.4)
CD4 TCM	2677	2531	464 (18.3)	767 (30.3)
CD4 Tph	1088	988	113 (11.4)	188 (19)
CD4 TEM_GZMK	1271	1086	384 (35.4)	702 (64.6)
CD4 TEM_GZMB	942	698	660 (94.6)	601 (86.1)
CD8 TCM	892	785	164 (20.9)	202 (25.7)
CD8 TEM_GZMK	1906	1676	1147 (68.4)	1390 (82.9)
CD8 TEM_GZMB	2551	1963	1682 (85.7)	1569 (79.9)
CD8 TRM	212	91	41 (45.1)	52 (57.1)
NK-T	75	32	25 (78.1)	22 (68.8)
Treg	801	712	106 (14.9)	70 (9.8)
dnT	267	116	23 (19.8)	23 (19.8)
gdT	132	30	7 (23.3)	3 (10)
Total	23172	19546	5865 (30)	6349 (32.5)

1446
1447 **TIL**

Cluster	Cells, *n*	Cells with TCR, *n*	Cells with expanded TCRs, *n* (%)	Cells with TCRβ in TLS, *n* (%)
CD4 Naive-like	38	11	3 (27.3)	8 (72.7)
CD4 TCM	28	14	1 (7.1)	10 (71.4)
CD4 Tph	31	29	7 (24.1)	24 (82.8)
CD4 TEM_GZMK	76	48	10 (20.8)	40 (83.3)
CD8 TCM	53	10	3 (30)	7 (70)
CD8 TEM_GZMK	194	147	68 (46.3)	121 (82.3)
CD8 TEM_GZMB	37	28	16 (57.1)	24 (85.7)
CD8 TRM	36	25	14 (56)	18 (72)
Treg	22	17	3 (17.6)	8 (47.1)
dnT	28	3	1 (33.3)	3 (100)
MAIT	19	14	10 (71.4)	10 (71.4)
Total	562	346	136 (39.3)	273 (78.9)

1448

1449

Extended Data Table 12 | Association of peripheral blood and TIL single cell clusters with clonal expansion.°†

Peripheral blood

Cluster	P value	OR	95%_CI_Lower	95%_CI_Upper
CD4 TEM_GZMB	< 0.001	31.48	25.72	38.83
CD8 TEM_GZMB	< 0.001	17.99	16.17	20.04
NK-T	< 0.001	10.27	4.73	23.62
Treg	< 0.001	9.02	5.42	16.23
CD8 TEM_GZMK	< 0.001	6.27	5.63	6.97
MAIT	0.398	0.82	0.54	1.22
CD8 TRM	0.389	0.73	0.35	1.39
gdT	0.614	0.59	0.12	1.93
CD4 TEM_GZMK	< 0.001	0.4	0.32	0.51
dnT	0.002	0.34	0.13	0.73
CD8 TCM	< 0.001	0.28	0.2	0.38
CD4 TCM	< 0.001	0.13	0.1	0.17
CD8 Naive	< 0.001	0.08	0.04	0.14
CD4 Naive	< 0.001	0.05	0.02	0.12
CD4 Naive-like	< 0.001	0.04	0.03	0.05
CD4 Tph	< 0.001	0.04	0.01	0.07

TIL

Cluster	P value	OR	95%_CI_Lower	95%_CI_Upper
Treg	0.03	Inf	1.2	Inf
CD8 TEM_GZMB	0.003	3.49	1.45	8.32
CD8 TRM	0.056	2.25	0.88	5.49
CD8 TEM_GZMK	0.013	1.94	1.12	3.36
MAIT	0.518	1.44	0.32	5.19
CD8 TCM	0.689	1.19	0.12	6.83
CD4 Tph	0.159	0.39	0.07	1.32
CD4 TEM_GZMK	< 0.001	0.13	0.02	0.53
CD4 TCM	0.046	0	0	1.05
CD4 Naive-like	0.131	0	0	1.4
dnT	1	0	0	8.64

°Clonal expansion defined as greater than 5 cells per unique TCRαβ in the peripheral blood dataset and greater than 2 in TIL.

† Fisher's Exact test

Extended Data Table 13 | Association of peripheral blood and TIL single cell clusters with detection in TLS.†

Peripheral blood

Cluster	P value	OR	95%_CI_Lower	95%_CI_Upper
CD4 TEM_GZMB	< 0.001	14.12	11.35	17.72
CD8 TEM_GZMK	< 0.001	12.65	11.08	14.48
CD8 TEM_GZMB	< 0.001	10.66	9.49	12
Treg	< 0.001	4.59	3.57	5.97
NK-T	< 0.001	4.58	2.08	10.85
CD4 TEM_GZMK	< 0.001	4.15	3.64	4.73
MAIT	< 0.001	3.09	2.33	4.11
CD8 TRM	< 0.001	2.79	1.8	4.34
CD4 TCM	0.012	0.89	0.81	0.98
CD8 TCM	< 0.001	0.71	0.6	0.84
dnT	0.003	0.51	0.31	0.82
CD4 Tph	< 0.001	0.47	0.4	0.56
gdT	0.006	0.23	0.04	0.75
CD4 Naive-like	< 0.001	0.1	0.1	0.11
CD4 Naive	< 0.001	0.06	0.03	0.09
CD8 Naive	< 0.001	0.03	0.01	0.05

TIL

Cluster	P value	OR	95%_CI_Lower	95%_CI_Upper
CD8 TCM	0.445	1.63	0.26	7.35
CD4 TCM	0.505	1.52	0.34	5.48
MAIT	0.505	1.52	0.34	5.48
CD8 TRM	0.444	1.5	0.51	3.96
CD4 Naive-like	0.706	1.42	0.24	6.11
CD4 Tph	0.812	0.76	0.22	2.15
CD4 TEM_GZMK	0.567	0.72	0.28	1.66
CD8 TEM_GZMK	0.23	0.7	0.39	1.22
CD8 TEM_GZMB	0.472	0.6	0.15	1.84
Treg	0.003	0.22	0.07	0.66
dnT	1	0	0	9.1

† Fisher's Exact test

1470 **Extended Data Table 14 | Match rate of TLS TCRβ in single cell sequencing of post-**
1471 **treatment peripheral blood and TIL.**
1472
1473 **Peripheral Blood**

Patient	Total TCRβ, *n* (%)	Top 10% of TCRβ, *n* (%)	Top 1% of TCRβ, *n* (%)	Top 0.1% of TCRβ, *n* (%)
P02	274/11783 (2.3)	130/1178 (11)	52/118 (44.1)	8/12 (67)
P03	114/10872 (1)	39/1087 (3.6)	15/109 (13.8)	2/11 (18)
P07	624/11623 (5.4)	276/1162 (24)	61/116 (52.6)	11/12 (92)
P08	742/33681 (2.2)	374/3368 (11)	123/337 (36.5)	20/34 (59)
P12	422/7025 (6)	161/702 (23)	38/70 (54.3)	6/7 (86)
OT1	58/2740 (2.1)	39/274 (14)	9/27 (33.3)	1/3 (33)
OT6	674/58185 (1.2)	237/5818 (4.1)	71/582 (12.2)	15/58 (26)
Total	2908 / 135909 (2.1)	1256/13589 (9.2)	369/1359 (27.2)	63/137 (46)

1474

1475 **TIL**

Patient	Total TCRβ, *n* (%)	Top 10% of TCRβ, *n* (%)	Top 1% of TCRβ, *n* (%)	Top 0.1% of TCRβ, *n* (%)
OT6	196/58185 (0.34)	135/5818 (2.3)	76/582 (13.1)	24/58 (41)

1476

1477 **Extended Data Table 15 | Summary of antibodies used for immunohistochemistry.** Each
1478 row indicates a different stain, and columns indicate the target, antigen retrieval buffer used,
1479 clone, vendor, product ID and concentration. For dual IHC stains, first and second antibody are
1480 indicated.
1481

		First antibody			Second antibody		
Target	**Antigen retrieval buffer**	**Clone**	**Vendor**	**Conc. (µg/mL)**	**Clone**	**Vendor**	**Conc. (µg/mL)**
CD20	low pH sodium citrate	L26	Leica	0.114			
CD21/CD3	low pH sodium citrate	2G9	Leica	4.075	LN10	Leica	0.213
CD8/CD4	high pH EDTA	4B11	Leica	0.114	ER204	Millipore Sigma	0.096
Ki67/CD20	high pH EDTA	MM1	Leica	0.42	L26	Leica	0.19

1482

1483 **Extended Data Table 16 | Summary of antibodies used for FACS.**
1484

Antibody	Clone	Vendor	Dilution
Live/Dead	Zombie NIR	Biolegend	1:1000
CD3-FITC	HIT3a	Biolegend	1:100
CD19-PE/dazzle	SJ25C1	Biolegend	1:200
Fc Block	N/A	Biolegend	1:100

1485

1486

EXTENDED DATA

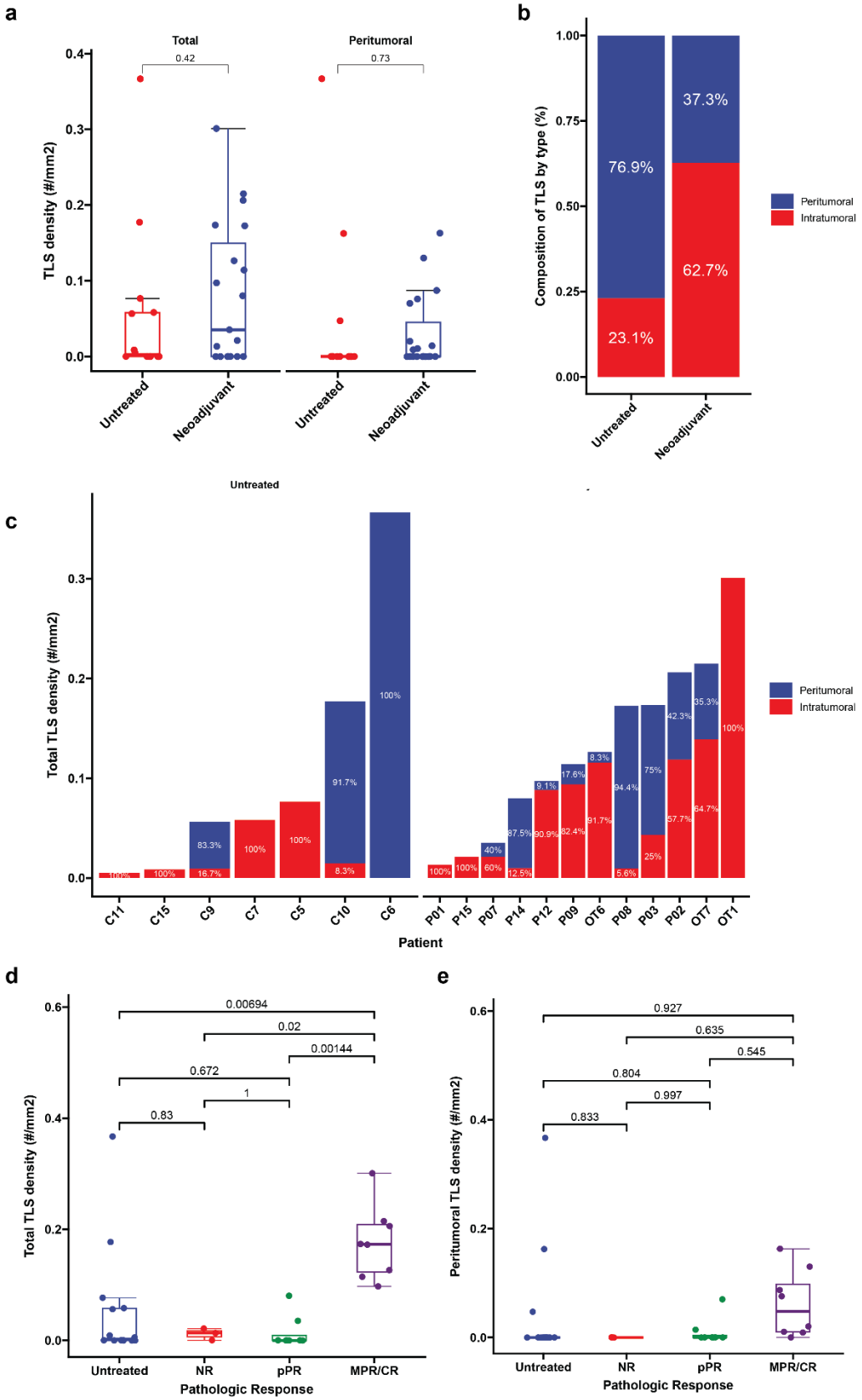

Extended Data Fig. 1 | TLS density in HCC tumors treated with neoadjuvant ICB and untreated controls. **a**, Box-and-whisker plots showing total and peritumoral TLS density in patients with locally advanced HCC treated with neoadjuvant ICB (n = 19) and untreated controls (n = 14). **b-c,** Stacked barplots showing proportion of TLS comprised of peritumoral verus intratumoral TLS location neoadjuvant treated and untreated HCC tumors (**b**) and by patient (**c**). Labels indicate proportion of total TLS comprised of peritumoral or intratumoral TLS. In **c**, patients with no observed TLS are not shown. **d-e,** Box-and-whisker plots showing total (**d**) and peritumoral (**e**) TLS density in untreated (n = 14) and neoadjuvant treated tumors, divided according to pathologic response (n = 19). Statistical significance was determined by two-tailed t-test (**a**) and one-way ANOVA followed by Tukey's honest significant difference (HSD) test (**d** and **e**).

1501
1502

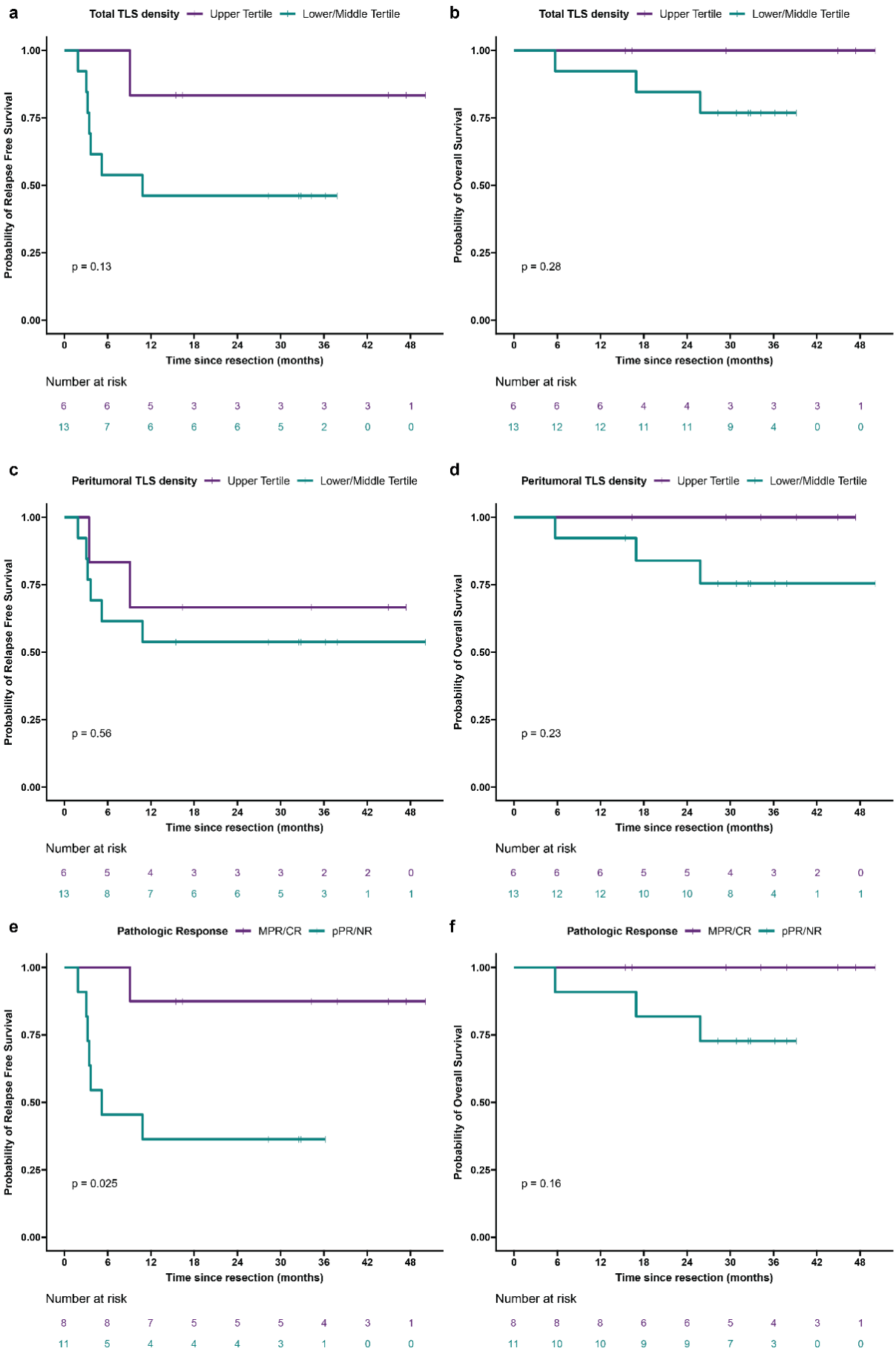
a
Total TLS density
Upper Tertile
Lower/Middle Tertile
Probability of Relapse Free Survival
p = 0.13
Time since resection (months)
Number at risk
6 6 5 3 3 3 3 3 1
13 7 6 6 6 5 2 0 0
b
Total TLS density
Upper Tertile
Lower/Middle Tertile
Probability of Overall Survival
p = 0.28
Time since resection (months)
Number at risk
6 6 6 4 4 3 3 3 1
13 12 12 11 11 9 4 0 0
c
Peritumoral TLS density
Upper Tertile
Lower/Middle Tertile
Probability of Relapse Free Survival
p = 0.56
Time since resection (months)
Number at risk
6 5 4 3 3 3 2 2 0
13 8 7 6 6 5 3 1 1
d
Peritumoral TLS density
Upper Tertile
Lower/Middle Tertile
Probability of Overall Survival
p = 0.23
Time since resection (months)
Number at risk
6 6 6 5 5 4 3 2 0
13 12 12 10 10 8 4 1 1
e
Pathologic Response
MPR/CR
pPR/NR
Probability of Relapse Free Survival
p = 0.025
Time since resection (months)
Number at risk
8 8 7 5 5 5 4 3 1
11 5 4 4 4 3 1 0 0
f
Pathologic Response
MPR/CR
pPR/NR
Probability of Overall Survival
p = 0.16
Time since resection (months)
Number at risk
8 8 8 6 6 5 4 3 1
11 10 10 9 9 7 3 0 0

1503

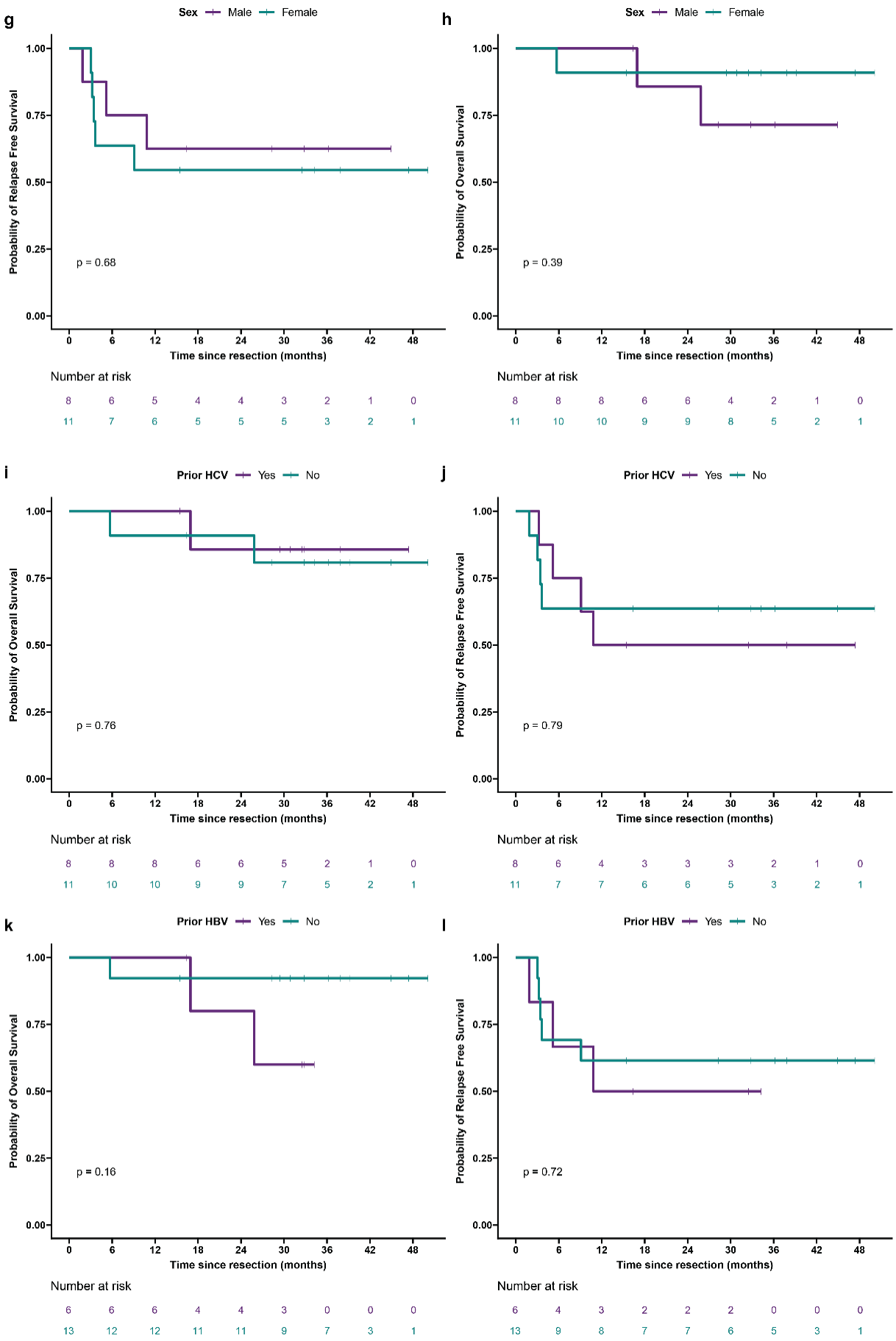
g
Sex Male Female
Probability of Relapse Free Survival
p = 0.68
Time since resection (months)
Number at risk
8 6 5 4 4 3 2 1 0
11 7 6 5 5 5 3 2 1
h
Sex Male Female
Probability of Overall Survival
p = 0.39
Time since resection (months)
Number at risk
8 8 8 6 6 4 2 1 0
11 10 10 9 9 8 5 2 1
i
Prior HCV Yes No
Probability of Overall Survival
p = 0.76
Time since resection (months)
Number at risk
8 8 8 6 6 5 2 1 0
11 10 10 9 9 7 5 2 1
j
Prior HCV Yes No
Probability of Relapse Free Survival
p = 0.79
Time since resection (months)
Number at risk
8 6 4 3 3 3 2 1 0
11 7 7 6 6 5 3 2 1
k
Prior HBV Yes No
Probability of Overall Survival
p = 0.16
Time since resection (months)
Number at risk
6 6 6 4 4 3 0 0 0
13 12 12 11 11 9 7 3 1
l
Prior HBV Yes No
Probability of Relapse Free Survival
p = 0.72
Time since resection (months)
Number at risk
6 4 3 2 2 2 0 0 0
13 9 8 7 7 6 5 3 1

1504 **Extended Data Fig. 2 | Relapse free survival and overall survival in HCC cohort treated with**
1505 **neoadjuvant ICB, according to clinical covariates. a—l**, Kaplan-Meier curves showing relapse
1506 free survival and overall survival after surgical resection for HCC patients treated with neoadjuvant
1507 ICB (*n* = 19), according to total TLS density (**a** and **b**), peritumoral TLS density (**c** and **d**),
1508 pathologic response (**e** and **f**), sex (**g** and **h**), prior hepatitis C (HCV) infection (**i** and **j**), and prior
1509 hepatitis B (HBV) infection (**k** and **l**). Statistical significance was determined by log-rank test.
1510

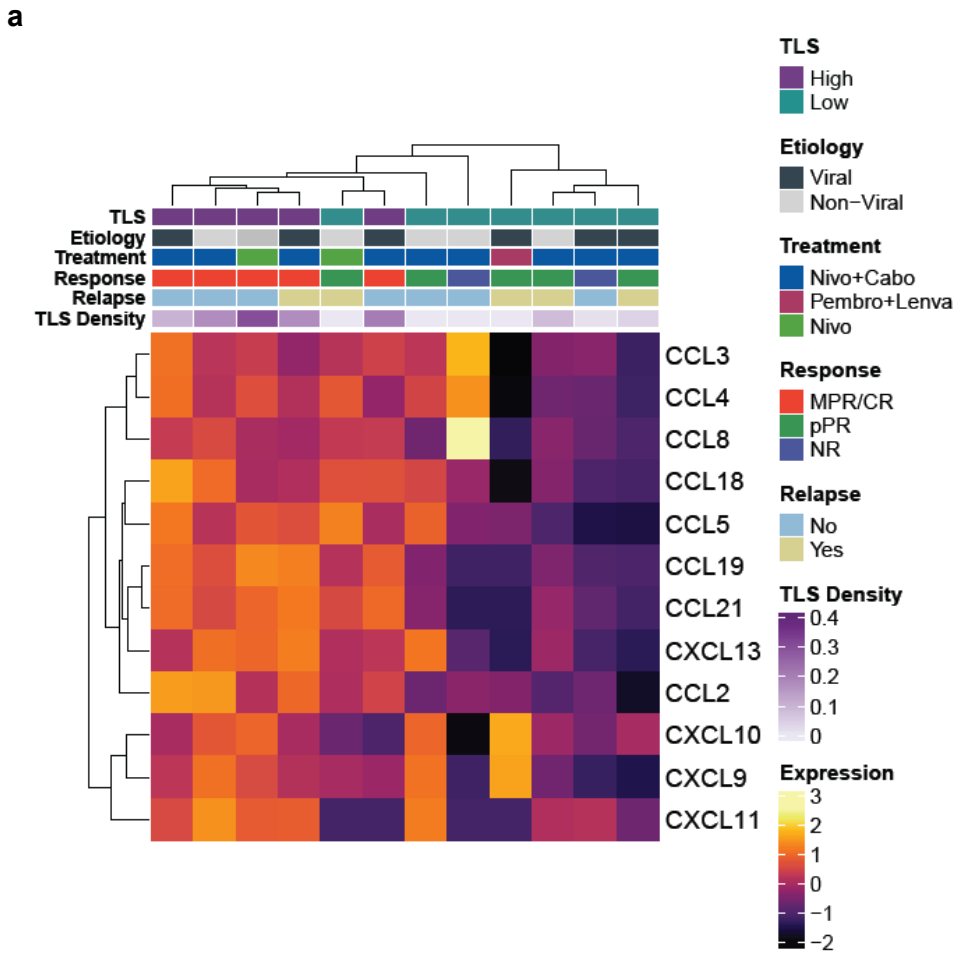

Extended Data Fig. 3 | High TLS density after neoadjuvant ICB is associated with increased expression of the 12-chemokine TLS gene signature. a, Heatmap showing expression of the 12-chemokine gene signature in tumors with high TLS density (n = 5) and low TLS density (n = 7). Annotation rows indicate TLS group, HCC etiology, neoadjuvant treatment, pathologic response, relapse, and TLS density.

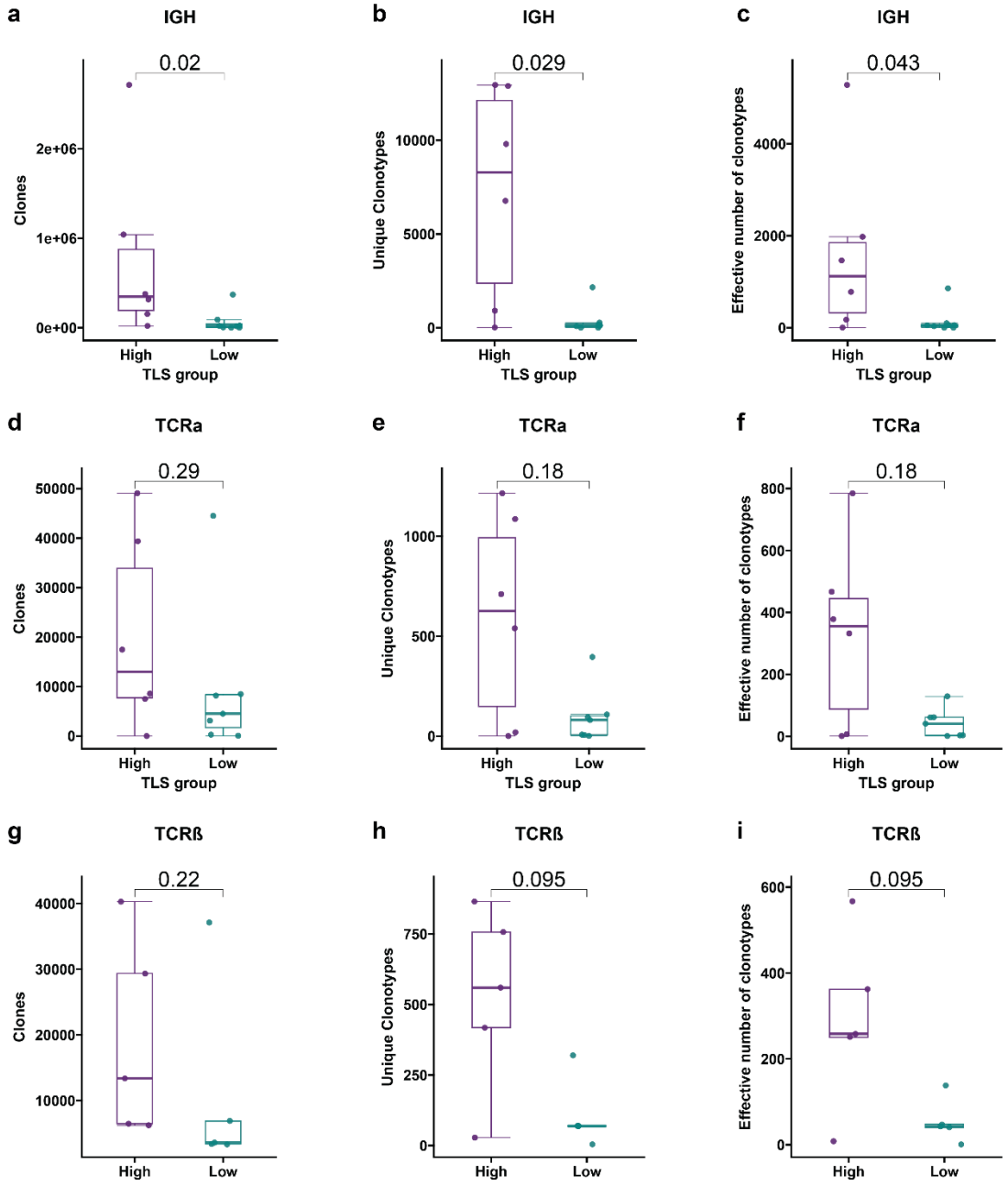

Extended Data Fig. 4 | HCC tumors with high TLS density after neoadjuvant ICB have expanded T and B cell repertoires compared to tumors with low TLS density. Box-and-whisker plots showing the total clones, unique clonotypes, and effective number of clonotypes (i.e. true diversity index) for the immunoglobulin heavy chain (IGH) **(a-c),** TCRα (**d-f**), and TCRβ (**g-i**) repertoires of HCC tumors with high and low TLS density after neoadjuvant ICB. For each box-and-whisker plot, the horizontal bar indicates the median, the upper and lower limits of the boxes the interquartile range, and the ends of the whiskers 1.5 times the interquartile range. Statistical significance was determined by Wilcoxon rank sum test.

1558

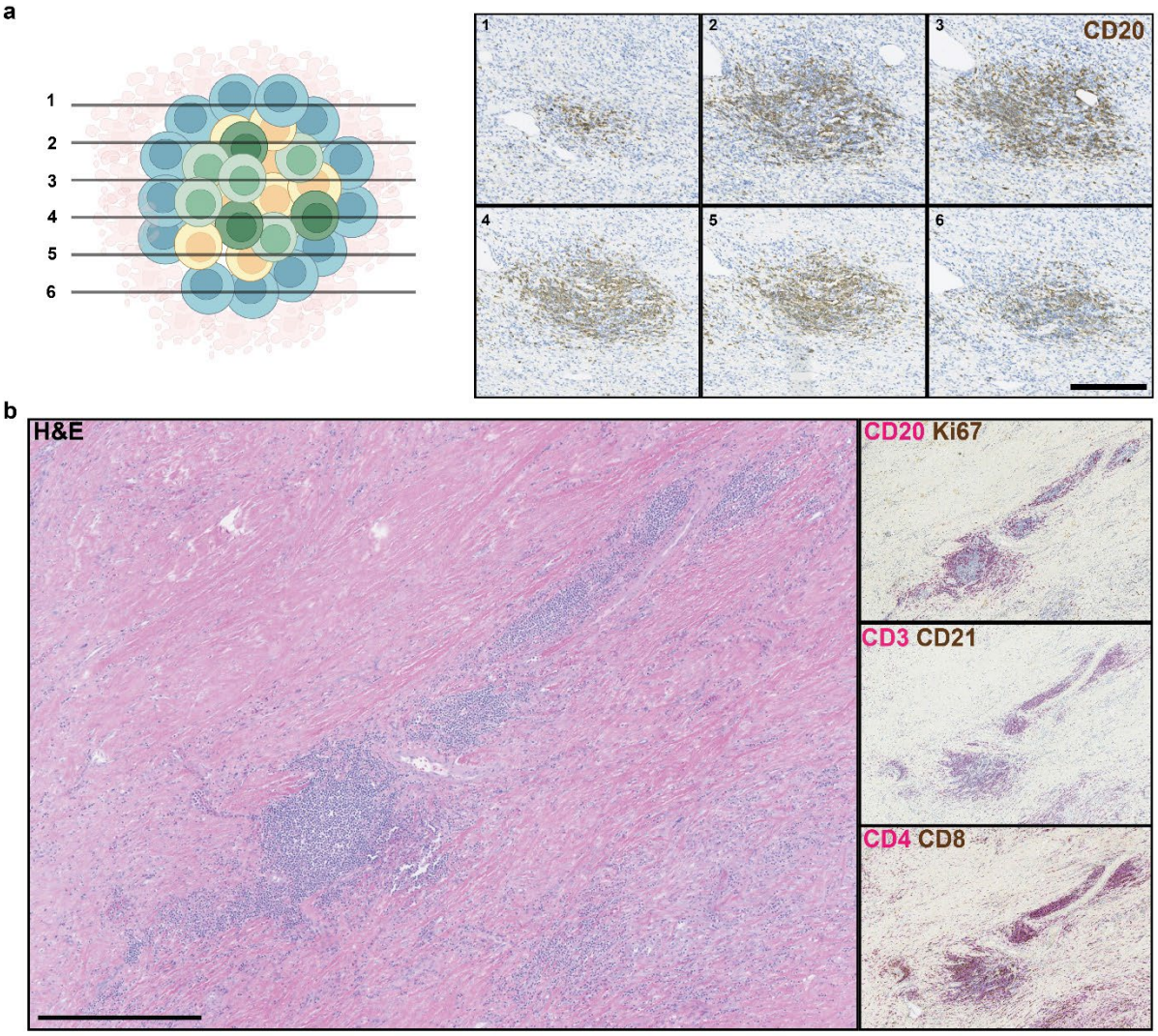

1559
1560
1561 **Extended Data Fig. 5 | Involuted TLS in an HCC tumor with complete pathologic response**
1562 **after neoadjuvant ICB (OT7). a,** Serial FFPE sections of an involuted TLS stained with anti-
1563 CD20 antibody (brown). Numbered images indicate the order in which the sections were cut from
1564 the tissue block. Scale bar, 250 μm. **b,** Representative images of multiple involuted TLS (red
1565 arrows) stained with hematoxylin and eosin (H&E), anti-CD20 (magenta) and anti-Ki67 (brown)
1566 (right middle), anti-CD3 (magenta) and anti-CD21 (brown) (middle right), and anti-CD4 and anti-
1567 CD8 (bottom right).

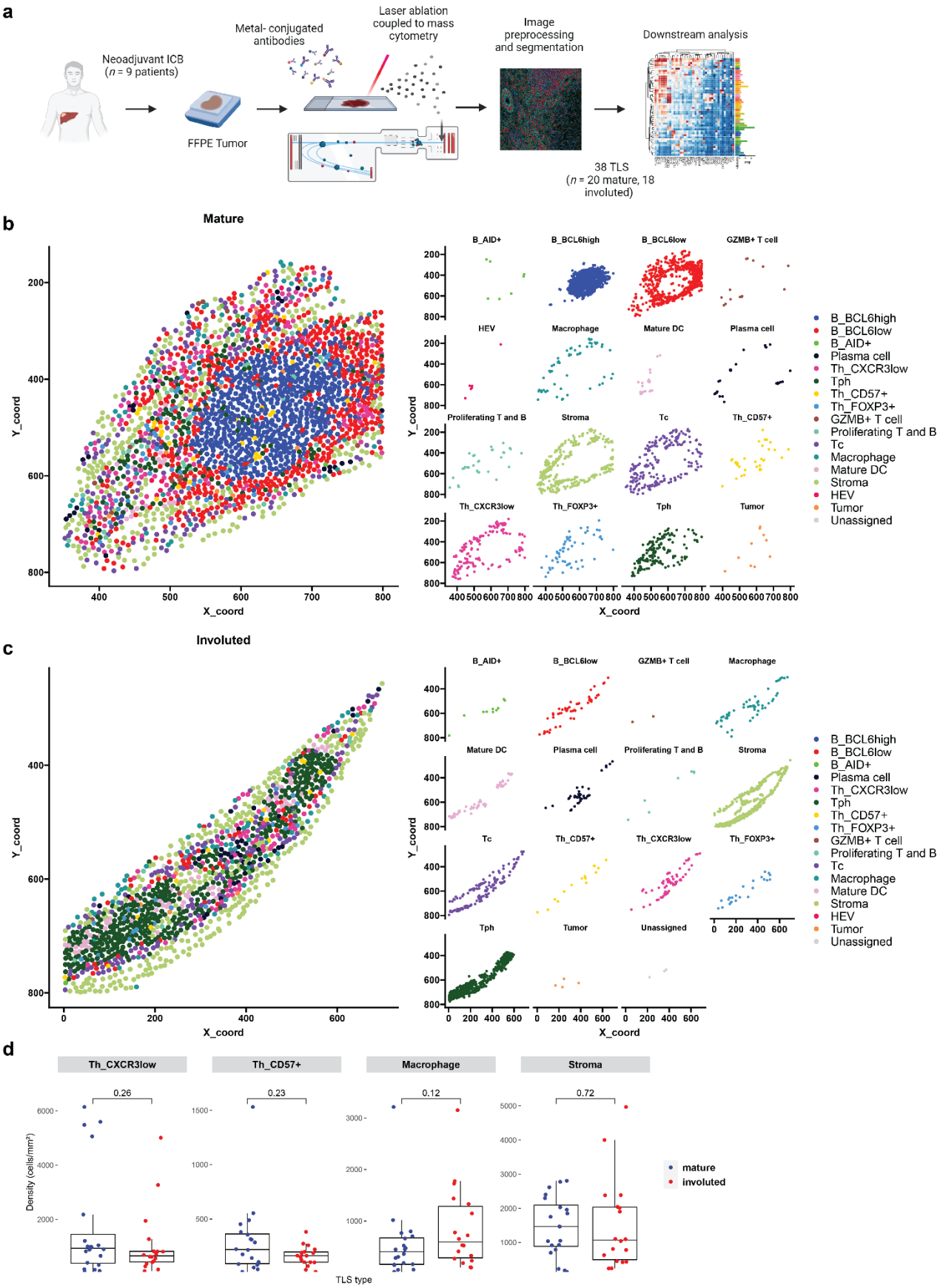
a
Neoadjuvant ICB
(n = 9 patients)
FFPE Tumor
Metal- conjugated antibodies
Laser ablation coupled to mass cytometry
Image preprocessing and segmentation
Downstream analysis
38 TLS
(n = 20 mature, 18 involuted)
b
Mature
Y_coord
X_coord
B_AID+
B_BCL6high
B_BCL6low
GZMB+ T cell
HEV
Macrophage
Mature DC
Plasma cell
Proliferating T and B
Stroma
Tc
Th_CD57+
Th_CXCR3low
Th_FOXP3+
Tph
Tumor
B_BCL6high
B_BCL6low
B_AID+
Plasma cell
Th_CXCR3low
Tph
Th_CD57+
Th_FOXP3+
GZMB+ T cell
Proliferating T and B
Tc
Macrophage
Mature DC
Stroma
HEV
Tumor
Unassigned
c
Involuted
Y_coord
X_coord
B_AID+
B_BCL6low
GZMB+ T cell
Macrophage
Mature DC
Plasma cell
Proliferating T and B
Stroma
Tc
Th_CD57+
Th_CXCR3low
Th_FOXP3+
Tph
Tumor
Unassigned
B_BCL6high
B_BCL6low
B_AID+
Plasma cell
Th_CXCR3low
Tph
Th_CD57+
Th_FOXP3+
GZMB+ T cell
Proliferating T and B
Tc
Macrophage
Mature DC
Stroma
HEV
Tumor
Unassigned
d
Th_CXCR3low
Th_CD57+
Macrophage
Stroma
0.26
0.23
0.12
0.72
Density (cells/mm²)
TLS type
mature
involuted

1568

1569 **Extended Data Fig. 6 | Characterization of divergent TLS morphologies in viable tumor and**
1570 **tumor regression bed by imaging mass cytometry. a,** Imaging mass cytometry workflow. **b-c**,
1571 Dot plots showing representative mature (**b**) and involuted (**c**) TLS, colored according to cluster
1572 assignment of individual cells after cell segmentation. (**d**) Box-and-whisker plots showing cell
1573 cluster density in mature versus involuted TLS for $CXCR3^{low}$ CD4 T cells, $CD57^{+}$ CD4 T cells,
1574 Macrophages, and Stroma. For each box-and-whisker plot, the horizontal bar indicates the
1575 median, the upper and lower limits of the boxes the interquartile range, and the ends of the
1576 whiskers 1.5 times the interquartile range. Statistical significance was determined by pairwise two
1577 sample Wilcoxon test (**d**).

1578

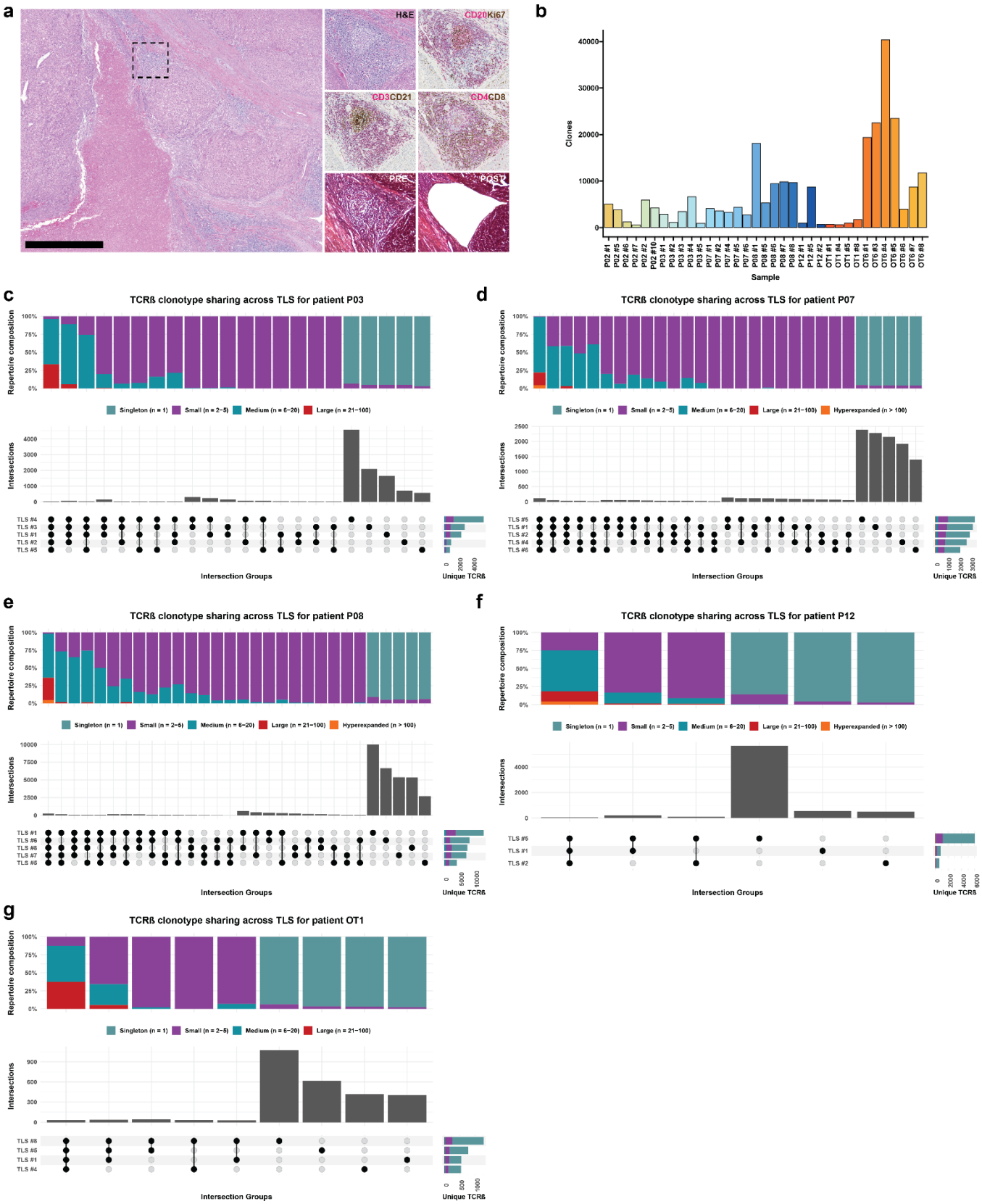
a
H&E
CD20Ki67
CD3CD21
CD4CD8
PRE
POST
b
Clones
Sample
c
TCRß clonotype sharing across TLS for patient P03
Repertoire composition
Singleton (n = 1)
Small (n = 2–5)
Medium (n = 6–20)
Large (n = 21–100)
Intersections
Intersection Groups
Unique TCRß
d
TCRß clonotype sharing across TLS for patient P07
Hyperexpanded (n > 100)
e
TCRß clonotype sharing across TLS for patient P08
f
TCRß clonotype sharing across TLS for patient P12
g
TCRß clonotype sharing across TLS for patient OT1

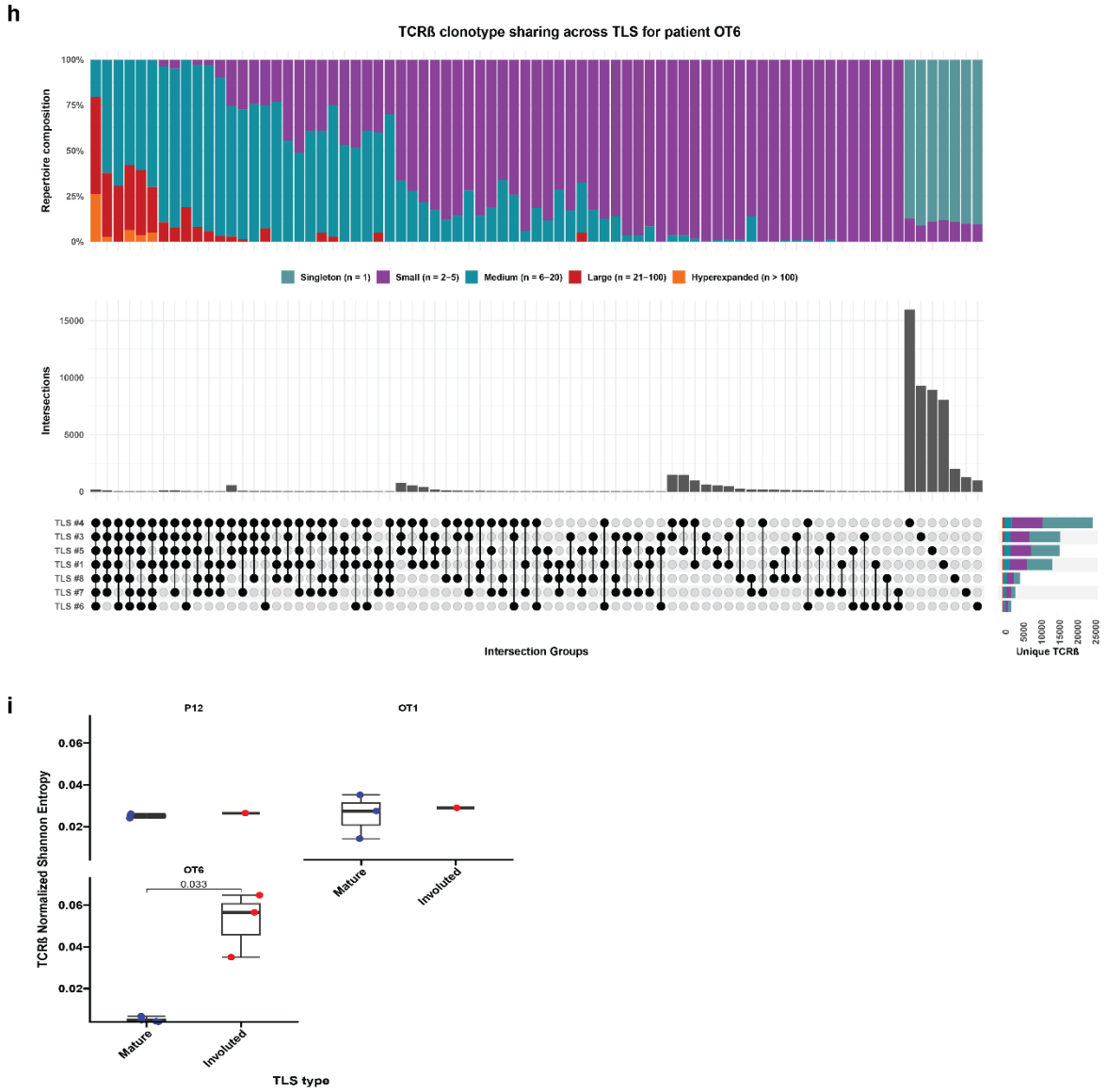

Extended Data Fig. 7 | TCRβ repertoire features of microdissected TLS. a, Representative images showing method of identification and microdissection of individual TLS. Image on left shows HCC tumor stained with hematoxylin and eosin (H&E) at low magnification. Insets show higher magnification of staining with H&E, anti-CD20 (magenta) and anti-Ki67 (brown), anti-CD3 (magenta) and anti-CD21 (brown), anti-CD4 and anti-CD8 (bottom right), and corresponding pre- and post-microdissection images. Scale bar, 1mm. **b,** Barplot showing total clone count across all microdissected TLS. **c-h,** Representative upset plots showing overlap in TCRβ clonotypes across microdissected TLS from patients P03 (**c**), P07 (**d**), P08 (**e**), P12 (**f**), OT1 (**g**), and OT6 (**h**). For each upset plot, barplots in gray and row below indicate number of overlapping clonotypes between different combinations of TCRβ repertoires. Stacked barplots at top indicate repertoire composition of different groups of TCRβ and at bottom right indicate total number of unique TCRβ clonotypes identified in each TLS, colored according to clonal expansion. Intersections with fewer than 20 unique clonotypes are not shown. **i**, Dotplot showing TCRβ repertoire clonality (as determined by Normalized Shannon Entropy) for matched mature and involuted TLS. Statistical significance was determined by two-tailed t test (**i**).

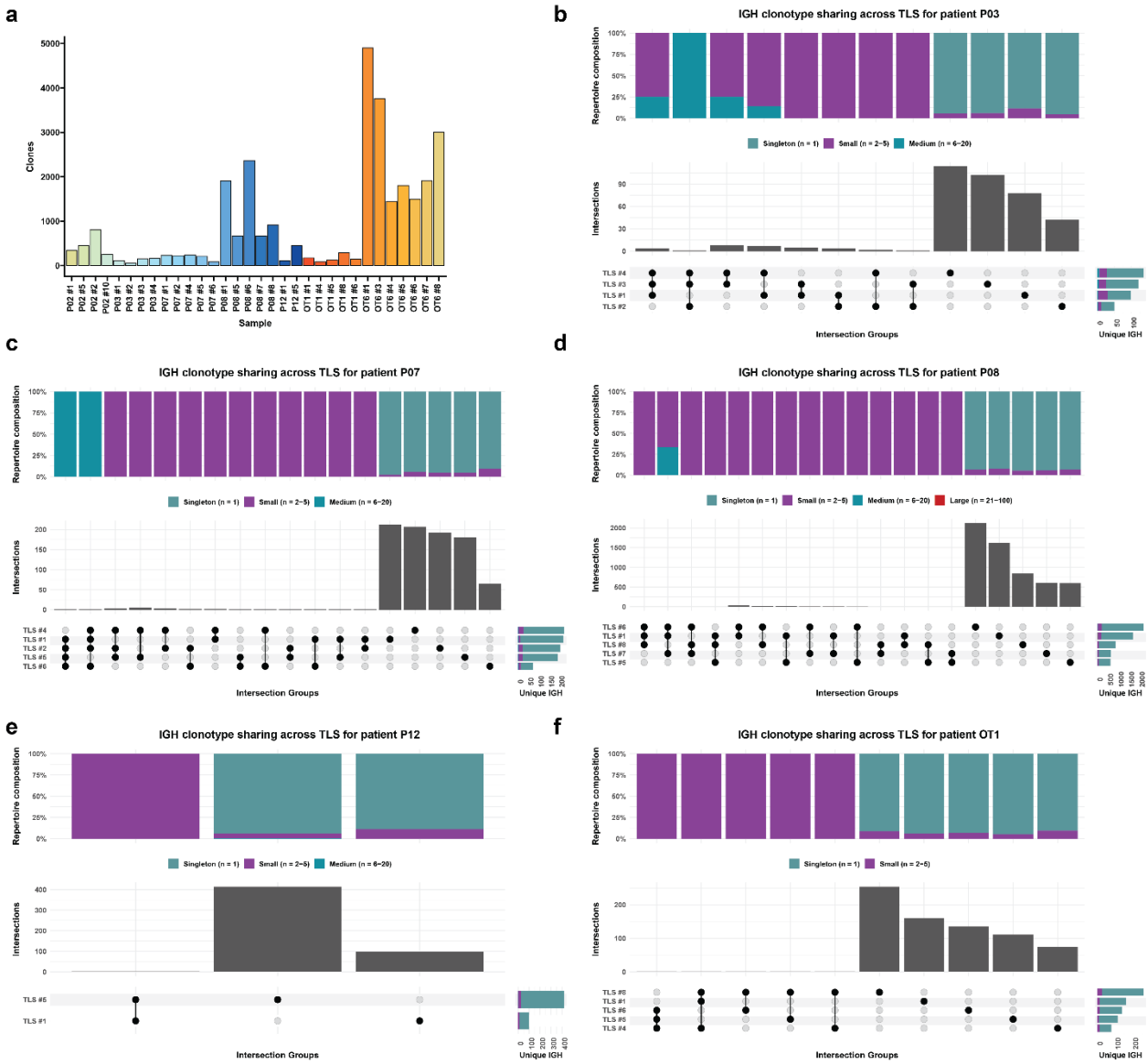
a
Clones
Sample
b
IGH clonotype sharing across TLS for patient P03
Repertoire composition
Singleton (n = 1)
Small (n = 2–5)
Medium (n = 6–20)
Intersections
Intersection Groups
Unique IGH
c
IGH clonotype sharing across TLS for patient P07
Repertoire composition
Singleton (n = 1)
Small (n = 2–5)
Medium (n = 6–20)
Intersections
Intersection Groups
Unique IGH
d
IGH clonotype sharing across TLS for patient P08
Repertoire composition
Singleton (n = 1)
Small (n = 2–5)
Medium (n = 6–20)
Large (n = 21–100)
Intersections
Intersection Groups
Unique IGH
e
IGH clonotype sharing across TLS for patient P12
Repertoire composition
Singleton (n = 1)
Small (n = 2–5)
Medium (n = 6–20)
Intersections
Intersection Groups
Unique IGH
f
IGH clonotype sharing across TLS for patient OT1
Repertoire composition
Singleton (n = 1)
Small (n = 2–5)
Intersections
Intersection Groups
Unique IGH

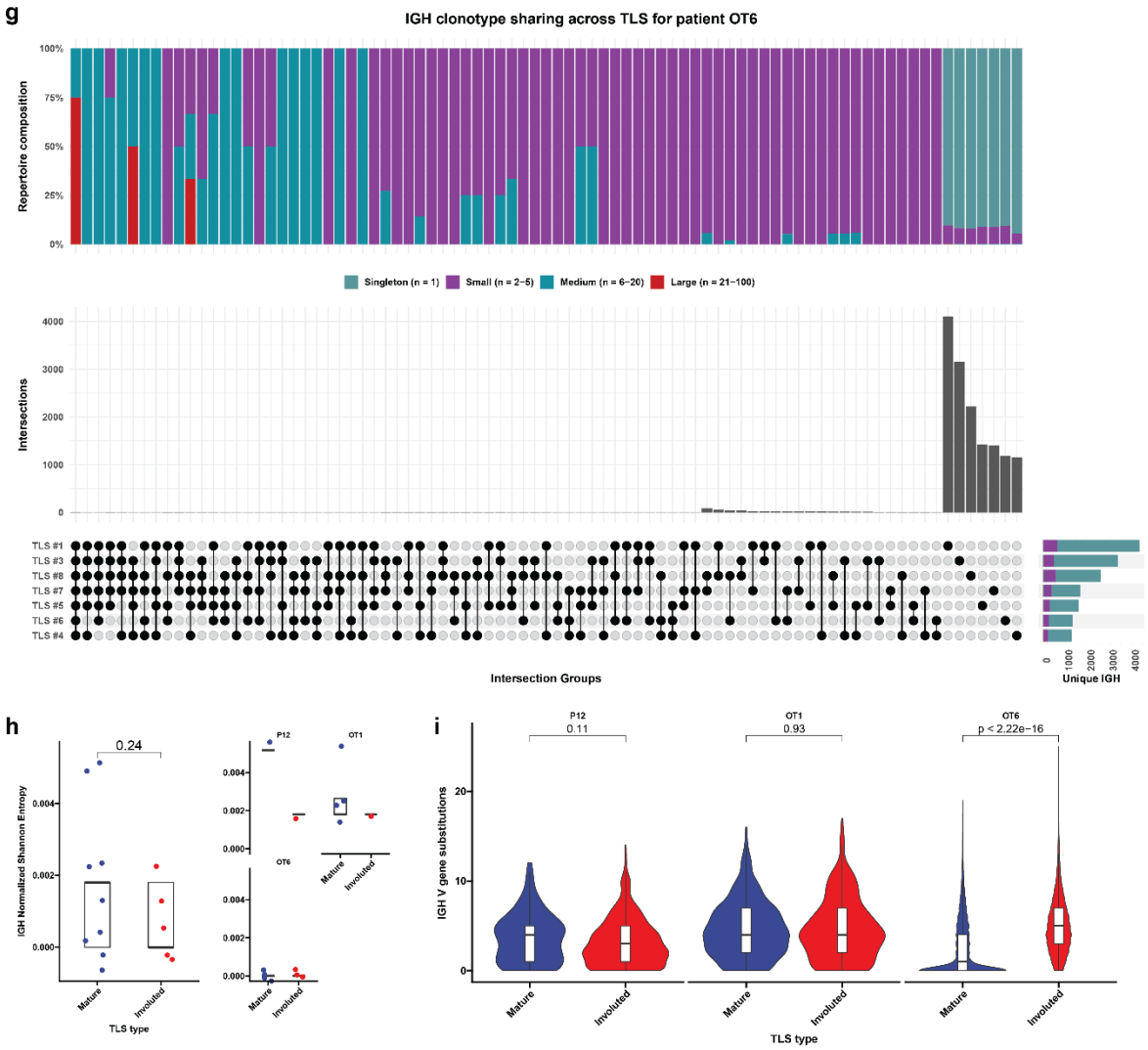

Extended Data Fig. 8 | IGH repertoire features of microdissected TLS. a, Stacked barplot showing IGH repertoire composition across all TLS. **b-f,** Representative upset plots showing overlap in unique IGH clonotypes across microdissected TLS from patients P03 (**b**), P07 (**c**), P08 (**d**), P12 (**e**), OT1 (**f**), and OT7 (**g**). Bottom barplots and annotation row indicate number of overlapping clonotypes between different TLS repertoires. Top stacked barplots indicate clonal composition of overlapping ("public IGH") and nonoverlapping ("Private IGH"). Bottom right stacked barplots indicate total number of unique IGH clonotypes identified at each TLS and overall clonal composition. **h,** Dotplot showing IGH repertoire clonality (as determined by Normalized Shannon Entropy) for microdissected TLS, according to TLS morphology. Statistical significance was determined by two-tailed t test (**h** and **i**).

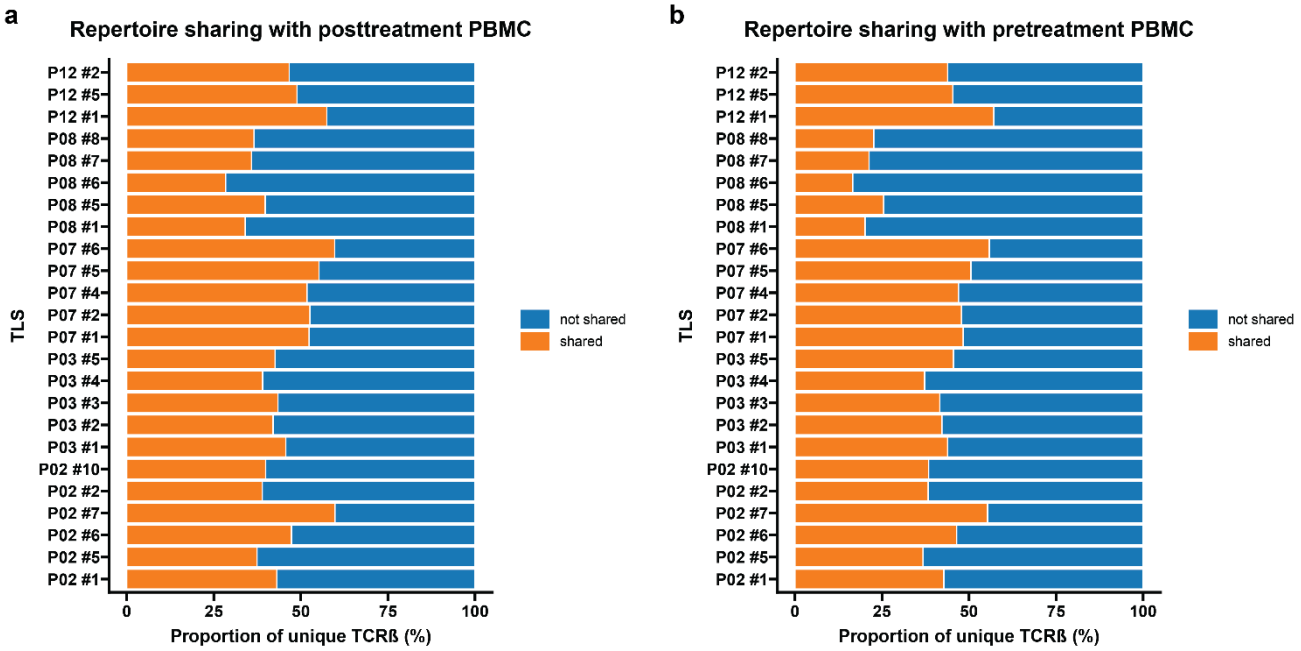

Extended Data Fig. 9 | TLS display a high degree of T cell repertoire overlap with pre- and post-treatment peripheral blood. a-b, Barplots showing proportion of unique TCRβ clonotypes at each TLS that also identified in matched pre-treatment (**a**) and post-treatment (**b**) peripheral blood.

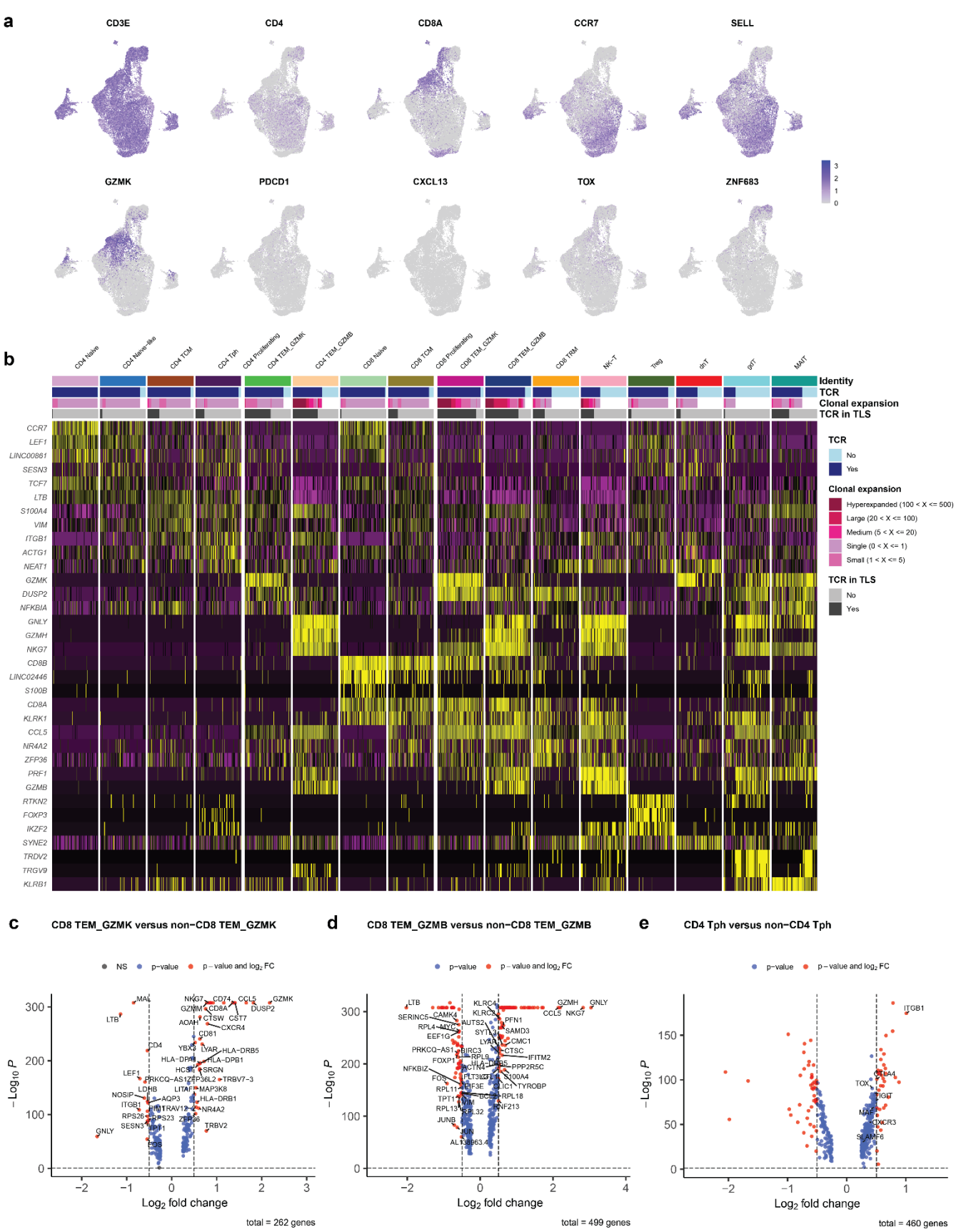
a
CD3E
CD4
CD8A
CCR7
SELL
GZMK
PDCD1
CXCL13
TOX
ZNF683
b
CD4 Naïve
CD4 Naïve-like
CD4 TCM
CD4 Tph
CD4 Proliferating
CD4 TEM_GZMK
CD4 TEM_GZMB
CD8 Naïve
CD8 TCM
CD8 Proliferating
CD8 TEM_GZMK
CD8 TEM_GZMB
CD8 TRM
NK-T
Treg
dnT
gdT
MAIT
Identity
TCR
Clonal expansion
TCR in TLS
TCR
No
Yes
Clonal expansion
Hyperexpanded (100 < X <= 500)
Large (20 < X <= 100)
Medium (5 < X <= 20)
Single (0 < X <= 1)
Small (1 < X <= 5)
TCR in TLS
No
Yes
c
CD8 TEM_GZMK versus non−CD8 TEM_GZMK
NS
p−value
p − value and log2 FC
−Log10 P
Log2 fold change
total = 262 genes
d
CD8 TEM_GZMB versus non−CD8 TEM_GZMB
p−value
p − value and log2 FC
−Log10 P
Log2 fold change
total = 499 genes
e
CD4 Tph versus non−CD4 Tph
p−value
p − value and log2 FC
−Log10 P
Log2 fold change
total = 460 genes

Extended Data Fig. 10 | Single cell sequencing of post-treatment peripheral blood. a, UMAPs showing gene expression of *CD3E*, *CD4*, *CD8A*, *CCR7*, *SELL*, *GZMK*, *PDCD1*, *CXCL13*, *TOX*, and *ZNF683* across all single cells sequenced from post-treatment peripheral blood of 7 HCC patients treated with neoadjuvant ICB. **b,** Heatmap showing gene expression of the top 3 differentially expressed genes per cluster. Rows represent single genes and columns represent individual cells. Annotation bar indicates cluster identity, whether each cell had a sequenced TCR, the clonality of the TCR, and whether the TCR was identified in microdissected TLS from the same patient. Clusters were downsampled to 75 cells per cluster for visualization. **c-e,** Volcano plots showing differentially expressed genes in the CD8 TEM_GZMK (**b**),CD8 TEM_GZMB (**c**), and CD4 Tph **(d)** clusters compared to all other cells. Vertical dotted lines indicates a fold change of greater or less than 1.4 and horizontal line indicates a P value of 0.05. Labeled genes in **c** and **d** indicate genes with the highest differential expression. Labeled genes in **e** indicate genes known to be highly expressed in CD4 Tph.

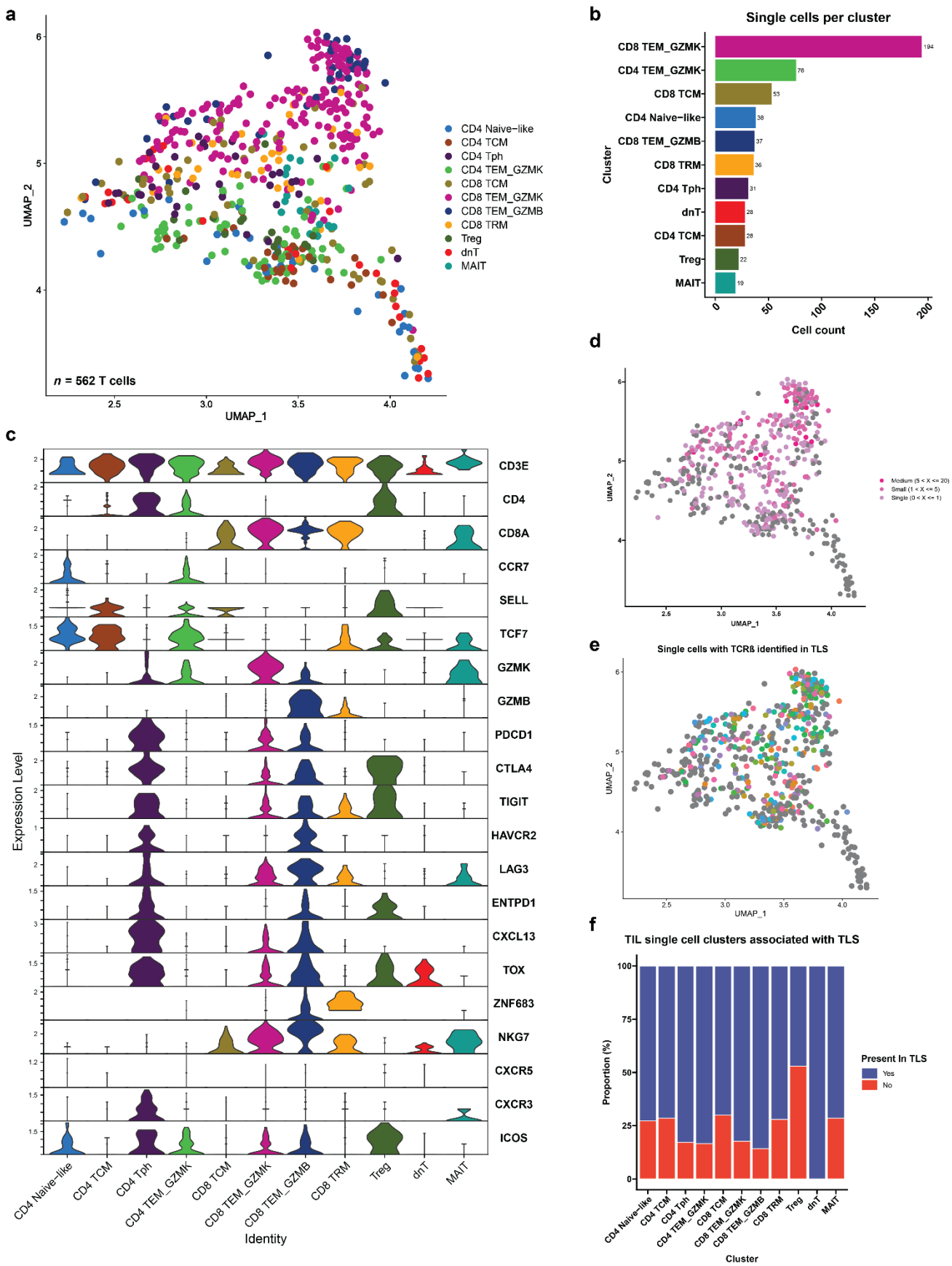
a
UMAP_2
UMAP_1
n = 562 T cells
CD4 Naive−like
CD4 TCM
CD4 Tph
CD4 TEM_GZMK
CD8 TCM
CD8 TEM_GZMK
CD8 TEM_GZMB
CD8 TRM
Treg
dnT
MAIT
b
Single cells per cluster
Cluster
Cell count
CD8 TEM_GZMK 194
CD4 TEM_GZMK 76
CD8 TCM 53
CD4 Naive−like 38
CD8 TEM_GZMB 37
CD8 TRM 36
CD4 Tph 31
dnT 28
CD4 TCM 28
Treg 22
MAIT 19
c
Expression Level
Identity
CD3E
CD4
CD8A
CCR7
SELL
TCF7
GZMK
GZMB
PDCD1
CTLA4
TIGIT
HAVCR2
LAG3
ENTPD1
CXCL13
TOX
ZNF683
NKG7
CXCR5
CXCR3
ICOS
d
UMAP_2
UMAP_1
Medium (5 < X <= 20)
Small (1 < X <= 5)
Single (0 < X <= 1)
e
Single cells with TCRß identified in TLS
UMAP_2
UMAP_1
f
TIL single cell clusters associated with TLS
Proportion (%)
Cluster
Present In TLS
Yes
No

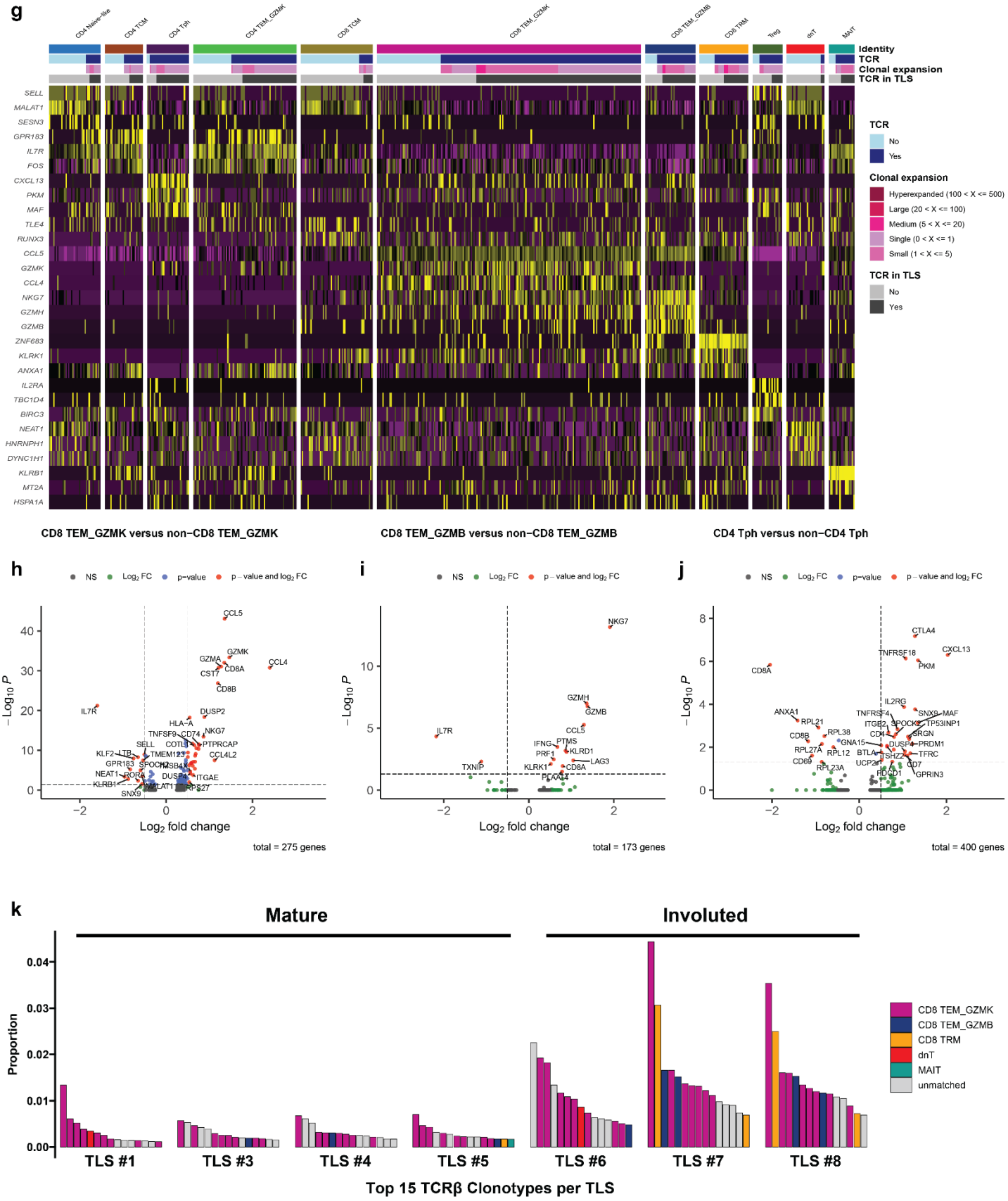
g
CD4 Naive-like
CD4 TCM
CD4 Tph
CD4 TEM_GZMK
CD8 TCM
CD8 TEM_GZMK
CD8 TEM_GZMB
CD8 TRM
Treg
dnT
MAIT
Identity
TCR
Clonal expansion
TCR in TLS
SELL
MALAT1
SESN3
GPR183
IL7R
FOS
CXCL13
PKM
MAF
TLE4
RUNX3
CCL5
GZMK
CCL4
NKG7
GZMH
GZMB
ZNF683
KLRK1
ANXA1
IL2RA
TBC1D4
BIRC3
NEAT1
HNRNPH1
DYNC1H1
KLRB1
MT2A
HSPA1A
TCR
No
Yes
Clonal expansion
Hyperexpanded (100 < X <= 500)
Large (20 < X <= 100)
Medium (5 < X <= 20)
Single (0 < X <= 1)
Small (1 < X <= 5)
TCR in TLS
No
Yes
CD8 TEM_GZMK versus non−CD8 TEM_GZMK
CD8 TEM_GZMB versus non−CD8 TEM_GZMB
CD4 Tph versus non−CD4 Tph
h
NS
Log2 FC
p−value
p − value and log2 FC
−Log10 P
Log2 fold change
total = 275 genes
i
total = 173 genes
j
total = 400 genes
k
Mature
Involuted
Proportion
CD8 TEM_GZMK
CD8 TEM_GZMB
CD8 TRM
dnT
MAIT
unmatched
TLS #1
TLS #3
TLS #4
TLS #5
TLS #6
TLS #7
TLS #8
Top 15 TCRβ Clonotypes per TLS

Extended Data Fig. 11 | Single cell sequencing of post-treatment TIL from patient OT6. a, Uniform Manifold Approximation and Projection (UMAP) for 562 T cells identified by single cell RNA/TCR/BCR sequencing of $CD3^{+}CD19^{+}$ FACS-sorted tumor infiltrating lymphocytes. **b,** Barplot showing number of single cells per cluster. **c,** Violin plots showing expression of subset specific marker genes across clusters. **d-e,** UMAPs showing clonality of single cells with an associated T cell receptor sequence (**d**) and single cells with a TCRβ identified in microdissected TLS (**e**). **f,** Stacked barplot showing proportion of each single cell cluster identified in TLS. **g,** Heatmap showing gene expression of the top 3 differentially expressed genes per cluster. Rows represent single genes and columns represent individual cells. Annotation bar indicates cluster identity, whether each cell had a sequenced TCR, the clonality of the TCR, and whether the TCR was identified in microdissected TLS from the same patient. **h-j,** Volcano plots showing differentially expressed genes in the CD8 TEM_GZMK (**h**),CD8 TEM_GZMB (**i**), and CD4 Tph **(j)** clusters compared to all other cells. Vertical dotted lines indicates a fold change of greater or less than 1.4 and horizontal line indicates a P value of 0.05. **k,** Inferred transcriptional phenotype of the top 15 TCRβ clonotypes in mature and involuted TLS of patient OT6.

a

TCRβ CDR3aa	*n* cells in peripheral blood	*n cells in* tumor
CAIKGGLAEETQYF	2	4
CASAQQDTDTQYF	2	2
CASGWDRRNTEAFF	1	1
CASRDQGGQTQYF	2	2
CASRSLTGQGAVRETYEQFF	2	2
CASSDSSGRADTQYF	12	5
CASSFDPYEQYF	12	2
CASSLGLGQNTGELFF	1	1
CASSLVGGSGANVLTF	1	2
CASSQVREGTQYF	1	1
CASSVGGDLGEAFF	1	1
CASTPYPSGRRNEQFF	1	1
CAWSVSPPGEQYF	1	1
CSAPSRDFRNSPLHF	2	2
CSARGTREPYEQYF	4	2
CSVSPESAGTRETQYF	1	1

b

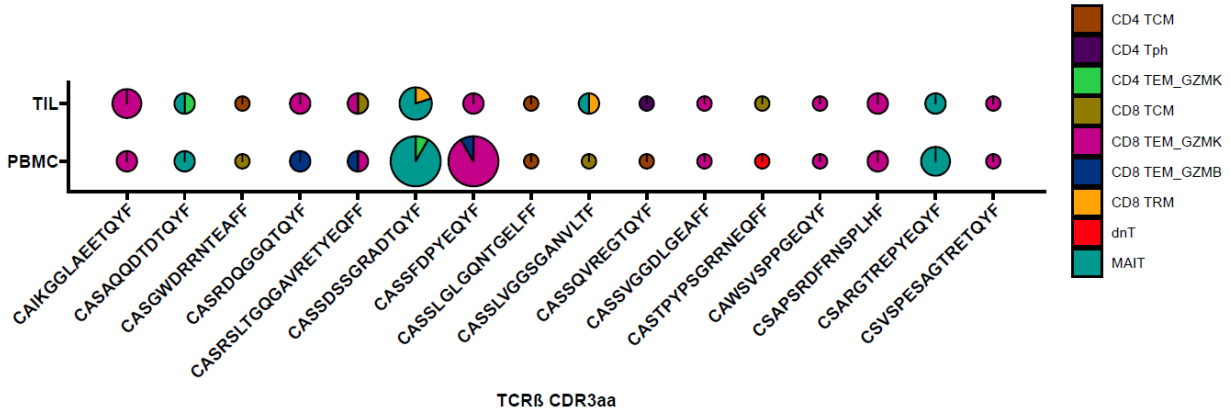

Extended Data Fig. 12 | Cluster annotation of single cells with shared TCRβ in post-treatment peripheral blood and TIL (*n* = 16) from patient OT6. a, Shared TCRβ identified in both PBMC and TIL for patient OT6. Rows indicate different TCRβ clonotype and columns provide the complementarity determining region 3 (CDR3) amino acid sequence and number of cells with the TCRβ CDR3 amino acid sequence in peripheral blood and TIL, respectively. **b,** Single cell cluster identities of shared TCRβ according to unique CDR3 and compartment where the TCR was identified. Piecharts are colored according to the cluster identities of all cells with the same TCRβ. The radius of each piechart is proportional to the total number of cells in which each TCRβ was identified (square root of *n* cells divided by eight).